Nonlinear State Estimation of the Ionosphere as Perturbed by the 2017 Great American Eclipse

Kevin Lee Sauerwein

Thesis submitted to the faculty of the Virginia Polytechnic Institute and State University in partial fulfillment of the requirements for the degree of

Master of Science

In

Aerospace Engineering

Mark L. Psiaki, Chair

Gregory Earle

Scott England

December 3, 2018

Blacksburg, VA

Keywords: Eclipse, Nonlinear State Estimation, Ionosphere

Nonlinear State Estimation of the Ionosphere as Perturbed by the 2017 Great American Eclipse

Kevin Lee Sauerwein

ABSTRACT

The 2017 Great American Eclipse provided an excellent opportunity for scientists and engineers to study the ionosphere. The dynamics of the ionosphere are affected by the amount of solar radiation it receives and a total solar eclipse produces a short perturbation to the incoming solar radiation. Analyzing how the ionosphere reacts to this type perturbation could lead to new levels of understanding of it. This study develops a nonlinear filter that estimates the state of the ionosphere's 3-D electron density profile given total electron content (TEC) measurements from dual-frequency GPS receivers located on the ground and on low-Earth-orbiting spacecraft. The electron density profile is parameterized by a bi-quintic latitude/longitude spline of Chapman Profile parameters that define the vertical electron density profile. These Chapman parameters and various latitude and longitude partial derivatives are defined at a set of latitude/longitude spline grid points. Bi-quintic interpolation between the points defines the parameters' values and the corresponding Chapman profiles at all latitude/longitude points. The Chapman parameter values and their partial derivatives at the latitude/longitude spline nodes constitute the unknowns that the nonlinear filter estimates. The filter is tested with non-eclipse datasets to determine its reliability. It performs well but does not estimate the biases of the receivers as precisely as desired. Many attempts to improve the filter's bias estimation ability are presented and tried. Eclipse datasets are input to the filter and analyzed. The filter produced results that suggest that the altitude of peak electron density increased significantly near and within the eclipse path and that the vertical TEC (VTEC) was drastically decreased near and within the eclipse path. The changes in VTEC and altitudes of peak electron density caused by the eclipse leave a lasting effect that alters the density profile for anywhere from 15 minutes to several hours.

Nonlinear State Estimation of the Ionosphere as Perturbed by the 2017 Great American Eclipse

Kevin Lee Sauerwein

GENERAL AUDIENCE ABSTRACT

The 2017 Great American Eclipse garnered much attention in the media and scientific community. Solar eclipses provide unique opportunities to observe the ionosphere's behavior as a result of irregular solar radiation patterns. Many devices are used to measure this behavior, including GPS receivers. Typically, GPS receivers are used to navigate by extracting and combining carrier phase and pseudorange data from signals of at least four GPS satellites. When the position of a GPS receiver is well-known, information about the portion of the ionosphere that the signal traveled through can be estimated from the GPS signals. This estimation procedure has been done with ground-based and orbiting GPS receivers. However, fusing the two data sources has never been done and will be a primary focus of this study. After demonstrating the performance of the estimation algorithm, it is used to estimate the state of the ionosphere as it was perturbed by the 2017 Great American Eclipse.

ACKNOWLEDGEMENTS

I would like to thank my advisor and mentor, Dr. Psiaki, for guiding me through a difficult year and half of graduate school. He taught me a lot about filtering, estimation and GPS. I learned many invaluable lessons through him and he helped me to become a better engineer. Thank you for your patience and guidance in my research and studying under you. The four other members of the "GPS Group," Brian, Brian, Matt, and Mike, are great engineers and friends. Whether meeting afterhours to try so desperately to learn how to build a software-defined GPS receiver or bonding at the Blacksburg Taphouse, I was never short of good company.

I would like to thank Virginia Tech, and the department of Aerospace and Ocean Engineering, for facilitating all that I've learned the last 18 months. I would like to thank Dr. Earle and Dr. England for their support and lending me their technical expertise in my research area. Thank you to all the dedicated professors I've had at Virginia Tech, especially Dr. Southward, Dr. Kuester, and Dr. Beatty. Thank you to the outstanding engineers, professors and fellow grad students at Space@VT for the great community you've provided me with.

I would like to thank my fiancée, Shawn, for her love, support and understanding through writing my thesis and all graduate school. You're Microsoft Word expertise has saved me countless hours. Thank you, Jeremy and Rajath. The many good times and laughs we've shared have helped me get through graduate school in one piece. Thank you to my family for your support and for raising me and teaching me to work hard.

CONTENTS

LIST OF FIGURES

CHAPTER 1: INTRODUCTION AND LITERATURE REVIEW

Since its initial postulation by Carl Friedrich Gauss in 1839, and its role in the reception of the first trans-Atlantic radio signal in 1901, the ionosphere has been probed and studied by scientists and engineers worldwide. Particularly, the spatial and temporal distribution of electrons within the ionosphere form a 3-dimensional (3D) electron density profile. Precise knowledge of this profile is valuable in many applications such as general radio frequency communications, scintillation predictions for satellite communications, and range delay estimates to be used in satellite-based navigation [1].

A fraction of the time that it takes a radio signal to travel from a GPS satellite to a GPS receiver is spent in the ionosphere. While traveling through the ionosphere, that signal's speed is altered, and its path is deflected due to its radio-frequency carrier wave's interaction with the ionosphere [1]. This perturbation of the speed is realized when estimating a GPS receiver's position in that an unknown time delay is imposed upon the receiver due to the signal's journey through the ionosphere. The magnitude of this delay is directly related to the degree of interaction between the signal and the ionosphere. And, the total degree of interaction between the signal and the ionosphere is a function of the path integral of the electron density and the frequency of the radio wave. The integrated electron density along the path of the radio wave is the Total Electron Content (TEC) of that path and must be estimated for each position update that a dual-frequency GPS receiver outputs [2].

Scientists and engineers take advantage of this TEC estimate and apply inversion techniques to extract the electron density profile from a set of TEC path integrals. Even though most of these inversion techniques do not use multiple data types, there have been attempts to do this [3]. The methods that do not use multiple data types make assumptions based on thin-shelled ionosphere approximations or do not allow unknown ionosphere variables to fluctuate much.

TEC measurements can be collected from ground-based dual-frequency receivers such as those that comprise the Continuously Operating Reference Stations (CORS) network and from

dual-frequency receivers mounted on Low Earth Orbiting (LEO) satellites. TEC measurements from CORS receivers are successfully used in ionospheric state estimation regularly. One study inverted thousands of CORS TEC measurements to develop a smooth, parameterized estimate of the electron density profile. It demonstrated a method that combined a latitude/longitude bi-quintic spline with a vertical electron density profile to produce a regional 3D electron density profile via solution of a nonlinear estimation problem that seeks to produce the model that best fits the measured TEC values [4]. The first of two objectives of this thesis is to continue the work completed from that study by assimilating TEC measurements from LEO satellites, which are known as radio-occultation (RO) measurements, into the nonlinear estimation problem along with TEC measurements from ground-based receivers. The second objective of this thesis is to use the resulting batch filter to estimate the 3D electron density profile during the Great American Eclipse of 2017.

1.1 The 2017 Great American Eclipse

The ionosphere's electron density profile is highly dependent on the amount of solar radiation it receives. As the sun sets, the ionosphere electron density begins to decay, with the density levels in lower layers decaying the fastest, and the density levels in the upper-most F layers continuing to decay all night. The resulting decay of the electron density follows a somewhat predictable pattern and can be observed daily. Similarly, as the sun rises at dawn, the ionosphere begins to gain electron density until about 2 p.m. local time. Once again, this cycle is somewhat predictable and can be observed daily. However, what is not as predictable and is rarely observed is the effect that a temporary complete blockage of sunlight during the middle of the day has on the local ionosphere.

On August 21, 2017, a total solar eclipse passed directly over the Contiguous United States (CONUS) giving it the name the Great American Eclipse. Beginning at 15:46 UTC in the central Pacific Ocean and ending at 21:04 UTC in the eastern Atlantic Ocean, the eclipse created a

complete blockage of sunlight over a swath that crossed the CONUS. The total eclipse shadow diameter was, on average, about 100 kilometers. And, the region of the Earth in partial shadow was much larger at any given point in time. The eclipse's location over the United States is significant in studying its effect on the local ionosphere because the CORS network of GPS receivers used to collect data in this study is in the United States. So, during the entirety of the eclipse, nearly 2000 GPS receivers were measuring TEC along multiple lines of sight to multiple GPS spacecraft at regular intervals. The assimilation of these data, along with RO TEC measurements from LEO satellites above the locally eclipsed region, created a situation where the local electron density profile, as modeled with Chapman Profiles, was observable in an estimation sense. The geometry of the eclipse allows the perturbed ionosphere to be observed from approximately 9:00 a.m. local time to 4:00 p.m. local time. With the assimilation of the two datasets, the eclipse's direct effect on a completely (and partially) dark ionosphere and how the ionosphere recovers from brief solar radiation blockage can be estimated.

The effects of solar eclipses on the ionosphere have been measured in the past by many. For example, Ref. [5] compared vertical incidence sounding and TEC measurements of the October 3rd, 2005 eclipse over Europe. Ref. [6] examined VLF delay time and differential Doppler shift data. Ref. [7] analyzed TEC measurements from GPS receivers during the March 9, 1997 eclipse. Ref. [8] used a large ionosonde network, and Ref. [9] used data from about 100 GPS stations to analyze the August 11, 1999 eclipse. Even in 1963, Ref. [10] analyzed data collected from several rocket flights during the July 20, 1963 eclipse.

The particular eclipse of August 21, 2017 also garnered a large amount of research interest. Ref. [11] used data collected by citizens to detect changes in medium- and high-frequency radio wave propagation. Ref. [12] analyzed data collected from SuperDARN high-frequency radars, software-defined radios and scintillation receivers.

1.2 Ionosphere Behavior and Characteristics

The ionosphere is a shell of electrons and electrically charged atoms (ions) that envelops the Earth and extends from roughly 50 kilometers to 1000 kilometers altitude. Incoming solar radiation with frequencies within and above those of the ultraviolet regime contain photons with enough energy to ionize a neutral gas atom. The process of recombination, in which an ion is captured by a free electron, occurs simultaneously with the ionization process. At lower altitudes, where the gas density is larger, and the molecules are closer together, recombination time constants are shorter than at higher altitudes.

The rate of ionization is largely dependent on the amount of solar radiation that the ionosphere receives. For instance, the sunspot cycle of the sun, season of the local ionosphere, WGS-84 position, and time of day are all factors impacting how much solar radiation a given part of the ionosphere receives. During the day, when the local ionosphere receives large amounts of solar radiation, the ionosphere has a large electron content and the density of electrons at various altitudes is generally larger. Conversely, at night, when the local ionosphere receives virtually no solar radiation, the ionosphere has a low electron content with very low densities at the lowest altitudes. Figure 1 illustrates the differences between the local daytime and nighttime ionospheres.

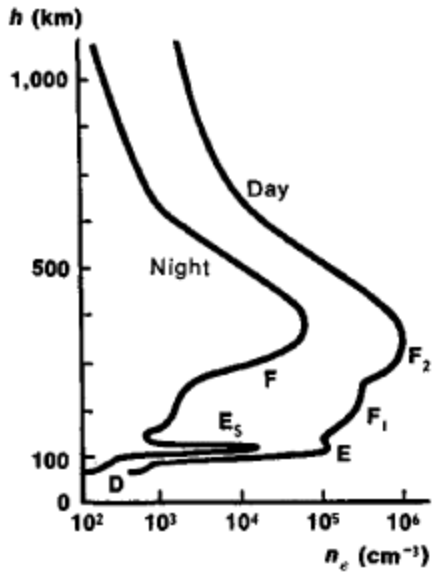

Figure 1: Example daytime and nighttime ionosphere vertical electron density profiles [13]

The nighttime decrease in electron density is apparent in that the nighttime electron density profile is closer to the vertical axis than the daytime electron density profile. Integrating the electron density from an altitude of 50 kilometers to 2000 kilometers will yield the Vertical Total Electron Content (VTEC). For practical numerical integration purposes, it is unnecessary to consider altitudes outside of the 50 to 2000-kilometer range in the integral due to them having negligible electron densities.

1.3 The Chapman Profile as a Vertical Electron Density Profile Model

Figure 1 gives typical electron density profiles for both the daytime and nighttime. While the altitude of peak electron density may shift, or the overall total electron content could change, the general shape of the profile will remain relatively constant with the exception of the E layer, which may be hard to distinguish against a significant F1 layer during the day while appearing more pronounced during the night. Given the constancy of the shape of the profile, it would be convenient to fit a true electron density profile with a parameterized model that reflects important aspects of the ionosphere's electron density profile such as the VTEC, F layer thickness, and height of peak electron density. There are several global and local ionosphere models that are used today. The Chapman vertical profile is a model that is well-suited for this study. Chief among its benefits is that it only requires three parameters to define, whereas other models such as the Booker Profile, require many more. This small number of parameters is very useful when applying model-based estimation techniques to the ionosphere. Figure 2 depicts an example Chapman Profile:

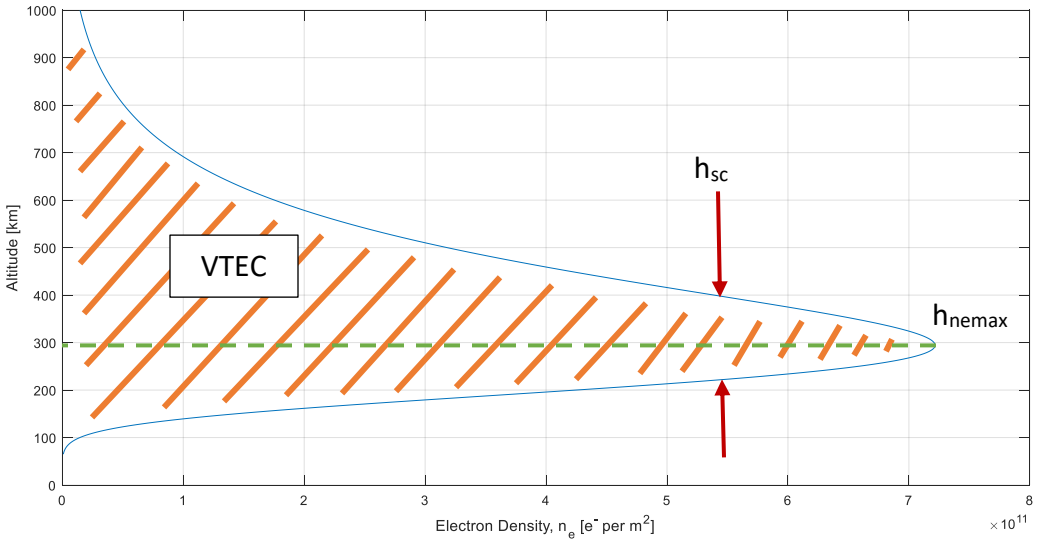

Figure 2: Example Chapman Profile and its three parameters.

Figure 2 illustrates the three parameters needed to construct a Chapman Profile. The aforementioned VTEC and altitude of peak electron density, h_{nemax}, are shown as well as the scale height h_{sc}, which is a measure of the profile's thickness. A corresponding quantity is the nondimensional altitude, $z(h) = \frac{h-h_{nemax}}{h_{sc}}$, which measures the signed distance from the height of peak electron density to the altitude of interest in units of scale heights.

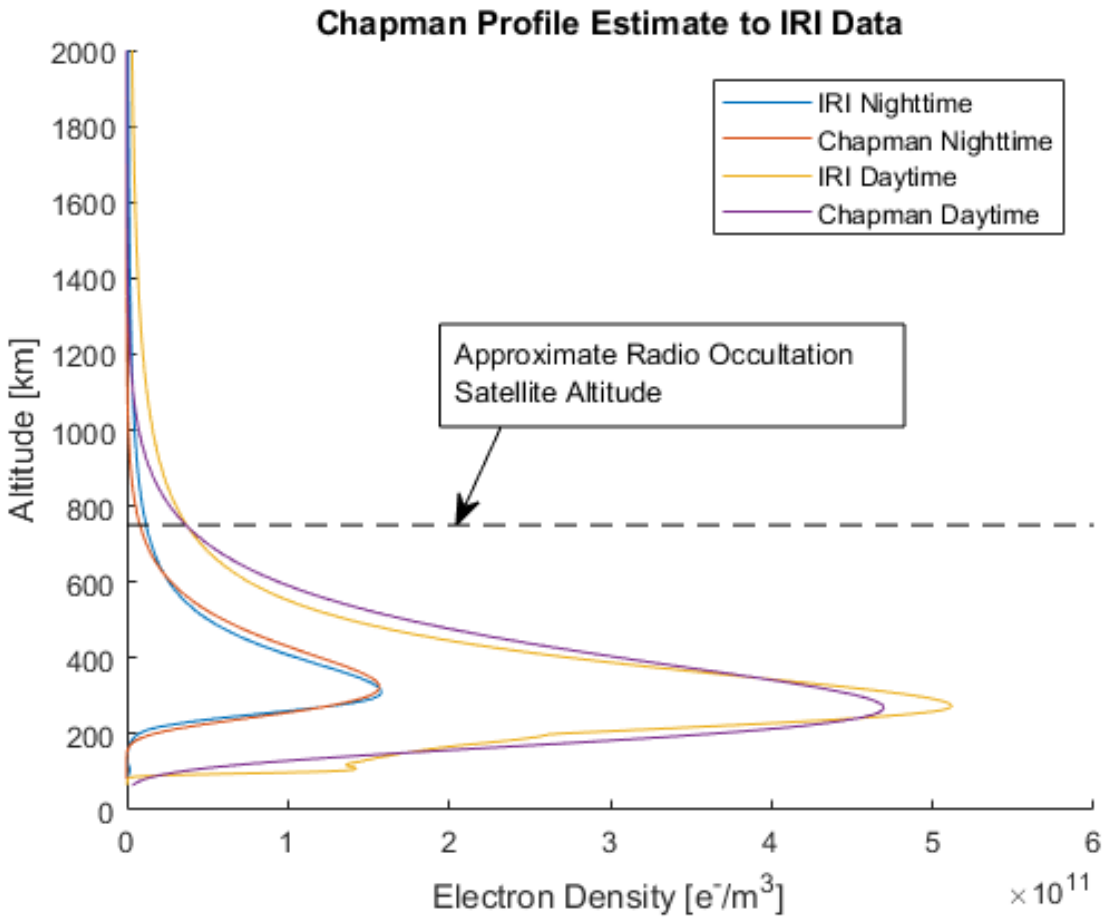

Figure 3: Example Chapman Profile fits of daytime and nighttime ionosphere profiles.

One of the largest shortcomings of approximating a vertical electron density profile using a Chapman Profile is shown in Fig. 3. The Chapman Profile fails to model the D and E layer "hump" at approximately 100 kilometers altitude. However, the Chapman Profile provides a reasonable fit above the D and E layers.

Chapman Profiles are used to model the ionosphere regularly and have been shown to provide good fits for vertical profile data [14] and have been used in part to model a 3-D ionosphere [15].

1.4 Outline of Remainder of Thesis

The remainder of the thesis will introduce the estimation problem and algorithm in Chapter 2. The thesis will demonstrate the estimator's capabilities on a test dataset in Chapter 3. It will apply the estimator to the eclipse problem in Chapter 4, and that chapter will also analyze the eclipse results. Finally, Chapter 5 will contain conclusions on the research performed and suggest future work.

CHAPTER 2: NONLINEAR ESTIMATION PROBLEM DEFINITION AND BATCH FILTER SOLUTION ALGORITHM

2.0 Overview of Chapter

This section outlines the basic components of the filter. Each subsection of Chapter 2 corresponds to a key building block of the filter. Understanding of these key components of the filter is necessary in interpreting the results of the filter to come in Chapters 3 and 4.

2.1 GPS Background and Observables Model

The Global Positioning System (GPS), comprised of 32 Medium Earth Orbit (MEO) satellites, has been an invaluable tool for solving a variety of positioning, navigation, and timing (PNT) problems since it became operational in 1996. Even beyond its applications in the PNT domain, GPS is a tool used to solve many other types of problems, including those within the atmospheric

remote-sensing realm. While in transit from the transmitting satellite to the receiver, a GPS signal is delayed due to its interaction with the portion of the ionosphere that it passes through (among other delay sources). When estimating the position of the GPS receiver, the amount of delay due to the ionosphere must be estimated, too, with the sole purpose of obtaining a more accurate position estimate. However, estimation and removal of ionospheric effects on a signal leads naturally to the concurrent estimation of the slant total electron content along the line of sight vector to the corresponding GPS satellite [2].

Given a properly tracked GPS signal on either the L1 or L2 frequencies, a receiver can compute the range-equivalent difference between the signal's time of transmission, t^S, and its time of reception, t_R, $p = c(t_R - t^S)$, or the pseudorange. The pseudorange is not the true range between the receiver and the satellite due to various delay sources:

$$p = \rho + c(\delta_R - \delta^S) + I_\rho(\omega) + \varepsilon_\rho \tag{2.1}$$

where c is the speed of light, δ_R and δ^S are the respective receiver and satellite clock errors, $I_\rho(\omega)$ is the range-equivalent ionospheric group delay, and ε_ρ is the sum of other delays whose magnitudes are not directly dependent on the carrier frequency (e.g. multipath, or tropospheric delays).

The beat carrier phase of the GPS signal can also be observed, and the range-equivalent beat carrier phase can be modeled as:

$$\lambda_\omega \varphi_\omega = \rho + c(\delta_R - \delta^S) - I_\varphi(\omega) + \lambda_\omega \beta_\omega + \varepsilon_\varphi \tag{2.2}$$

where λ_ω is the carrier frequency's wavelength, φ_ω is the beat carrier phase, $I_\varphi(\omega)$ is the range-equivalent ionospheric carrier phase advance, β_ω is a frequency-specific bias that represents the difference in the initial carrier phase of the transmitting satellite and the receiver's initial carrier phase replica. Finally, ε_φ is the sum of other delays whose magnitudes are not directly dependent on the carrier frequency.

2.2 TEC Measurement and Model

TEC measurements are the measurements used in the estimation procedure presented in this study. TEC is the count of the number of free electrons within a particular region. Specifically, for a GPS satellite/receiver link, it is the electron content within a 1m-by-1m column that encloses the line of sight between the satellite transmitter antenna and the receiver antenna. Numerically, it is the integral with respect to distance of the electron density value along the line-of-sight path. Given an electron density in electrons/m^3, the corresponding TEC is given in electrons/m^2. This study considers two different types of slant TEC measurements: slant-TEC from a ground-based receiver and slant-TEC from an orbiting RO receiver. For example, Fig. 2 illustrates the shaded area that constitutes the TEC integral. It is called Vertical TEC (VTEC) because the GPS satellite is directly overhead. Thus, slant TEC refers to TEC along any line-of-sight path, regardless of its orientation. VTEC applies only to a line-of-sight path that is vertical, i.e., to a satellite that has an elevation of 90 deg above the local horizon.

RO slant-TEC measurements are similar to ground-based slant-TEC measurements, except that they are the total electron content contained within the path that a GPS signal takes from a GPS spacecraft to an orbiting spacecraft that carries the RO receiver. As seen in Fig. 2, RO satellites orbit at a roughly median altitude of 750 kilometers. The defining geometry of a typical RO measurement is such that there is often some altitude along the line of sight from the LEO satellite to the GPS satellite that is less than the orbiting altitude of both satellites. The assimilation of ground-based slant TEC measurements (having roughly vertical lines of sight) with RO slant TEC measurements (approximately horizontal lines of sight) is an important feature of this study, as it allows the estimator to “fill in the gaps” of information that would have been left open if solely one or the other measurement had been used.

The CORS network is a set of stationary ground-based dual-frequency receivers mainly located in the United States that provide carrier phase and pseudorange measurements to the end user.

The network is made up of nearly 2,000 stations and provides data at various rates ranging from once per second to once per minute.

Several satellite programs are active that provide radio occultation measurements with dual-frequency GPS receivers onboard. The most prominent program is the joint United States/Taiwan endeavor, COSMIC. When launched in April 2006, there were six satellites in highly inclined orbits gathering radio occultation data. However, as of 2017, only two of the initial six satellites remained. Other satellite programs that collect radio occultation data to be used in this study are GRACE, MetOp-A, MetOp-B, and TerraSAR-X [16].

Most positioning, navigation and timing (PNT) problems treat the $I_\rho(\omega)$ and the $I_\varphi(\omega)$ terms in Eqs. (2.1) and (2.2) as nuisance parameters that must be estimated in order to deduce other quantities, such as the true range between a GPS satellite and a receiver. The same receiver calculations that remove ionosphere effects can be modified such that $I_\rho(\omega)$ and $I_\varphi(\omega)$ are the output quantities of the receiver, where $\beta_{I\varphi}$ is an unknown constant bias in the carrier-phase-based measurement of the ionosphere effect. The receiver's ability to estimate these quantities is independent of its ability to estimate its position.

The range-equivalent ionospheric group delay and the range-equivalent ionospheric carrier phase advance are effectively identical at GPS frequencies and can be expressed in terms of the TEC associated with the signal's path from transmission to reception and its carrier frequency ω:

$$I_\rho(\omega) = I_\varphi(\omega) = \frac{40.3TEC}{(\omega/[2\pi])^2} \tag{2.3}$$

where *TEC* is the total electron content in units of electrons/m^2, and ω is the frequency given in units of radians/sec. The group delay and carrier phase advance are both given in units of meters. The two frequencies of interest are the GPS L1 frequency, $\omega_{L1} = (2\pi)1575.42\text{x}10^6$ radians/sec, and the GPS L2 frequency, $\omega_{L2} = (2\pi)1227.6\text{x}10^6$ radians/sec.

With the use of dual-frequency GPS receivers, signals on both the L1 and L2 frequencies can be processed simultaneously. The pseudorange observed on the L1 frequency can be subtracted from the pseudorange observed on the L2 frequency to yield the following equation after substitution of Eq. (2.1) into the difference formula:

$$p_{L2}^{j} - p_{L1}^{j} = \frac{40.3TEC}{(\omega_{L2}/[2\pi])^2} - \frac{40.3TEC}{(\omega_{L1}/[2\pi])^2} \tag{2.4}$$

where the superscript *j* denotes pseudoranges observed from GPS satellite *j.* Note that all other terms in Eq. (2.1) will cancel because they are only dependent on satellite/receiver geometry and not the carrier-frequency. Rearranging Eq. (2.4) yields a direct expression for the pseudorange-based slant TEC [2]:

$$TEC_{pr} = \frac{\omega_{L1}^2\omega_{L2}^2}{40.3(2\pi)^2(\omega_{L1}^2-\omega_{L2}^2)}(p_{L2}^{j} - p_{L1}^{j}) \tag{2.5}$$

Equation (2.5) provides a straightforward expression for the measured slant TEC along a line of sight that is easily deduced from the two observed pseudoranges. However, the pseudorange-based TEC is noisy and not the best possible measurement for direct use in estimation algorithms.

In order to extract a less noisy TEC value, the beat carrier phase observables on the L1 and L2 frequencies must also be considered. In a similar manner to how Eq. (2.5) has been derived, the following equation gives an expression for the carrier-phase-based slant TEC measurement between the receiver and GPS satellite *j* [2]:

$$TEC_{carrier} = \frac{\omega_{L1}^2\omega_{L2}^2}{40.3(2\pi)^2(\omega_{L1}^2-\omega_{L2}^2)}\left(\lambda_{L1}\varphi_{L1}^{j} - \lambda_{L2}\varphi_{L2}^{j}\right) + \tilde{\beta} \tag{2.6}$$

where $\tilde{\beta}$ is the combination of the two frequency-specific biases such that $\tilde{\beta} = \frac{\omega_{L1}^2\omega_{L2}^2}{40.3(2\pi)^2(\omega_{L1}^2-\omega_{L2}^2)}(\lambda_{L2}\beta_{L2}^{j} - \lambda_{L1}\beta_{L1}^{j})$. The carrier-phase-based TEC value contains less noise. However, it is biased by the unknown constant value $\tilde{\beta}$. Given a time history of TEC_{pr} and $TEC_{carrier}$, a reasonable less noisy nonbiased estimate of the TEC between the satellite and the receiver can be extracted. The remainder of Chapter 2 contains further discussion and an example for how this slant TEC value is computed.

2.3 Ionosphere Electron Density Model Using Bi-Quintic Spline and the Chapman Profile

The goal of the algorithm developed in this study is to construct a reliable global 3D electron density profile, $N_e(\mathbf{r};\mathbf{p})$. Any vertical profile could be used; however, the Chapman Profile is an excellent choice due to its dependence on only three parameters: VTEC, h_{nemax} (or h_{pk}), h_{sc}. The 3D electron density profile is created by combining the Chapman Profile with a latitude and longitude bi-quintic spline, as defined in [18]. Let $N_{echap}(h;\mathbf{p}_{chap})$ be a Chapman Profile that is a function of altitude, h, and the 3-element parameter vector, $\mathbf{p}_{chap}$. The 3-element parameter vector varies with latitude φ, and longitude λ and is itself a function of a separate parameter vector, **p**. So, the global electron profile is expressed as $Ne\{h(\mathbf{r});\mathbf{p}_{chap}[\varphi(\mathbf{r}),\lambda(\mathbf{r});\mathbf{p}]\}$.

Physically, it is impossible for any of the three elements of $\mathbf{p}_{chap}$ to be nonpositive. In practice, the elements of $\mathbf{p}_{chap}$ are expressed as

$$\boldsymbol{p}_{chap}(\phi,\lambda;\mathbf{p}) = f[\boldsymbol{p}_{fchap}(\phi,\lambda;\mathbf{p})] \tag{2.7}$$

where $\boldsymbol{p}_{fchap}$ is a splined function that can take on both positive and negative values, and $f(\boldsymbol{p}_f) = 0.5 * \boldsymbol{p}_f + log[2\,cosh(0.5a\boldsymbol{p}_f)]/a$ is a continuous approximation of $f(\boldsymbol{p}_f) = \boldsymbol{p}_f$ if $\boldsymbol{p}_f > 0$ or 0 if $\boldsymbol{p}_f \leq 0$. Thus, $\boldsymbol{p}_{chap}$ from Eq. (2.7), which is used in the Chapman profile, is guaranteed to be positive even though the bi-quinitic splined function $\boldsymbol{p}_{fchap}$ can take on any sign. Essentially, Eq. (2.7) protects the algorithm from producing any nonpositive Chapman parameters.

The function $\boldsymbol{p}_{fchap}$ is modeled with a bi-quintic latitude/longitude spline of the form:

$$\boldsymbol{p}_{fchap} = \sum_{j=1}^{6} \boldsymbol{p}_{1j} s_{spj}(\phi,\lambda) + \sum_{i=2}^{M-1}\sum_{j=1}^{9} \boldsymbol{p}_{ij} s_j(\phi,\lambda,\pi_i) + \sum_{j=1}^{6} \boldsymbol{p}_{Mj} s_{npj}(\phi,\lambda) \tag{2.8}$$

where s_{spj}, s_j, s_{npj} are the basis functions of the spline. The functions s_{spj} and s_{npj} are specific to the south and north pole, respectively, while s_j is applicable to all of the other latitude/longitude nodes. The $\mathbf{p}_{ij}$ vectors in Eq. (2.8) are the elements of the complete bi-quintic spline parameter vector:

$$\boldsymbol{p} = \begin{bmatrix} \boldsymbol{p}_{11} \\ \boldsymbol{p}_{12} \\ \vdots \\ \boldsymbol{p}_{16} \\ \boldsymbol{p}_{21} \\ \boldsymbol{p}_{22} \\ \vdots \\ \boldsymbol{p}_{29} \\ \boldsymbol{p}_{31} \\ \vdots \\ \boldsymbol{p}_{(M-1)9} \\ \boldsymbol{p}_{M1} \\ \boldsymbol{p}_{M2} \\ \vdots \\ \boldsymbol{p}_{M6} \end{bmatrix} \tag{2.9}$$

Equation (2.9) contains parameter vector components for *M – 2* regular nodes and 2 special nodes, one for each of the poles. Each $\boldsymbol{p}_{ij}$ vector contains three elements, thus the $\boldsymbol{p}$ vector contains 3(9M-6) elements.

The nature of the bi-quintic spline drives the need for nine spline functions for each regular spline node. The bi-quintic latitude/longitude spline of an arbitrary function, $a(\phi, \lambda)$ requires the function value, a, as well as eight partial derivatives, $\frac{\partial a}{\partial \phi}$, $\frac{\partial a}{\partial \lambda}$, $\frac{\partial^2 a}{\partial \phi^2}$, $\frac{\partial^2 a}{\partial \lambda^2}$, $\frac{\partial^2 a}{\partial \lambda \partial \phi}$, $\frac{\partial^3 a}{\partial \lambda^2 \partial \phi}$, $\frac{\partial^3 a}{\partial \lambda \partial \phi^2}$, and $\frac{\partial^4 a}{\partial \lambda^2 \partial \phi^2}$. The eight partial derivatives combined with the function value make up the coefficients of the nine basis functions at each node [18].

With the exception of the two nodes at the poles, nodes are placed on sets of small circles of latitude with somewhat arbitrary longitudinal spacing. In this specific study, it is wise to concentrate more nodes over CONUS, as this is where the ground stations are located, and where the eclipse passes over. A larger total node count could increase the granularity of the map but comes with a price as it adds more parameters to estimate. Figure 4 shows the specific nodes used in this study.

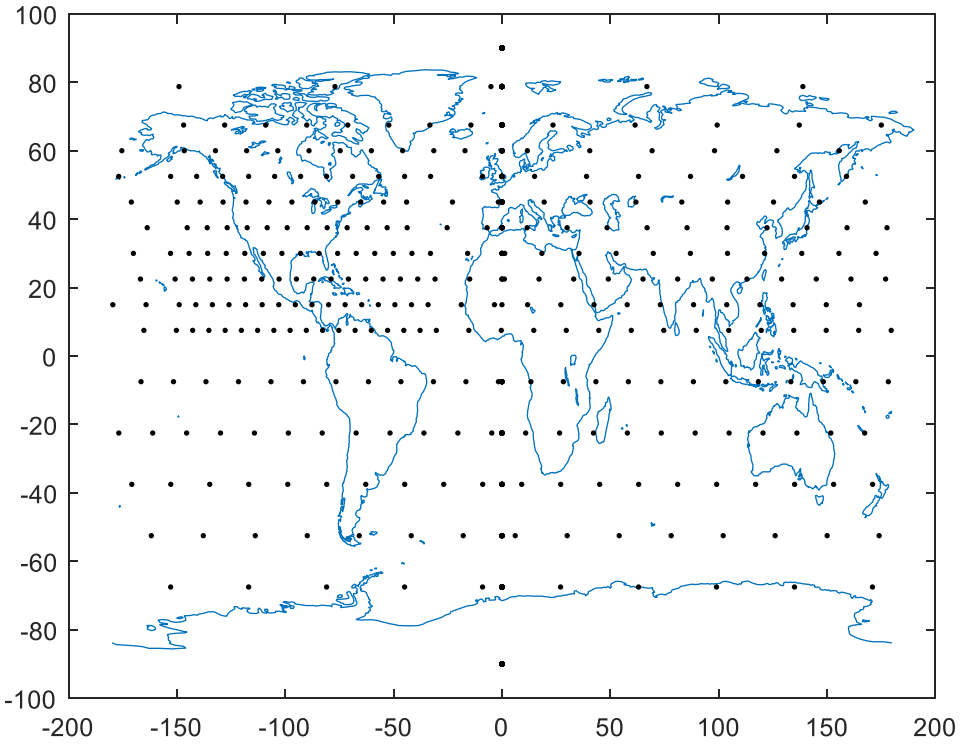

Figure 4: Bi-quintic spline node locations.

Suppose that the splined value $a_0(\lambda)$ is desired between two longitude nodes, λ_1 and λ_2, with $\Delta\lambda_{12} = \lambda_2 - \lambda_1$ and $\tau(\lambda) = (\lambda - \lambda_1)/\Delta\lambda_{21}$. Then, the one-dimensional spline is:

$$\begin{aligned} a_0(\lambda) = {} & a_1[1 - 10\tau^3(\lambda) + 15\tau^4(\lambda) - 6\tau^5(\lambda)] + a_2[10\tau^3(\lambda) - 15\tau^4(\lambda) + 6\tau^5(\lambda)] \\ & + \left.\frac{\partial a}{\partial \lambda}\right|_1 \Delta\lambda_{21}[\tau(\lambda) - 6\tau^3(\lambda) + 8\tau^4(\lambda) - 3\tau^5(\lambda)] \\ & + \left.\frac{\partial a}{\partial \lambda}\right|_2 \Delta\lambda_{21}[-4\tau^3(\lambda) + 7\tau^4(\lambda) - 3\tau^5(\lambda)] \\ & + \left.\frac{\partial^2 a}{\partial \lambda^2}\right|_1 \Delta\lambda_{21}^2[0.5\tau^2(\lambda) - 1.5\tau^3(\lambda) + 1.5\tau^4(\lambda) - 0.5\tau^5(\lambda)] \\ & + \left.\frac{\partial^2 a}{\partial \lambda^2}\right|_2 \Delta\lambda_{21}^2[0.5\tau^3(\lambda) - \tau^4(\lambda) + 0.5\tau^5(\lambda)] \end{aligned} \tag{2.10}$$

With Eq. (2.10), the bi-quintic spline calculation can be carried out. Suppose that the desired parameter value, a_0, lies between the four points: (ϕ_i, λ_i), (ϕ_i, λ_j), (ϕ_k, λ_k), and (ϕ_k, λ_l). Respectively, these points represent the southwest, southeast, northwest and northeast points closest to the location of interest. The procedure to calculate a_0 using the bi-quintic spline is as follows: Perform two separate λ splines of the function value, one along the lower circle of latitude at ϕ_i and the other along the higher circle at latitude ϕ_k so that two new function values are created at the desired line of longitude. Similarly, perform λ spline calculations in order to compute $\frac{\partial a}{\partial \phi}$ and $\frac{\partial^2 a}{\partial \phi^2}$ on the lower ϕ_i latitude small circle and on the upper ϕ_k latitude small circle to yield these two latitude partial derivative values at the ϕ_i and ϕ_k latitude points on the same line of longitude. Finally, perform a one-dimensional quintic spline of the function value in the ϕ latitude direction to the final desired latitude to get a_0. A similar procedure is used if one of the closest nodes is the north or south pole. However, a special technique must be used to compensate for the lack of a fourth node point to interpolate between [18].

2.4 Slant TEC Measurement Models

2.4.1 Ground-Based GPS Receivers

In order to estimate the ionosphere parameter vector **p**, a model is needed that predicts the slant TEC that would be measured through the parameterized ionosphere model along any given line-of-sight path from a satellite to a receiver. The batch estimation filter can then compare predicted slant TEC values with actual measured values and adjust its parameter estimations until the predicted values agree well with the measured values. Suppose one is given a perfect model of the electron density profile, $N_e(\boldsymbol{r};\boldsymbol{p})$, the position of the ground station making the k^{th} measurement, $\boldsymbol{r}_{gsk}$, the unit vector pointing in the direction from the receiver to the corresponding GPS satellite, $\hat{\boldsymbol{r}}_k$, and the distance to the GPS satellite, ρ_k. Then the k^{th} slant TEC measurement is modeled by the equation:

$$\tilde{h}_{STECk} = \int_0^{\rho_k} N_e\left[\left(\boldsymbol{r}_{gsk} + \rho\hat{\boldsymbol{r}}_k\right); \boldsymbol{p}\right] d\rho \tag{2.11}$$

In practice, the definite integral in Eq. (2.11) is numerically approximated via quadrature integration based on a one-dimensional electron density distribution (the distribution along the line of sight from the receiver to the satellite) and a set of L grid points that lie along the line of sight vector $\{\rho_{k0}, \ldots, \rho_{kL}\}$. Associated with each grid point is a unique electron density and electron density derivative with respect to ρ: N_{ekl} and N'_{ekl}. The slant TEC is then approximated using the quadrature integration formula:

$$\tilde{h}_{STECk}(\boldsymbol{p}) \approx \sum_{l=0}^{L-1} \frac{\Delta\rho_{kl}}{2}\left[N_{ekl} + N_{ek(l+1)} + \frac{\Delta\rho_{kl}}{6}\left(N'_{ekl} - N'_{ek(l+1)}\right)\right] \tag{2.12}$$

where $\Delta\rho_{kl} = \rho_{k(l+1)} - \rho_{kl}$.

The grid points are selected to lie at pre-determined $z(h)$ locations along the Chapman Profile. Ref. [4] discusses the methods used to arrive at the specific pre-selections. It states that the relative accuracy in using them is better than 1 part in 10,000. Figure 5 illustrates the numerical

integration procedure. Note that any line-of-sight path other than a vertical path will pass through a varying set of latitudes and longitudes on its way from the receiver to the satellite. Therefore, each different quadrature integration point will use slightly different Chapman profile parameters to compute its N_{ekl} value and its N'_{ekl} derivative. Note, also, that the N'_{ekl} derivative is computed using the chain rule and the dot product between the $\hat{\mathbf{r}}_k$ direction and the gradient of N_{ekl} evaluated at the quadrature integration point.

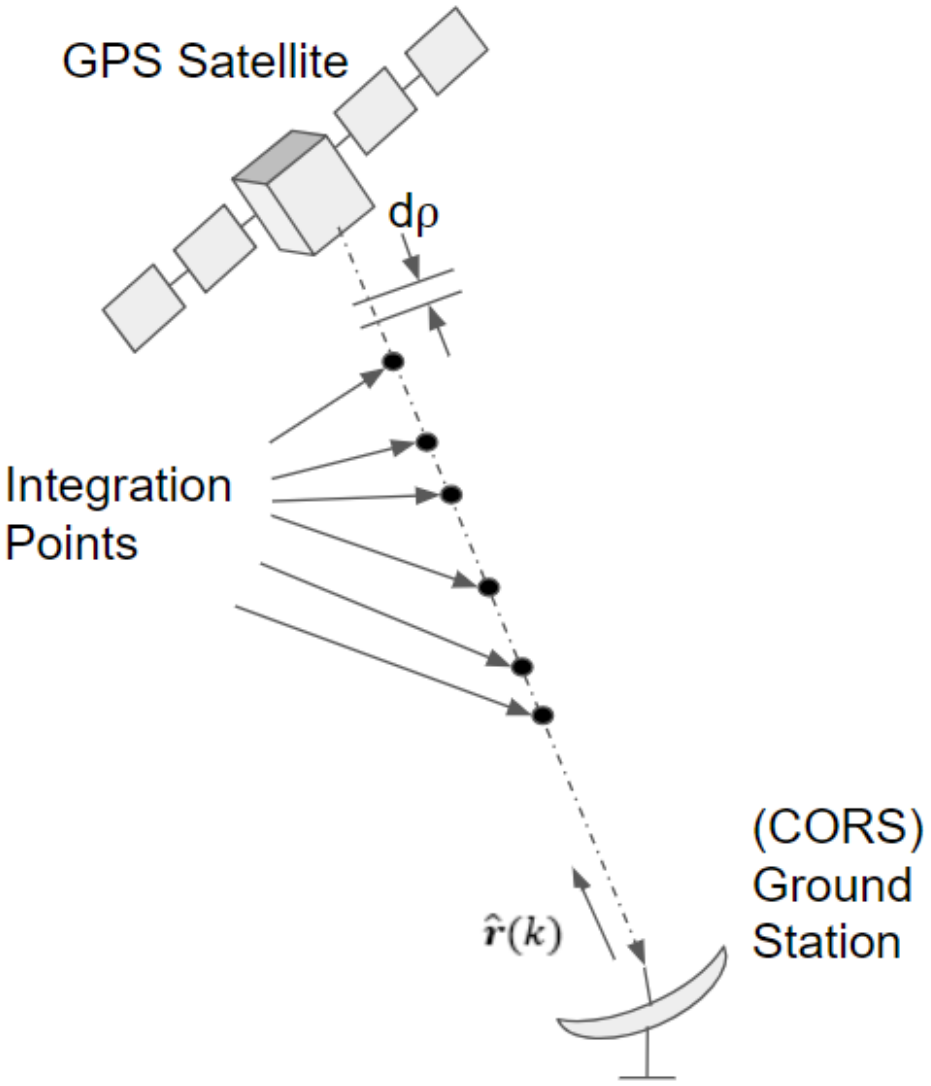

Figure 5: Slant TEC numerical integration along a line-of-sight path.

Embedded within the measurement reported by each CORS receiver is an inter-channel TEC bias, $b_{q(k)}$, for the $q(k)^{th}$ receiver, which is the receiver that applies for the k^{th} measurement. Typically, multiple measurements come from any given receiver so that the same output value of the integer function *q(k)* is produced for multiple k input values. There is also measurement noise, v_k. The full slant-TEC measurement model equals the sum of the numerically integrated slant TEC, the receiver's TEC bias, and measurement noise:

$$y_k = \tilde{h}_k(\boldsymbol{p}) + b_{q(k)} + v_k \tag{2.13}$$

The measurement noise is assumed to be sampled from a zero-mean Gaussian distribution with standard deviation σ_{vk}. Note that each GPS satellite also has a differential code bias (DCB) similar to $b_{q(k)}$. These biases are known beforehand and subtracted from corresponding TEC measurements before estimation. Hence, the GPS satellite DCBs do not appear in any of the equations presented.

2.4.2 Orbiting-Radio Occultation Receivers

A radio occultation measurement is a slant TEC measurement made from an orbiting satellite. A satellite with a dual-frequency GPS receiver (typically in LEO) receives a GPS signal that traversed through the ionosphere. Note that while a satellite does not necessarily need to be in LEO for a radio occultation, this paper will denote the 3-dimensional position of the satellite carrying the dual-frequency receiver as $\boldsymbol{r}_{LEO}$ because all occulting satellites in this study are in LEO. A radio occultation is strictly defined such that there must exist a point along the line of sight between the GPS satellite and the receiver that is lower in altitude than the receiver's altitude. Not only will these GPS receivers track occulted signals, but they will also track signals from overhead that do not meet the strict criteria for being a radio occultation. That is, the altitude of each point along the line of sight strictly increases when tracing it from the receiver to the GPS satellite (see Fig. 5). While these measurements do not pass through as much of the ionosphere as radio occultations, they still contain information about the ionosphere and will be

used in the estimation algorithm and processed the exact same way as slant TEC measurements from ground-based receivers.

The formula for the radio occultation integral with a parameterized model of the ionosphere electron density profile is very similar to the slant TEC integral from Eq. (2.11):

$$\tilde{h}_{ROk} = \int_0^{\rho_k} N_e[(\boldsymbol{r}_{LEOk} + \rho\hat{\boldsymbol{r}}_k); \boldsymbol{p}]d\rho \tag{2.14}$$

Again, this definite integral will be approximated using quadrature numerical integration techniques in order to implement it in software. A method has been developed for this study that uses the 3-dimensional position of a pseudo receiver location. This location is the point of minimum altitude along the line of sight from the LEO satellite to the GPS satellite, as identified in Fig. 6.

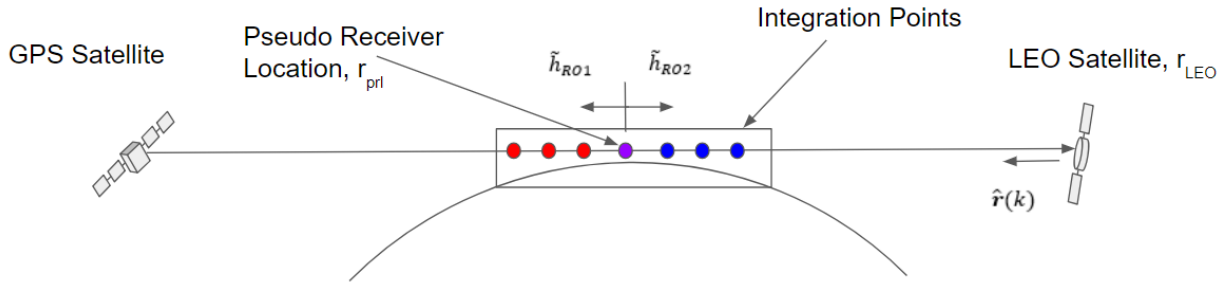

Figure 6: The geometry of a radio occultation measurement model numerical integration.

The pseudo receiver's position is the solution to the minimization of the cost function given in Eq. (2.15).

$$J_{ro} = (\boldsymbol{r}_{GPS} * (1-\alpha) + \boldsymbol{r}_{LEO} * \alpha)^T W(\boldsymbol{r}_{GPS} * (1-\alpha) + \boldsymbol{r}_{LEO} * \alpha) \tag{2.15}$$

where α is the scaled distance of the pseudo receiver location along the line of sight from the GPS satellite (α = 0) to the LEO satellite (α = 1). W is a diagonal weighting matrix where the (1,1) and (2,2) entries are 1/A and the (3,3) entry is 1/B where A = 6378137 meters and B = 6356752 meters. The optimized α yields an approximation of the closest point to the WGS-84 ellipsoid along the line-of sight vector because A is the equatorial radius of that ellipsoid and B is its polar radius.

Given the pseudo receiver location $\boldsymbol{r}_{prl} = \boldsymbol{r}_{GPS}(1 - \alpha_{opt}) + \boldsymbol{r}_{LEO}\alpha_{opt}$, two numerical integrals are carried out to calculate the modeled TEC of the radio occultation: one from $\boldsymbol{r}_{prl}$ to the LEO satellite, and one from $\boldsymbol{r}_{prl}$ to the GPS satellite. Both integrals are carried out with quadrature integration techniques using a similar set of integration points $\{\rho_{k0}, \dots, \rho_{kL}\}$ as has been used to calculate the modeled slant TEC in Section 2.4.1:

$$\tilde{h}_{ROk}(\boldsymbol{p}) \approx \tilde{h}_{RO1} + \tilde{h}_{RO2} = \sum_{i=0}^{I-1} \frac{\Delta\rho_{ki}}{2}\left[N_{eki} + N_{ek(i+1)} + \frac{\Delta\rho_{ki}}{6}\left(N'_{eki} - N'_{ek(i+1)}\right)\right] + \sum_{j=0}^{J-1} \frac{\Delta\rho_{kj}}{2}\left[N_{ekj} + N_{ek(j+1)} + \frac{\Delta\rho_{kj}}{6}\left(N'_{ekj} - N'_{ek(j+1)}\right)\right] \quad (2.16)$$

In Fig. 6, the red points correspond to the *I-1* integration points from Eq. (2.16), the blue points correspond to the *J-1* integration points, and the purple point is the pseudo receiver location that is common to both summations in Eq. (2.16) at the points *i* = 0 and *j* = 0.

2.5 TEC Data Retrieval and Pre-Processing

As discussed in Sections 2.1 and 2.2, four observables from the j^{th} GPS satellite are used to generate a TEC measurement: p_{L2}^j, p_{L1}^j, φ_{L1}^j, and φ_{L2}^j. The National Oceanic and Atmospheric Administration (NOAA) provides near real-time day-long time histories of all four needed observables for all GPS satellites of the CORS stations. These data are provided in RINEX format. Equations (2.5) and (2.6) are used to generate time histories of TEC_{pr} and of a biased version of $TEC_{carrier}$ for each CORS receiver/GPS satellite pair. The biased $TEC_{carrier}$ value consists of the first term on the right-hand side of Eq. (2.6). The two raw TEC histories for a single pass of GPS satellite PRN 12 over CORS station *1lsu* on August 19, 2017 are shown in Fig. 7. Note that the vertical scale in Fig. 7 is given in TEC Units (TECU). 1 TECU = 10^{16} electrons/m^2.

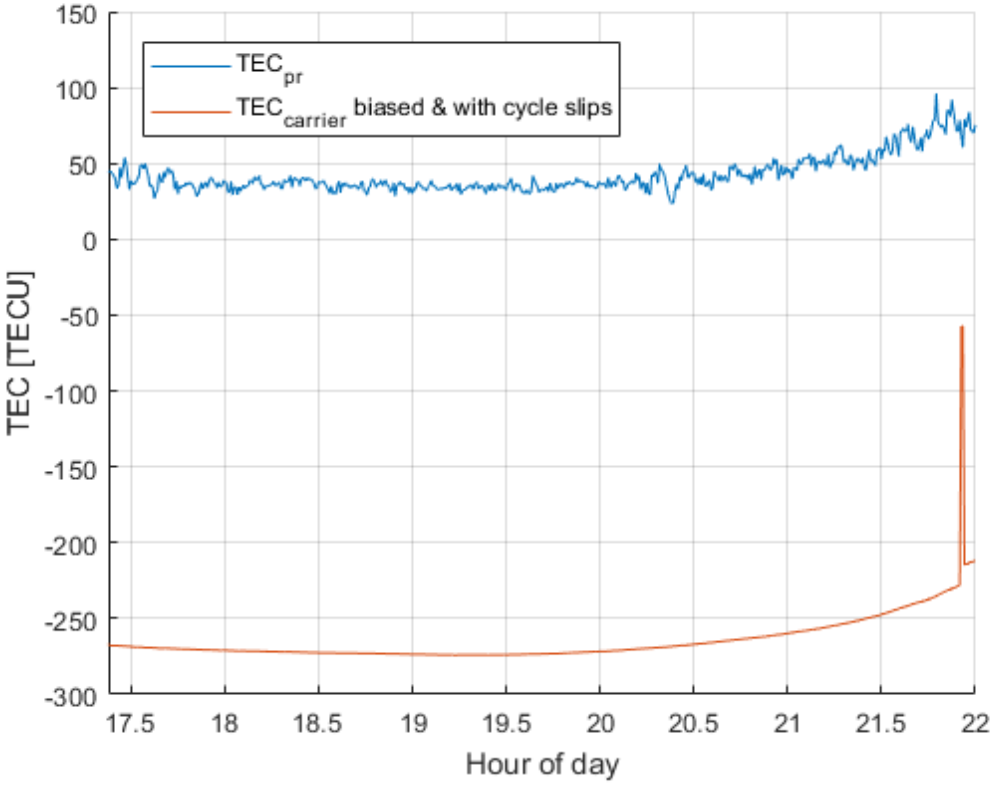

Figure 7: Time histories of TEC measurements of CORS station 1lsu and PRN 12.

As mentioned in Section 2.1, the noisy TEC_{pr} must be used with the biased $TEC_{carrier}$ to produce a more accurate TEC measurement. The respective noise of the TEC_{pr} time history and satellite-specific bias ($\tilde{\beta}$) of the $TEC_{carrier}$ time history are apparent in Fig. 7 along with occasional cycle slips that are the large jumps in $TEC_{carrier}$. In order to generate the more accurate TEC measurements, the cycle slips are first identified and removed from the $TEC_{carrier}$ time history. Afterwards, the average bias relative to the TEC_{pr} time history is computed by averaging the difference of the two curves.

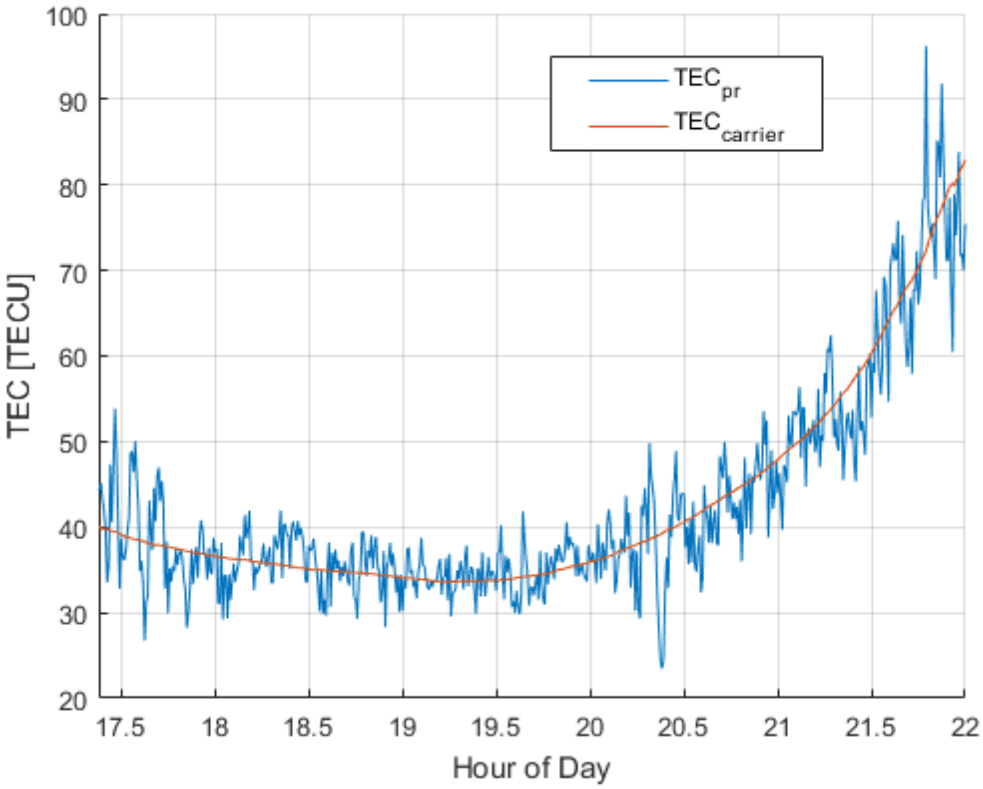

Figure 8: TEC_{pr} and cycle-slip-repaired, un-biased $TEC_{carrier}$ for CORS station 1lsu and PRN 12.

Figure 8 shows a time history of $TEC_{carrier}$ corrected for the cycle slips and the bias. These corrected values are the TEC values used as measurement inputs in the batch estimation problem that will be defined below. The bias for which these values are corrected is not to be mistaken for the inter-channel TEC bias, $b_{q(k)}$, which must be estimated by the batch estimator.

The University Corporation for Atmospheric Research (UCAR) operates the COSMIC Data Analysis and Archive Center (CDAAC). It publishes carrier-phase-based TEC measurements that have been corrected for the biases between pseudorange-based TEC values and carrier-phase-based TEC measurements for all orbiting radio-occultation receivers used in this study. That is, the calculations associated with Fig. 8 have already been carried out for orbiting radio-occultation receivers but not ground-based receivers. In addition to the TEC measurements, CDAAC provides the portions (DCBs) of $b_{q(k)}$ specific to each orbiting receiver and each GPS satellite. Therefore,

$b_{q(k)}$ for all measurements made by orbiting receivers is known and does not need to be estimated. Furthermore, the known GPS DCBs may be subtracted from the measurements made from ground-based receivers to improve the accuracy of the bias and ionosphere estimate. Along with the biases given for orbiting receivers, there is some level of uncertainty typically on the order of hundredths of a TECU (biases are typically on the order of tens of TECU). The orbiting biases are included in the estimation procedure, but, due to the small degree of uncertainty, they should not change much after the estimation procedure.

2.6 Batch-Estimation Problem Formulation

Given a set of TEC measurements, the batch filter computes an optimal estimate of the parameter vector $\boldsymbol{p}$ and the bias vector $\boldsymbol{b}$ such that their values minimize the negative-log-likelihood cost function:

$$J(\boldsymbol{p},\boldsymbol{b}) = \frac{1}{2}[\boldsymbol{y}-\boldsymbol{h}(\boldsymbol{p},\boldsymbol{b})]^T R^{-1}[\boldsymbol{y}-\boldsymbol{h}(\boldsymbol{p},\boldsymbol{b})] + \frac{1}{2}(\bar{\boldsymbol{p}}-\boldsymbol{p})^T P_{\bar{p}\bar{p}}^{-1}(\bar{\boldsymbol{p}}-\boldsymbol{p}) + \frac{1}{2}(\bar{\boldsymbol{b}}-\boldsymbol{b})^T \bar{R}_{\boldsymbol{bb}}^{-1}(\bar{\boldsymbol{b}}-\boldsymbol{b}) \quad (2.17)$$

The measurement vector, $\boldsymbol{y}$, has length (N_{measgd} + N_{measro}). The first N_{measgd} entries are the slant TEC measurements made from ground-based receivers, and the remaining N_{measro} entries are the slant TEC measurements made from orbiting-radio occultation receivers. The measurement model function, $\boldsymbol{h(p,b)}$, also has length (N_{measgd} + N_{measro}). The first N_{measgd} entries are the modeled slant TEC values whose entries are determined using Eq. (2.12). The remaining N_{measro} entries are the modeled slant TEC values whose entries are determined using Eq. (2.16). The bias vector, $\boldsymbol{b}$, has length ($N_{stationsgd}$ + $N_{stationsro}$). The first $N_{stationsgd}$ entries are the biases of the ground-based receivers, and the remaining $N_{stationsro}$ are the biases of the orbiting radio-occultation receivers. The k^{th} entry in the vector function $\boldsymbol{h(p,b)}$ models the slant TEC along the line of sight corresponding to the k^{th} measurement in $\boldsymbol{y}$. Similar in structure to $\boldsymbol{b}$, the *a priori* vector $\bar{\boldsymbol{b}}$ contains

a priori bias values that take on values of the optimal $\boldsymbol{b}$ from a previous filtering run. In the case that there is no previous filtering run, $\bar{\boldsymbol{b}}$ is a vector of all zeros. The *a priori* bias covariance matrix, $\bar{R}_{\boldsymbol{bb}}$, is diagonal when initialized on the first filter run. In the case of no *a priori* information about $\boldsymbol{b}$, the (q, q) entry of $\bar{R}_{\boldsymbol{bb}}$ is the bias error variance corresponding to the qth receiver: σ_{bq}^2.

The first term in the cost function penalizes mismatches between measured TEC values and corresponding modeled TEC values for both ground-based and orbiting measurements. The covariance matrix *R* is a diagonal matrix whose entries, r_{kk}, are equal to σ_{vk}^2, the slant TEC measurement error variance. Values ranging from 1 to 10 TECU were tried. But, ultimately, this variance is estimated to be 5 TECU - a value used in a previous study [4].

The second term in the cost function penalizes a parameter estimate that deviates far from the *a priori* parameter vector $\bar{\boldsymbol{p}}$. The matrix $P_{\bar{p}\bar{p}}$ is the *a priori* covariance matrix. These values are chosen so that the *a priori* parameter vector optimally fits the IRI model of the day of the year and time of day of the ionosphere estimate exactly one year prior. For instance, the parameter vector of an estimate of the ionosphere at 12:00 UTC on August 19, 2017 would be compared to an *a priori* parameter vector that optimally fits the IRI model for 12:00 UTC on August 19, 2016.

$P_{\bar{p}\bar{p}}$ has been designed such that an estimate is penalized for large differences between the estimated second derivatives with respect to position (i.e. the curvature) of the three Chapman profile parameters and the corresponding second derivatives for the *a priori* Chapman profile parameters. Limiting the curvature produces an estimate that is not very susceptible to large, unnatural parameter variations in a small geographic space. Additional terms in $P_{\bar{p}\bar{p}}$ apply small penalties to differences between the estimated and *a priori* values of the Chapman parameters at the bi-quintic spline nodes.

Finally, the third term penalizes receiver biases that differ from the *a priori* biases received from previous filter runs. If no *a priori* information is available, the *a priori* information is zero by default. Note that CDAAC provides the biases and associated variances for orbiting receivers. This information is handled in the filter by subtracting the known bias from the measurement in $\boldsymbol{y}$ and

letting the *a priori* bias be zero for all orbiting receivers. The (k, k) entry in $\bar{R}_{\boldsymbol{bb}}$ is the associated variance given by CDAAC.

The cost function minimization in Eq. (2.17) is equivalent to solving for the least-squares solution to the following over-determined system of nonlinear equations:

$$\begin{bmatrix} R^{-1/2}\boldsymbol{y} \\ P_{\bar{p}\bar{p}}^{-1/2}\bar{\boldsymbol{p}} \\ \bar{R}_{bb}^{-1}\bar{\boldsymbol{b}} \end{bmatrix} = \begin{bmatrix} R^{-1/2}\boldsymbol{h}(\boldsymbol{p},\boldsymbol{b}) \\ P_{\bar{p}\bar{p}}^{-1/2}\boldsymbol{p} \\ \bar{R}_{\boldsymbol{bb}}^{-\boldsymbol{1}}\boldsymbol{b} \end{bmatrix} + \boldsymbol{\nu}_{tot} \tag{2.18}$$

where $\boldsymbol{\nu}_{tot}$ is a sample from a Gaussian distribution with zero mean and identity covariance. $R^{-1/2}$, $P_{\bar{p}\bar{p}}^{-1/2}$, and $\bar{R}_{bb}^{-1}$ are the inverse square roots of R, $P_{\bar{p}\bar{p}}$, and $\bar{R}_{bb}$, respectively. These three matrices can be computed by computing the Cholesky factorization of the corresponding covariance matrix and inverting the result.

2.7 Gauss-Newton Solution Algorithm

To find a $\boldsymbol{p}$ and $\boldsymbol{b}$ that minimize the cost function in Eq. (2.17), the Gauss-Newton method [17] is used. This method is an iterative algorithm that searches for an optimal estimate based on a linearized approximation of the over-determined system of nonlinear equations in Eq. (2.18).

The algorithm begins with guesses of $\boldsymbol{p}$ and $\boldsymbol{b}$ that are typically the corresponding *a priori* vectors. The algorithm improves its guesses with vectors that decrease the cost function until either the cost changes by less than a given threshold, or a predetermined amount of maximum improvements have occurred. To find the new guess, the nonlinear system of equations in Eq. (2.18) is linearized about the current guess and the resulting overdetermined system of equations is solved for a potentially optimal $\boldsymbol{p}$ and $\boldsymbol{b}$. Then, the Gauss-Newton algorithm searches along the segment from the current ($\boldsymbol{p}$, $\boldsymbol{b}$) to the new pair of vectors. If a parameter and bias estimate pair is found that decreases the cost function in this search, the algorithm stops and selects the parameter and bias estimate pair that caused this decrease.

The nonlinear least-squares problem in Eq. (2.18) is linear in $\boldsymbol{b}$, which allows a feature to be added to the ordinary Gauss-Newton algorithm that optimizes only the bias vector first. This feature aids in achieving convergence and optimizes the bias vector exactly. The Gauss-Newton algorithm is further modified by restricting the step size between the current and new guess such that the norm of the change in $\boldsymbol{p}$ is strictly less than the current $\boldsymbol{p}$. This feature prevents initial $\boldsymbol{p}$ increments from being so large that it causes computational issues and produces absurd results.

It might be desirable to use the optimal $\boldsymbol{b}$ from a filter run as the *a priori* information in a subsequent filter run. Not only would the initial filter provide *a priori* bias vector information, but its Gauss-Newton calculations provide the *a posteriori* square-root information matrix for the errors in the optimal $\boldsymbol{b}$, $\tilde{R}_{\boldsymbol{bb}}$**.** This value is used to compute the *a posteriori* bias covariance $\bar{R}_{bb}$ via the following equation:

$$\bar{R}_{bb} = (\tilde{R}_{bb}^{-1}) * (\tilde{R}_{bb}^{-1})^{T} \tag{2.19}$$

This *a posteriori* covariance matrix would be an input to the next filter run as the *a priori* covariance matrix that is needed to define the cost function in Eq. (2.17) for the subsequent batch filter optimization problem.

CHAPTER 3: ALGORITHM PERFORMANCE

3.1 Overview of Chapter

This section evaluates the capabilities of the algorithm developed in Chapter 2 and realizes its limitations. Data from two days before the eclipse, August 19, 2017 will be used as a test dataset for the algorithm. It is important to evaluate the algorithm's performance on "normal" ionosphere conditions before analyzing results from eclipse datasets. This allows the filter to be tuned before inputting "abnormal" eclipse datasets.

3.2 Thin-shell Ionosphere Estimated VTEC

The first verification method is to compare the VTEC map produced by the filter with a thin-shell ionosphere VTEC estimate. The thin-shell estimate models the ionosphere to be an infinitely thin shell located at 350 kilometers altitude.

This verification method multiplies the measured TEC minus estimated bias from a ground-based receiver by the cosine of the angle, θ, between the line connecting the receiver to the pierce-point of the 350 thin-shell and the local vertical above the pierce point to produce a thin-shell-estimated VTEC above the receiver, $VTEC_{ts}$. If considering an array of measurements, the pierce-point angle and thin-shell-estimated VTEC of the kth measurement are $VTEC_{tsk}$ and θ_k, respectively, in Eq. (3.1):

$$VTEC_{tsk} = \left(y_k - b_{q(k)}\right) * \cos(\theta_k) \tag{3.1}$$

Slant TEC data collected August 19, 2017 at 13:23:30 UTC were input to the filter with no *a priori* bias information. $VTEC_{ts}$ was computed for each measurement using the raw ***y*** input to the filter and the optimal ***b*** determined by the filter in Eq. (3.1). Using the optimal ***p*** produced by the filter, the VTEC at each pierce-point location was determined via the bi-quintic latitude/longitude spline in Eq. (2.10). Figure 9 is a histogram of the differences between the splined *VTEC* and computed $VTEC_{ts}$ of Eq. (3.1) at each pierce-point location.

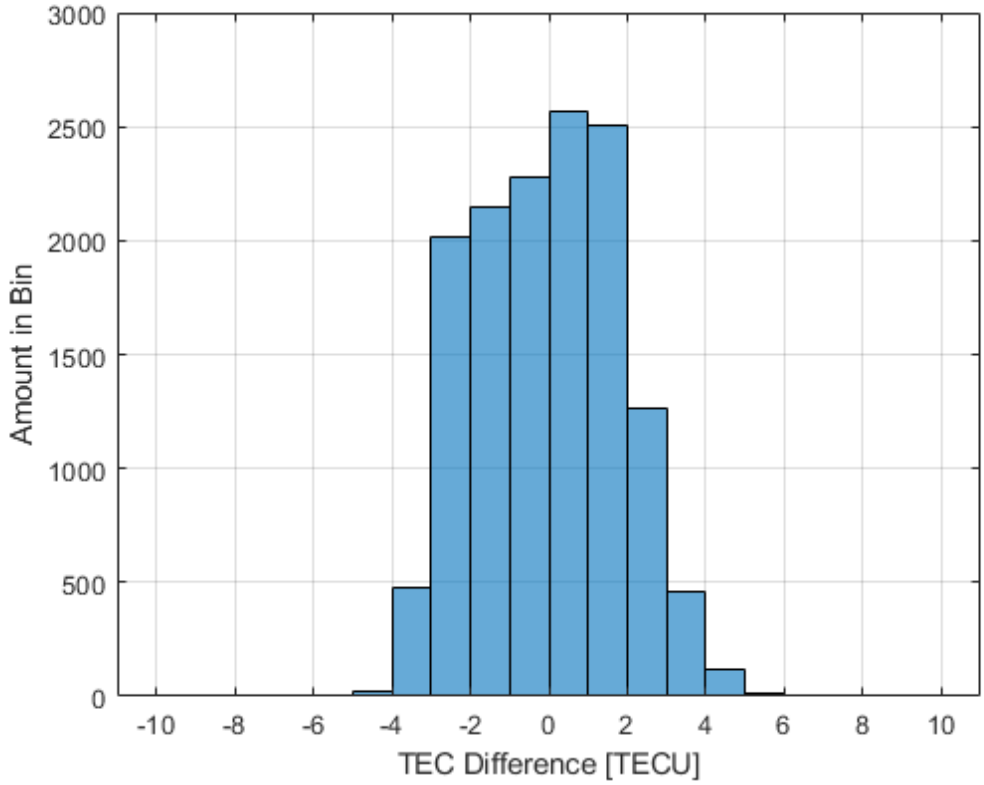

Figure 9: Distribution of differences in output VTEC map and estimated thin-shell VTEC.

The mean of the distribution in Fig. 9 is -0.06 TECU and the standard deviation is 1.8 TECU. The mean and standard deviation of the *VTEC* estimated with the optimal $\boldsymbol{p}$ is 5.90 TECU and 2.43 TECU, respectively. This distribution of residuals is reasonable. The mean is near zero and the standard deviation of the differences could be explained due to the fact that the thin-shell-estimated VTEC value is only a rough estimate. Additionally, if perfect biases were subtracted from y_k to produce $VTEC_{tsk}$, then the distribution might be tighter.

3.3 Day and Night Optimal Bias Comparison

The second verification method compared the optimal biases of the ground-based receivers from a day test case to a night test case. The biases of the dual frequency receivers do not drift very quickly. In fact, it is a valid assumption to make that over the course of several days, the biases will not drift more than fractions of a TECU. Therefore, if two test cases several hours apart are input to the filter, then it would be expected that the optimal bias vectors output in both cases would be very similar. Furthermore, if a reasonable estimate for the biases is known for the CORS receivers the day before the eclipse, the same biases may be assumed to be very close to the biases of the receivers during the eclipse. More precise bias knowledge would allow the filter to optimize the parameter vector better. Sections 3.3.1 and 3.3.2 analyze results from test cases at 13:23:30 UTC and 22:21:00 UTC on August 19, 2017. Note that the two epochs were chosen because of their relatively high concentration of radio occultation coverage above the CORS network.

3.3.1 Bias Comparison without a priori information

The algorithm optimized biases and parameters for the two test cases. The distribution of bias differences between the night and the day cases is given in Fig. 10.

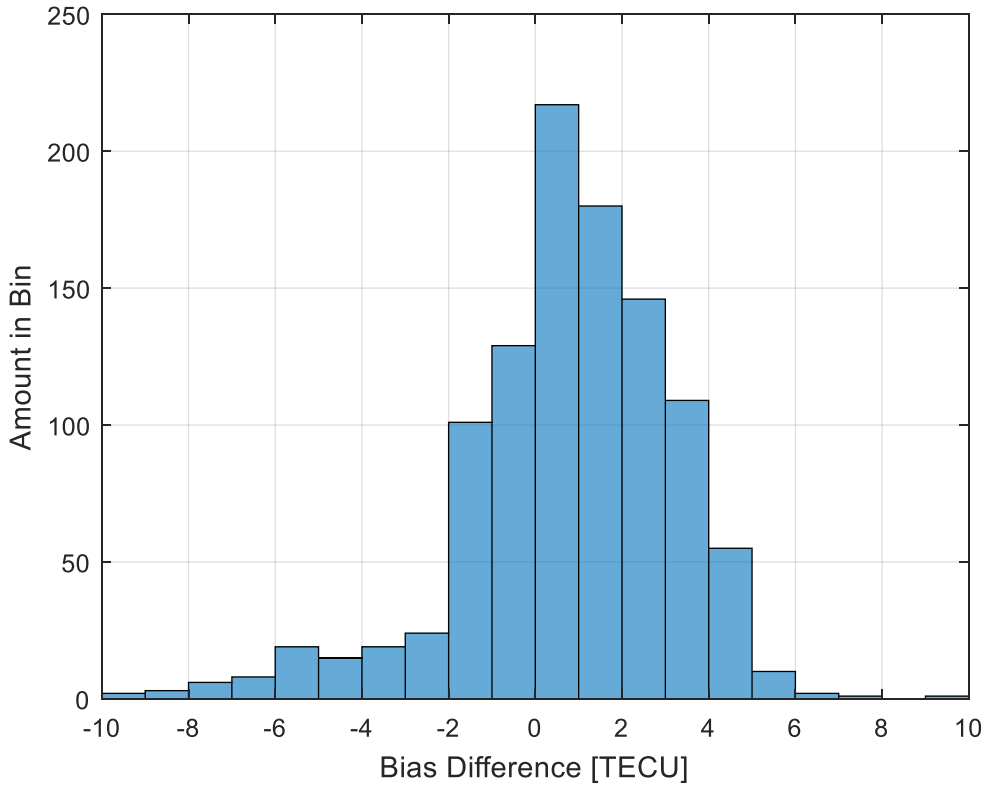

Figure 10: Nighttime bias minus daytime bias distribution.

The bias difference distribution has mean, standard-deviation, and peak values of, respectively, 0.33, 2.58, and 11.27 TECU. The slant-TEC fit errors of the daytime estimate has mean, RMS, and peak values of, respectively, 0, 2.40, and 11.76 TECU and the raw TEC (corrected for receiver biases) measurement vector has mean, RMS, minimum, and maximum values of, respectively, 7.89, 9.49, -3.02, and 35.21 TECU. The slant-TEC fit errors of the nighttime estimate

have mean, RMS, and peak values of, respectively, 0.03, 3.51, and 18.74 TECU, and the raw TEC (corrected for receiver biases) measurement vector has mean, RMS, minimum, and maximum values of, respectively, 14.61, 18.18, -3.56, and 82.07 TECU.

Note that the raw, bias-corrected TEC measurement vectors are the noisy measurements minus the estimated receiver biases. Therefore, while it is physically impossible for there to be negative TEC between a receiver and GPS satellite, negative raw, bias-corrected TEC measurements can be realistic if the measurement is too noisy and/or the estimated receiver bias is not accurate.

3.3.2 Bias Comparison when Passing Bias Estimates from One Filter Run as a priori Estimates into a Subsequent Filter Run

This section analyzes a similar scenario to Section 3.3.1. However, it takes advantage of the fact that receiver biases should not noticeably change over the course of several hours. In this comparison, the filter uses the optimized biases from Section 3.3.1 as *a priori* inputs to test cases later in the day using the methods of Section 2.7 and Eq. (2.19) to determine the appropriate R_{bb} matrix output from one run of the filter and the corresponding bias estimate $\boldsymbol{b}$ as the *a priori* $\bar{\boldsymbol{b}}$ and $\bar{R}_{\boldsymbol{bb}}$ inputs to the next run of the filter. Let the test case at 13:23:30 UTC be referred to as Day1, and the test case at 22:21:00 UTC be referred to as Night1. The optimized biases and bias covariance matrix are input into the Day2 case exactly thirty minutes after the Day1 case, at 13:53:30 UTC. Similarly, the optimized biases and bias covariance matrix that are output from the Day2 case are input as *a priori* values into the Day3 case exactly thirty minutes after the Day2 case, at 14:23:00 UTC. Similarly, the optimized biases and bias covariance matrix from Night1 are used as *a priori* for Night2 (22:51:00 UTC), and the optimized biases and bias covariance matrix from Night2 are used as *a priori* inputs for Night3 (23:21:00 UTC). The goal in adding the second and third day and night cases is to use data from Day2, Day3, Night2 and Night3 to improve the

final day and night biases. Ultimately, it would be ideal to use the estimated biases from the day before in the eclipse data so that the filter would be able to more accurately estimate the parameter vector, and uncertainty in the bias vector would be less of a nuisance. A chart of the flow of bias information is provided in Fig. 11.

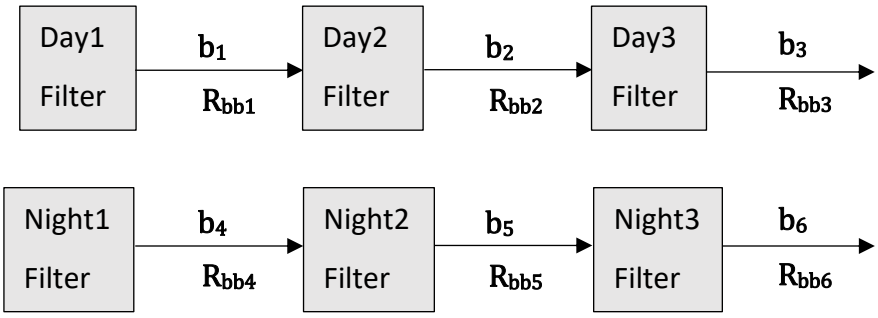

Figure 11: Flowchart of bias information through three day and three night cases.

Table 1 shows the fit statistics of this test (i.e. the measured TEC minus the modeled TEC). Clearly, the fit of the Day3 and Night3 estimates are much worse than the fits of the Day1 and Night1 estimates. Even though the RMS values of Day3 and Night3 are roughly threefold the RMS values of Day1 and Night1, they do decrease noticeably from the Day2 and Night2 values. The bias difference distribution does not improve at all with the introduction of *a priori* bias information.

	MEAN	**RMS**	**PEAK**
DAY1	0	2.40	22.14
DAY2	0.24	10.67	70.64
DAY3	0.15	9.02	85.62
NIGHT1	-0.04	3.51	20.93
NIGHT2	-0.33	12.04	70.53
NIGHT3	-0.14	10.31	94.44
NIGHT3 – DAY3 BIAS DIFFERENCE MEAN/STD./PEAK: -3.73/5.00/19.11			

Table 1: Slant-TEC fit error statistics of first test with *a priori* information.

Various solutions were attempted to improve the fit and bias differences from the first test. The second test increased the parameter vector's covariance matrix by a factor of 10 all runs.

Table 2 shows the results. The RMS values increased slightly, but for the most part, the fit statistics remained the same. However, the mean of the bias difference in the final day and night cases shifted several TECU towards zero, which is a good sign. However, the RMS and peak values are still extremely high.

	MEAN	RMS	PEAK
DAY1	0	3.35	12.04
DAY2	-0.33	10.94	69.80
DAY3	-0.18	9.50	88.72
NIGHT1	0	6.88	13.09
NIGHT2	-0.53	12.92	87.90
NIGHT3	-0.08	11.09	100.15
NIGHT3 – DAY3 BIAS DIFFERENCE MEAN/STD./PEAK: 0.44/4.30/17.19			

Table 2: Slant-TEC fit error statistics of second test with *a priori* information.

The third test was identical to the first test with the exception of the optimized bias vector and bias covariance matrix from Day3 input into Night1 as *a priori* information. Table 3 shows the results. While the RMS and peak values are still very high, the constant downward trend of the RMS and nearly constant downward trend of the peak values is promising. It is worth noting that Day2 contained 186 measurements that had extremely bad fits and differed from the model by greater than 50 TECU and Night3 only contained 27 of these extremely bad fits. All 186 extremely bad fits from Day2 originated from 38 ground-based receivers and all 27 extremely bad fits from Night3 originated from 3 ground-based receivers. The decrease in these extremely bad fits is a good sign. The decrease in the amount of receivers causing these poor fits might indicate that the bias estimate in Night3 is closer to truth than the bias estimate in Day2. This is also a good sign – as this is the purpose of performing these tests. Regardless of the downward trends, the RMS and peak values of the fits is too poor to ignore. That is, even if the fits are getting better and the bias vector estimates are seemingly improving, such a poor Night3 fit would indicate that the biases are still not close enough to being correct. Additionally, Table 3 does not include bias difference information because each subsequent test case to Day1 would be using prior biases and covariances as *a priori* information.

	MEAN	RMS	PEAK
DAY1	0	2.40	22.14
DAY2	0.24	10.67	70.64
DAY3	0.15	9.02	85.62
NIGHT1	0.12	8.40	92.90
NIGHT2	-0.53	7.50	77.48
NIGHT3	-0.08	7.01	74.56

Table 3: Slant-TEC fit error statistics of the third test with *a priori* information.

The fourth test was identical to the third test except that all receivers responsible for measurement/model mismatches were excluded from the estimation procedure. A table for these results is not included because the RMS values did not change much. Ultimately, the techniques attempted in this section did not yield any *a priori* biases or covariance matrices suitable to input into eclipse cases. However, future work should consider performing a test similar to the third test, but with many more epochs, say 20. The RMS and peak values were trending downward, but not very quickly.

CHAPTER 4: RESULTS AND DISCUSSION

4.1 Overview of Chapter

The tests performed in Chapter 3 probed the consistency of the filter during "normal" ionosphere conditions. Chapter 4 will input eclipse datasets into the filter and analyze the maps of the three Chapman profile parameters produced by the filter. These maps will help to assess how the ionosphere reacts to the eclipse. The Chapter contains four subsections, each analyzing a different part of the eclipse. The first subsection analyzes the estimated ionosphere from the beginning of the partial eclipse to the end of the beginning segment of it (from 15:46:48 UTC to 17:30:00 UTC). The second subsection analyzes the estimated ionosphere during the intermediate segment of the eclipse (from 17:30:01 UTC to 19:00:00 UTC). The third subsection analyzes the estimated ionosphere during the final segment of the eclipse (from 19:00:01 UTC to 21:04:19 UTC). In each figure, a map of the day-before's and day-after's ionosphere is averaged and subtracted from the eclipse map. This subtracted mean map is referred to as "two-day mean" in the following sections. Note that all of the figures in the following sections contain a black line of longitude that represents local noon and most figures contain a red dot (scaled up by a factor of five) that represents the position of the moon.

4.2 Comparison of Raw CORS Data Collected During the Eclipse with Data Before and After the Eclipse

Before analyzing filter results during the eclipse, the effect that the eclipse had on representative slant TEC data is examined in order to show the extent to which the eclipse affected raw measurements. Figure 12 plots the slant TEC measurement history for SV12 passes above CORS station, *wyrf*, in Casper, Wyoming the day before, of, and after the eclipse. Note that

the data is corrected for bias, $\tilde{\beta}$, but not bias $b_{q(k)}$. Recall that bias $\tilde{\beta}$ is the combination of the two frequency-specific biases in Eq. (2.6), whereas bias $b_{q(k)}$ is the unknown receiver bias that needs to be estimated.

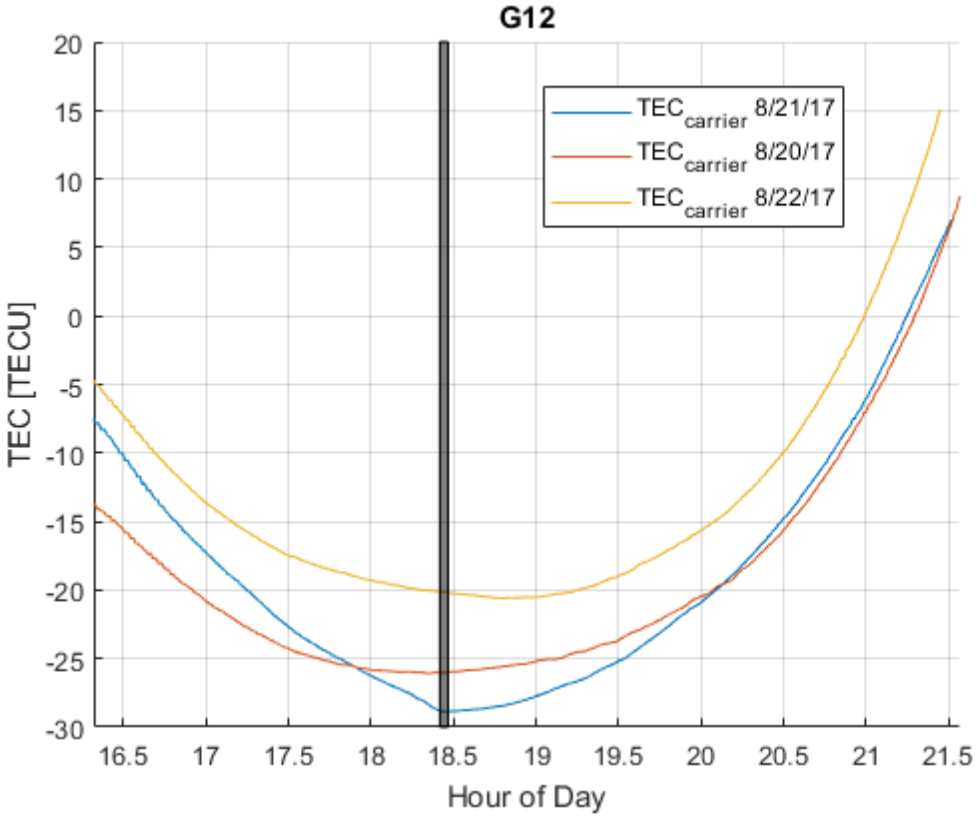

Figure 12: Raw slant TEC measurement histories over three days.

The vertical bar in Fig. 12 represents the times of day (a total of roughly 2.5 minutes) that the CORS station was totally eclipsed. Compared to the day-before and the day-after data, the data from the day of the eclipse (blue curve) dips by a significant amount more than the day-before and day-after data during the run-up to eclipse totality. The day-before measurements (red curve) begin at -14 TECU, dip by 12 TECU, and rise by 34 TECU. The day-after measurements (yellow curve) begin at -5 TECU, dip by 16 TECU, and rise by 36 TECU. The eclipse measurements (blue curve) begin at -7 TECU, dip by 22 TECU, and rise by 36 TECU. Additionally, the curve of the eclipse-day time history is not as smooth as the days before and after at the time of day of total

eclipse. Furthermore, the minimum slant TEC measurement of 8/21/17 is collected during the total eclipse, not slightly before (as in the day-before red curve) nor significantly after (as in the day-after yellow curve).

4.3 Analysis of the Beginning Segment of the Eclipse

This section covers the first segment of the eclipse. Figures 14 - 17 plot maps of the estimated Chapman profile peak electron density altitude h_{nemax} at 4 successive times early in the eclipse. Figures 18 - 21 plot maps of the Chapman profile altitude scale height h_{sc} at the same set of times. Figures 22 -25 plot maps of the Chapman profile Vertical TEC at the same set of times. The first of each of these sets of 4 plots corresponds to 15:47 UTC, which is the epoch at which the partial eclipse begins over the Pacific Ocean. The slant TEC fit errors of the estimate at 15:47 UTC have mean/standard-deviation/peak of values of -0.01/3.91/25.81 TECU. The second plot in each set of 4 corresponds to 16:15 UTC, which is still before any portion of the Earth is totally eclipsed. It is included to show how the ionosphere progresses during the partially eclipsed phase. The slant TEC fit errors of the estimate at 16:15 UTC have mean/standard-deviation/peak values of -0.01/3.82/19.58 TECU. The third plot in each set of 4 corresponds to 16:48 UTC, which is the instant that the total eclipse began. The slant TEC fit errors of the estimate at 16:48 UTC have mean/standard-deviation/peak values of -0.01/3.64/23.10 TECU. The fourth plot in each set of 4 corresponds to 17:15 UTC when the Pacific Ocean near Oregon is totally eclipsed. The slant TEC fit errors of the estimate at 17:15 UTC have mean/standard-deviation/peak values of -0.02/3.63/28.92 TECU.

The dataset used to produce the plots at 15:47 UTC contained 12463 slant TEC measurements from 1248 CORS receivers and 11 radio occultation passes. The dataset used to produce the plots at 16:15 UTC contained 11727 slant TEC measurements from 1258 CORS receivers and 14 radio occultation passes. The dataset used to produce the plots at 16:48 UTC contained 12345 slant

TEC measurements from 1429 CORS receivers and 9 radio occultation passes. The dataset used to produce the plots at 17:15 UTC contained 11462 slant TEC measurements from 1349 CORS receivers and 7 radio occultation passes. Figure 13 shows the ionosphere pierce points of the lines-of-sight between CORS receivers and GPS satellites, as in Section 3.2. These points are shown as dark grey dots in Fig. 13. They apply for the dataset corresponding to 15:47 UTC. The figure also shows the lowest points of approach of the lines-of-sight between orbiting radio-occultation receivers and GPS satellites, which are analogous to the purple dot in Fig. 6. Again, these apply to the dataset corresponding to 15:47 UTC. These points are shown as white diamonds. Note that a single radio occultation pass corresponds to a period spanning from 30 seconds before to 30 seconds after the corresponding epoch. This provides a larger "sweep" of the ionosphere. A sweep includes 30-60 measurements per pass instead of a single measurement.

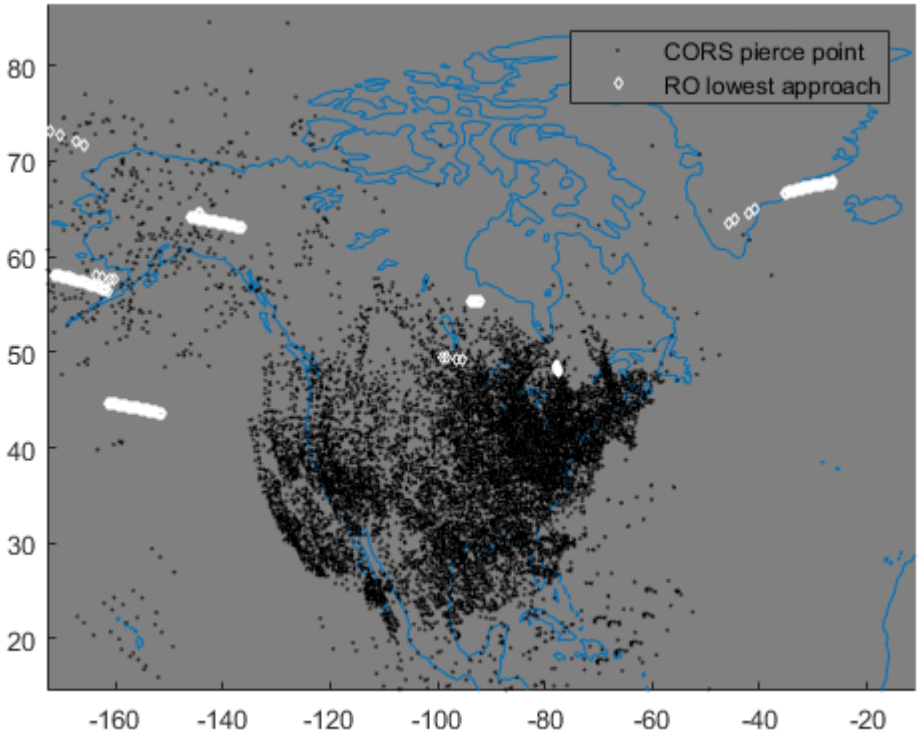

Figure 13: CORS to GPS satellite line-of-sight 350 km altitude ionosphere pierce points and points of lowest approach to the Earth of orbiting radio-occultation receiver to GPS satellite lines-of-sight. Data correspond to 15:47 UTC.

Figures 14 - 17 illustrate how the altitude of peak electron density map changes over time. At the instant that the partial Eclipse begins, h_{nemax} does not differ very much from the *a priori* or two-day mean map of h_{nemax}. Note that the expression "two-day mean" used here and throughout this thesis indicates the mean of the day-before and the day-after estimates of the given Chapman parameter as computed at the identical UTC during the prior and following days. At most, the optimal map of h_{nemax} differs by about 5 km from the *a priori* map. However, as the eclipse enters totality in Fig. 16, a portion of the ionosphere near the northwest contiguous United States begins to experience an increase in h_{nemax}. Even though that part of the Earth has not experienced totality yet, it has been in some degree of partial eclipse conditions that could

have caused the large peak. As this peak is happening, there is a portion of the southeastern United States that is experiencing a gradual decrease in h_{nemax}, ultimately by 15-17 km in Fig. 17, according to the *a priori* map. However, the two-day mean maps do not follow the same trend and, therefore, the effect that the eclipse has on h_{nemax} during this timeframe is inconclusive.

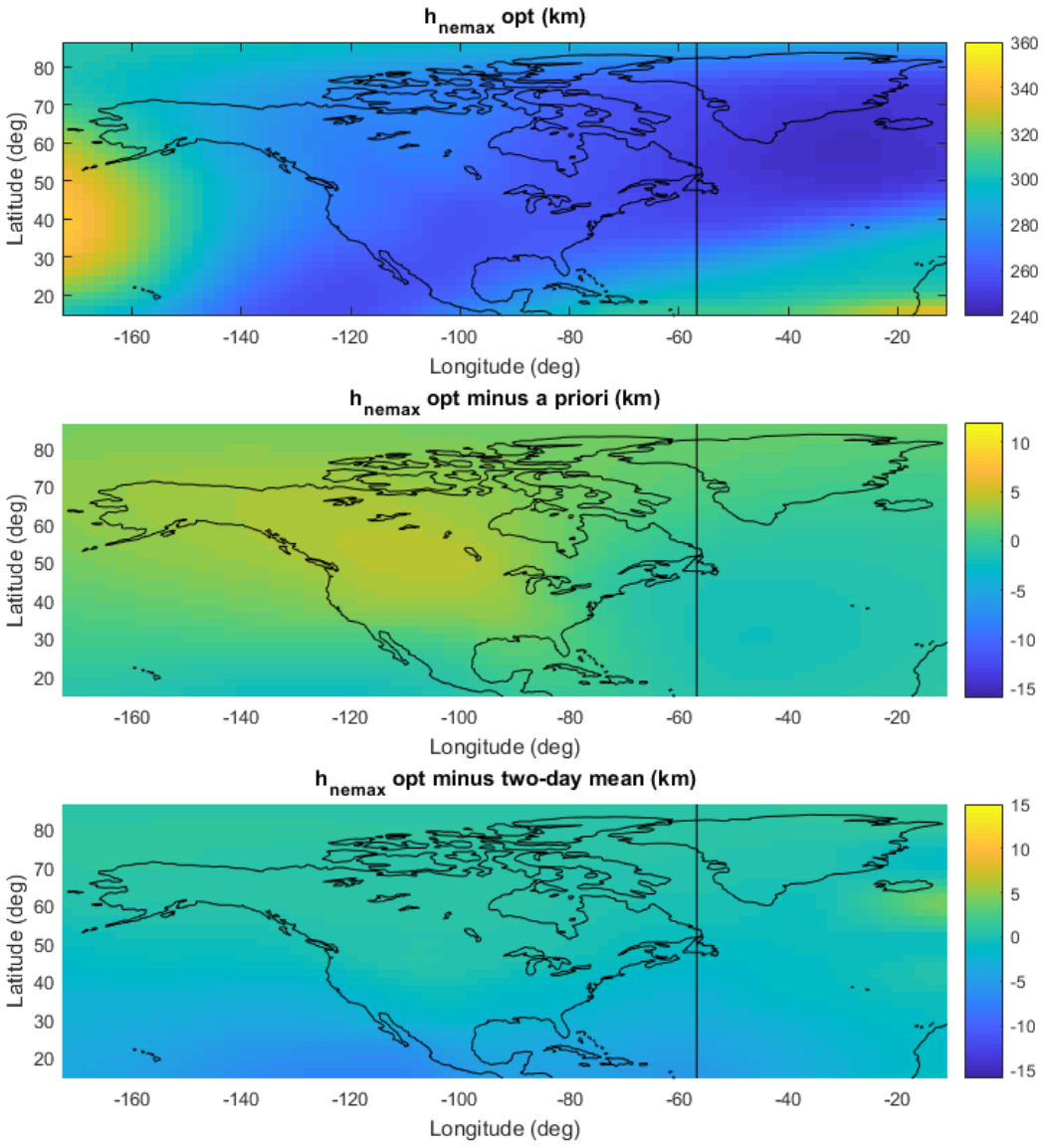

Figure 14: Optimal, deviation from *a priori,* and deviation from two-day mean maps of h_{nemax} at 15:47 UTC. Local noon at 57° W.

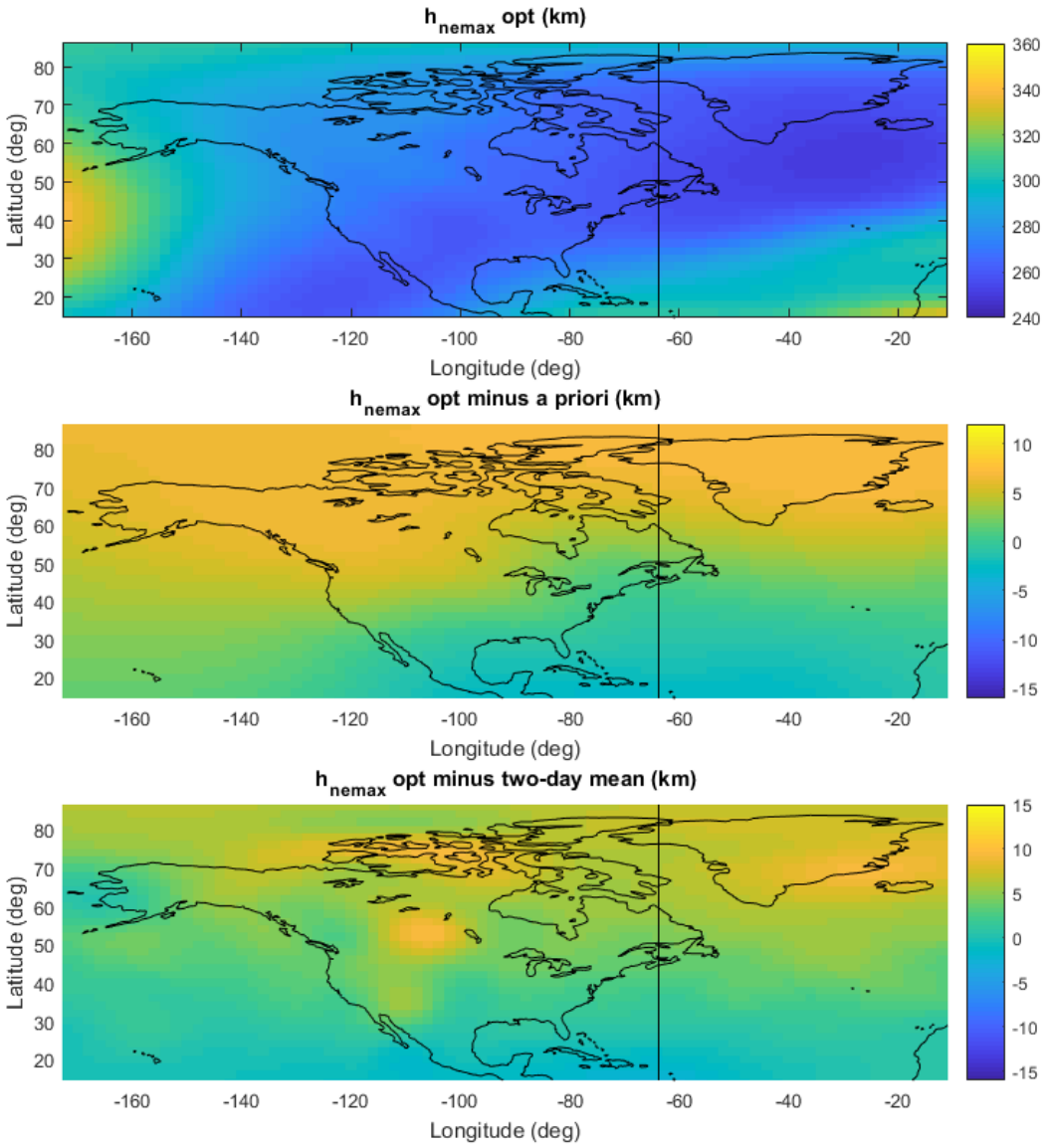

Figure 15: Optimal, deviation from *a priori,* and deviation from two-day mean maps of h_{nemax} at 16:15 UTC. Local noon at 64° W.

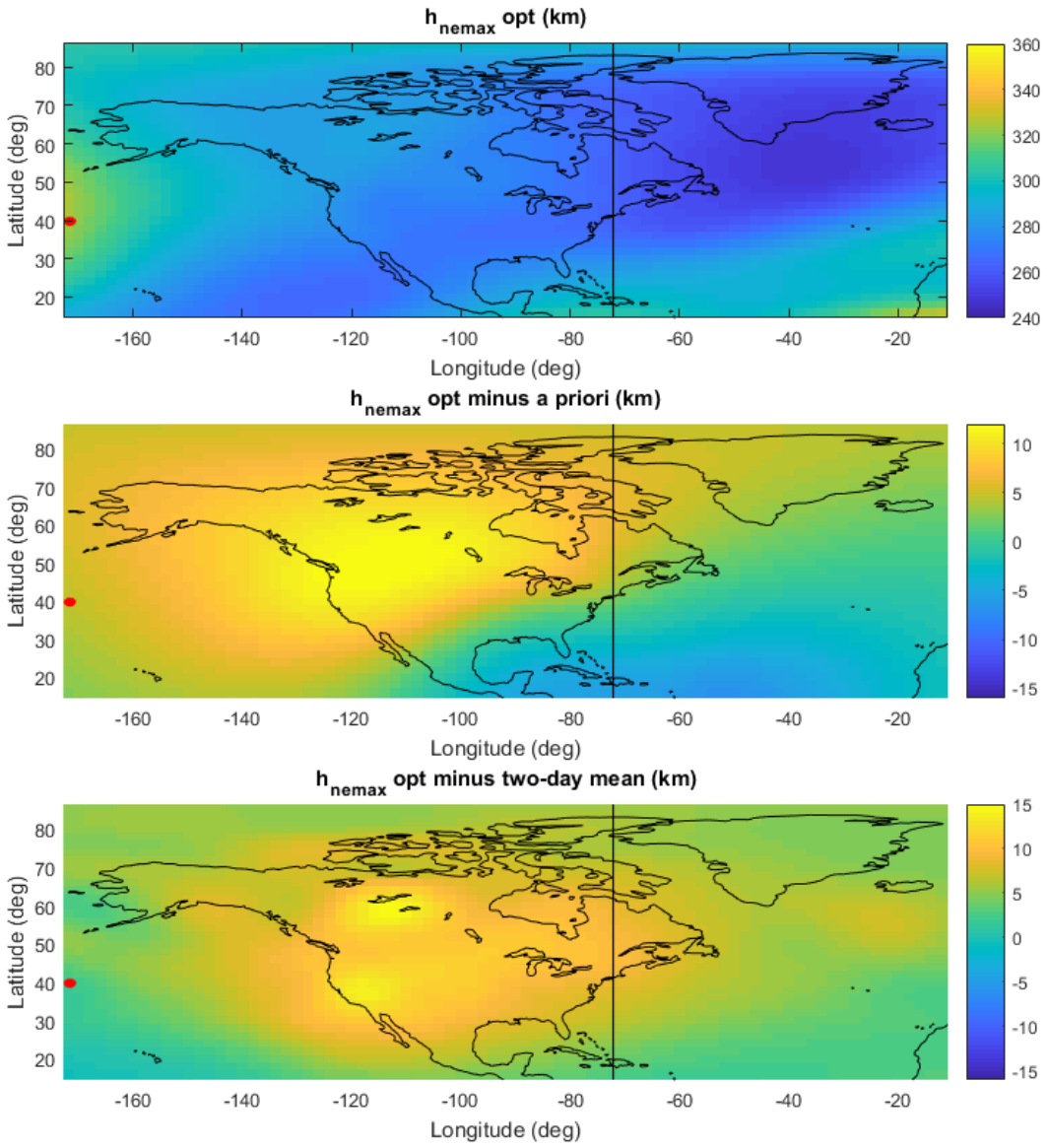

Figure 16: Optimal, deviation from *a priori,* and deviation from two-day mean maps of h_{nemax} at 16:48 UTC. Local noon at 72° W.

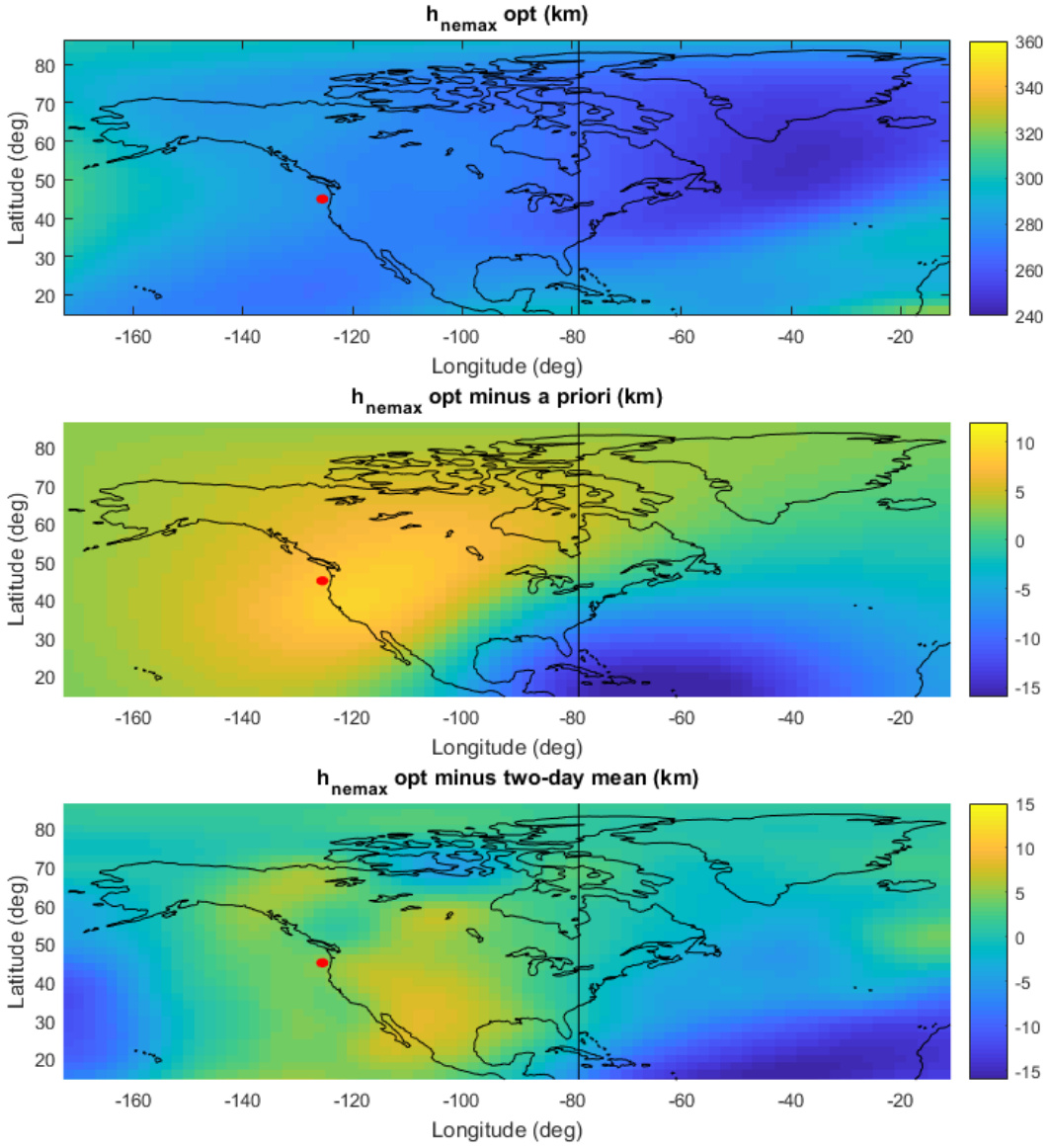

Figure 17: Optimal, deviation from *a priori,* and deviation from two-day mean maps of h_{nemax} at 17:15 UTC. Local noon at 79° W.

As the region of totality closes in on the United States, Figs. 18 -21 demonstrate that the scale height does not differ very much from the *a priori* or the two-day mean map.

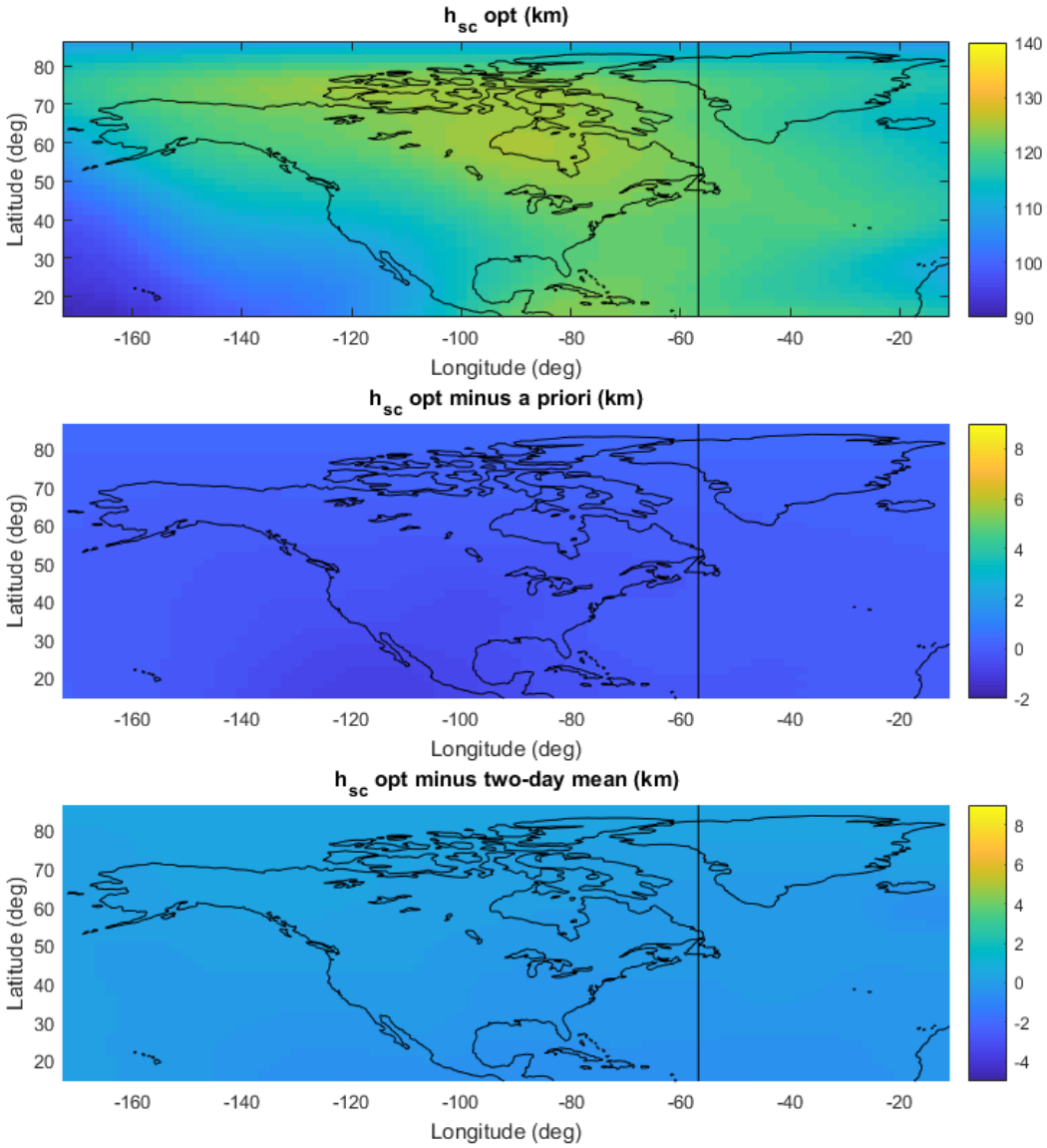

Figure 18: Optimal, deviation from *a priori,* and deviation from two-day mean maps of h_{sc} at 15:47 UTC. Local noon at 57° W.

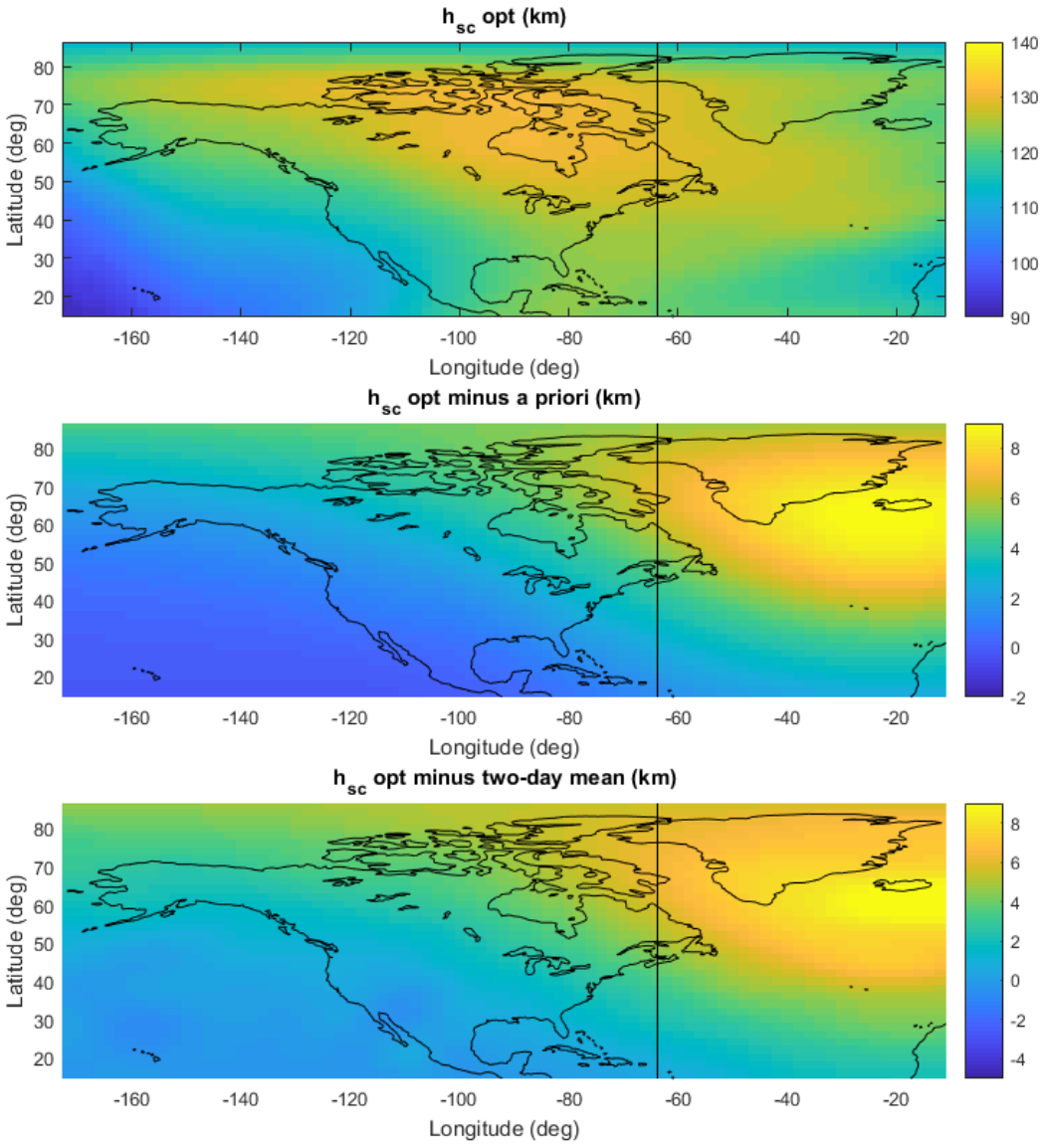

Figure 19: Optimal, deviation from *a priori,* and deviation from two-day mean maps of h_{sc} at 16:15 UTC. Local noon at 64° W.

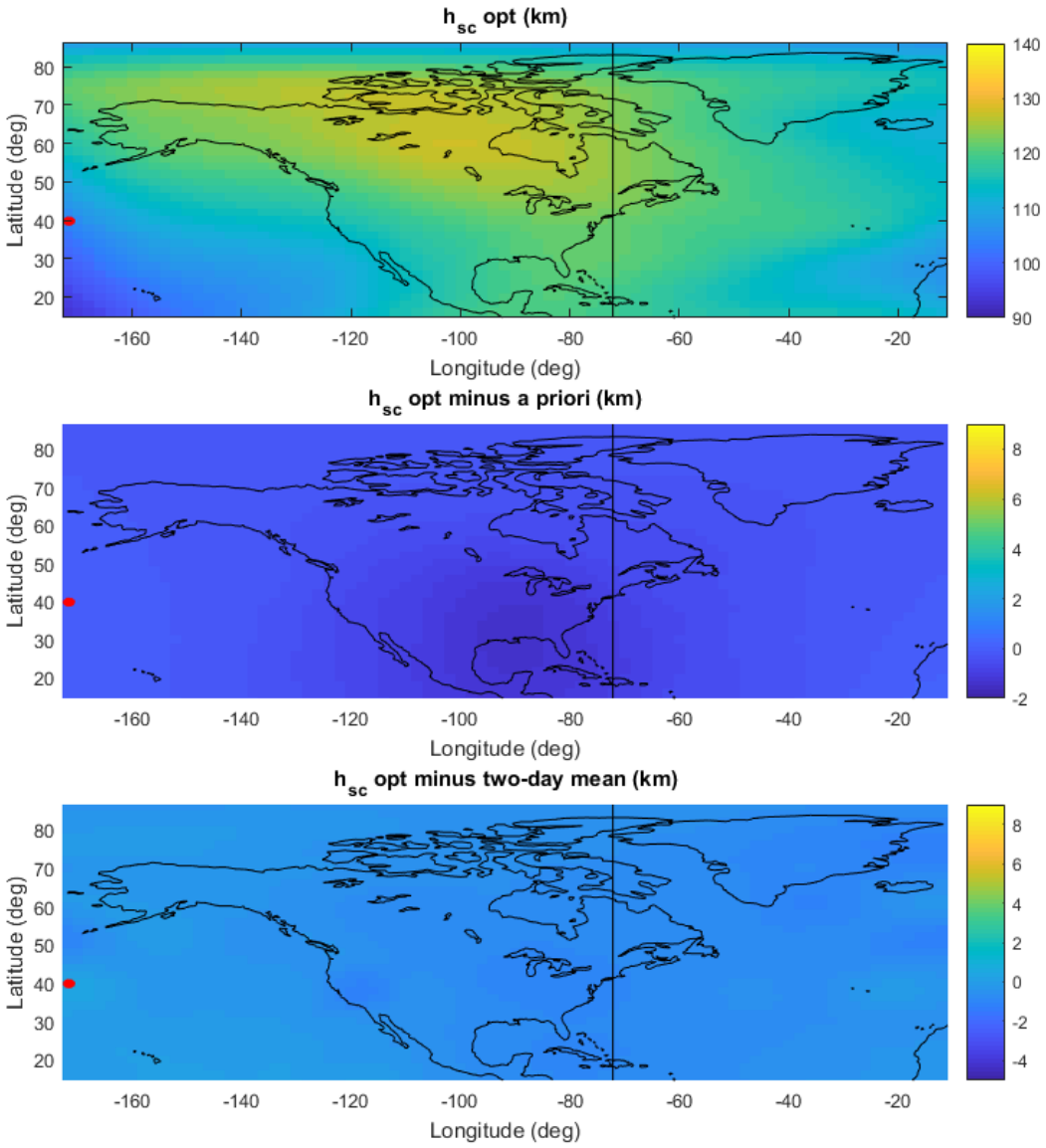

Figure 20: Optimal, deviation from *a priori,* and deviation from two-day mean maps of h_{sc} at 16:48 UTC. Local noon at 72° W.

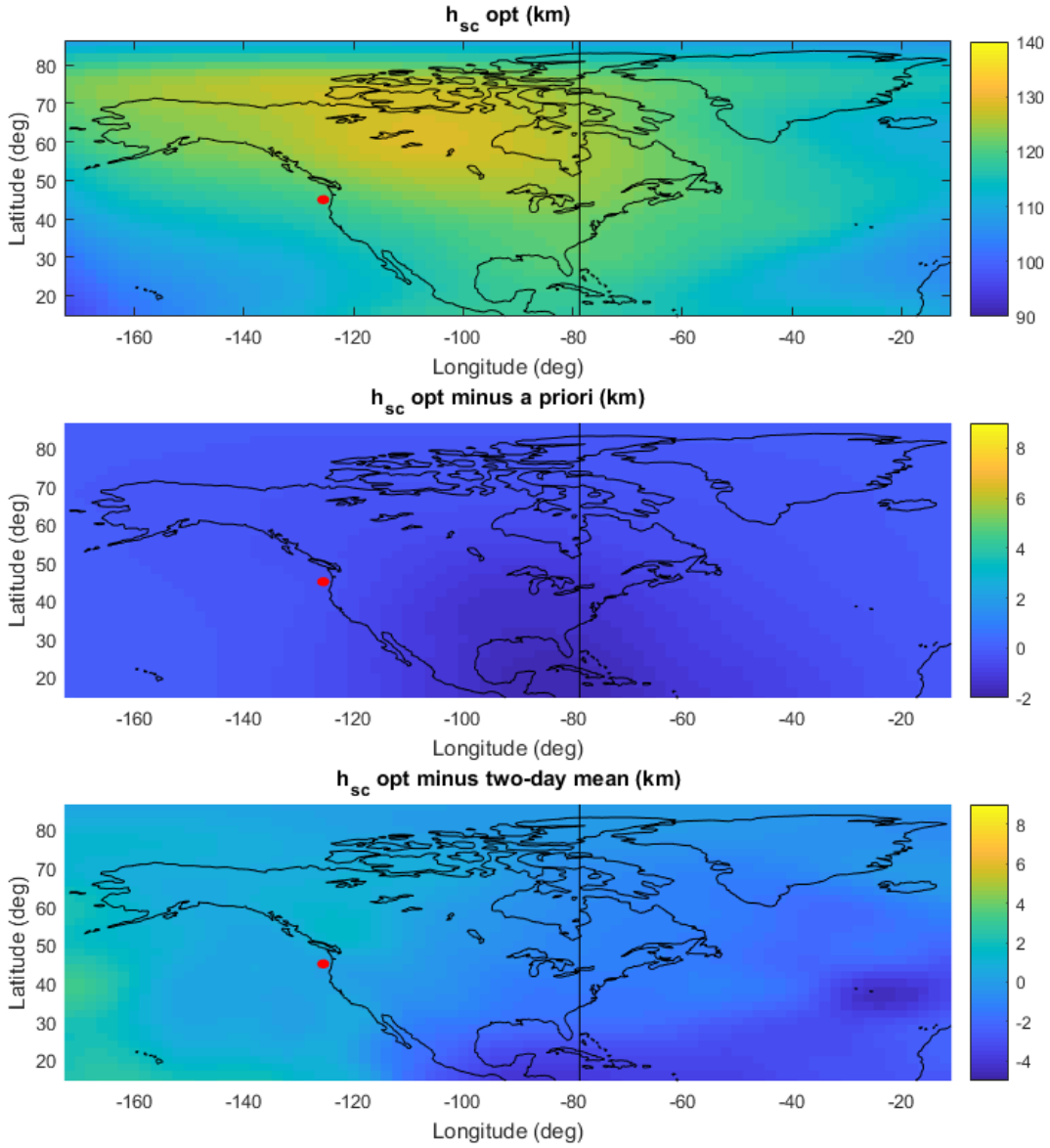

Figure 21: Optimal, deviation from *a priori,* and deviation from two-day mean maps of h_{sc} at 17:15UTC. Local noon at 79° W.

Figures 22-25 show the estimated VTEC map (top plots) and its deviations from the *a priori* (middle plots) and from the two-day average (bottom plots) at four times early in the eclipse sequence. Beginning in Figs. 24 and 25, a pocket of the ionosphere surrounding the region of totality experiences a significant dip in VTEC of 5-7 TECU if one compares the difference between the estimated and two-day mean VTEC in this north-west region among the 4 plots. Not only does the region directly within totality at 17:15 UTC experience a large dip in VTEC, but the region immediately west of totality that had recently experienced the total eclipse still has lower VTEC values. So, that region immediately west has yet to recover the dip in VTEC at 17:15 UTC causing a small “wake” behind the region of totality.

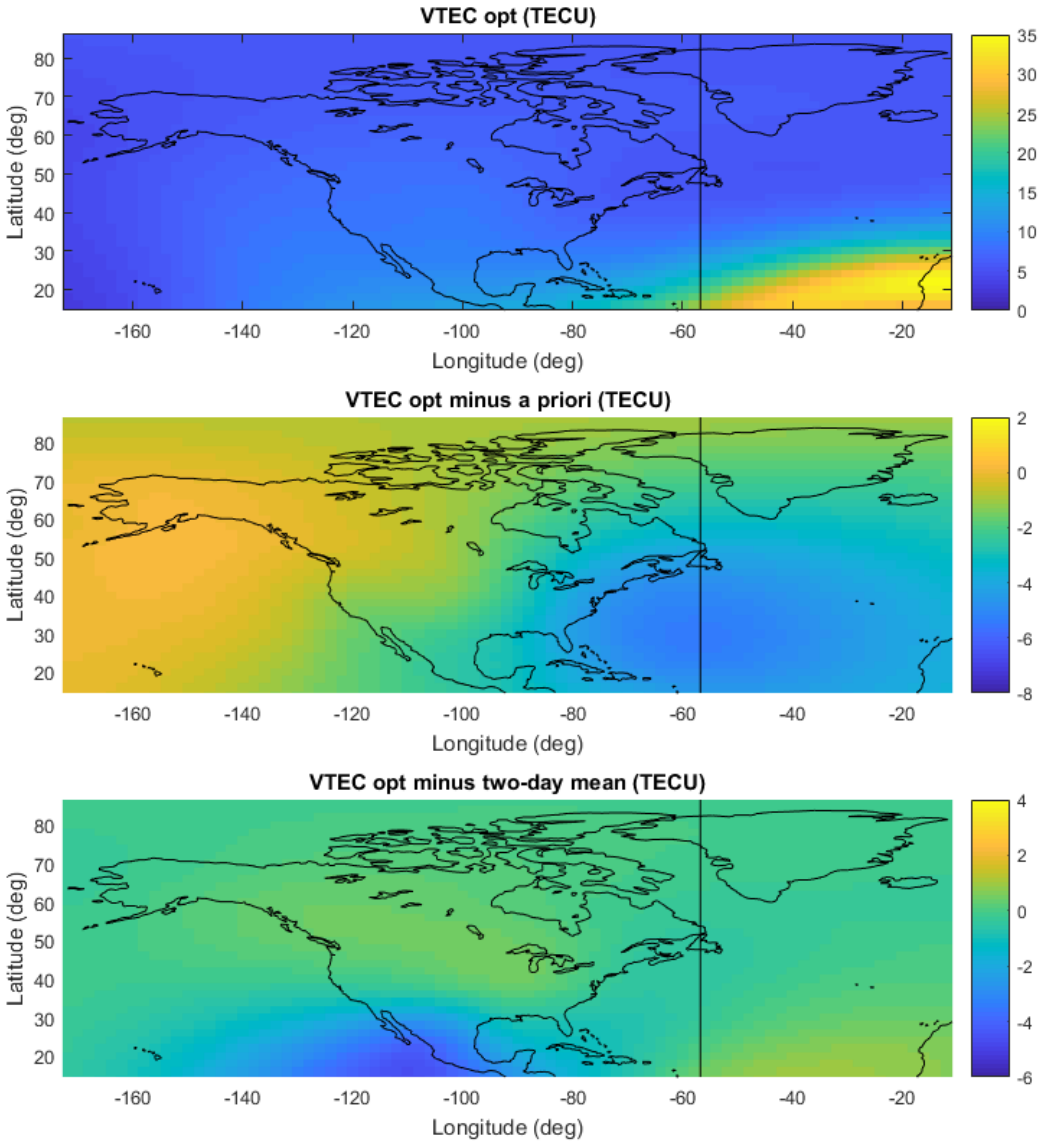

Figure 22: Optimal, deviation from *a priori,* and deviation from two-day mean maps of VTEC at 15:47 UTC. Local noon at 57° W.

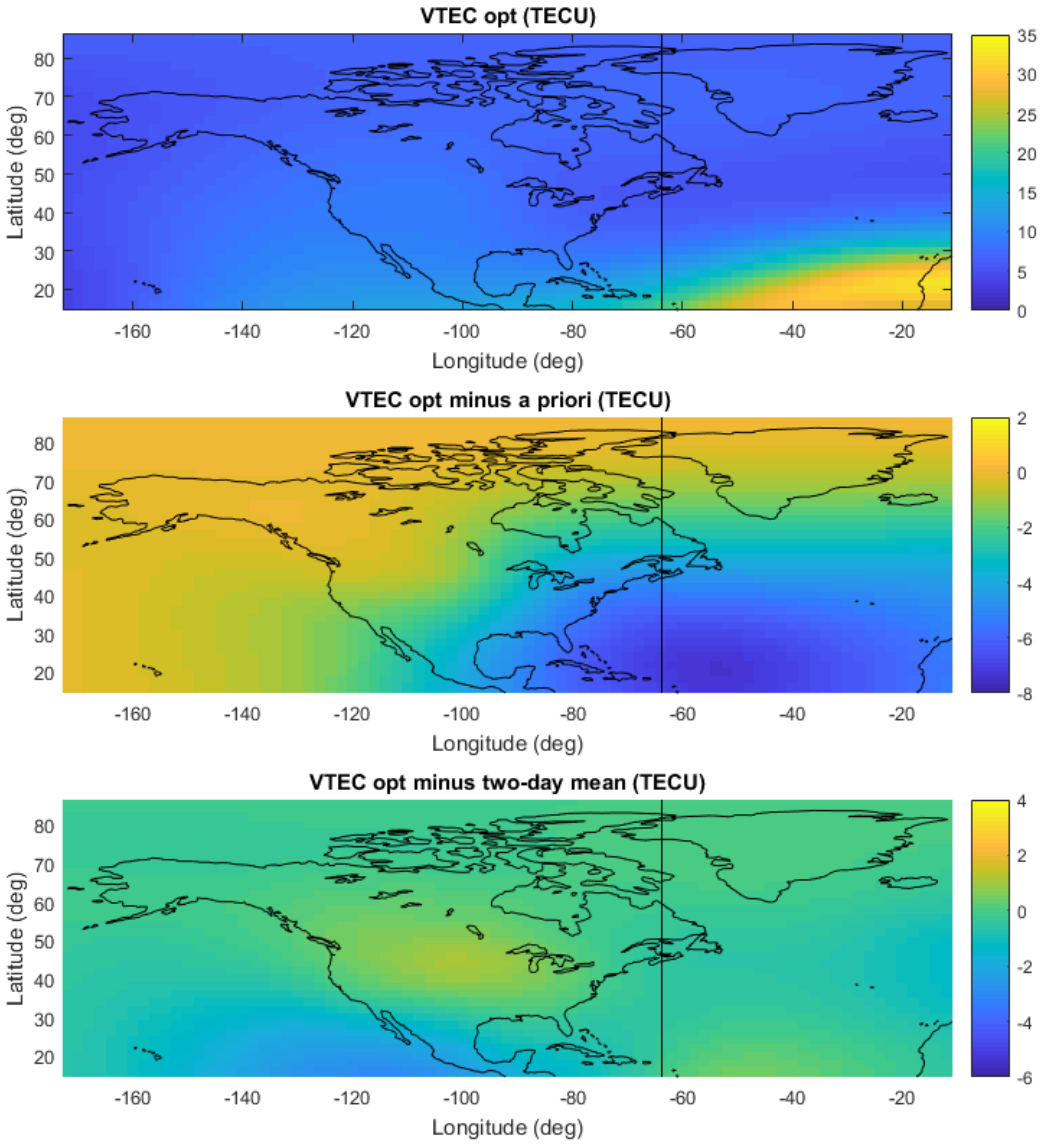

Figure 23: Optimal, deviation from *a priori,* and deviation from two-day mean maps of VTEC at 16:15 UTC. Local noon at 64° W.

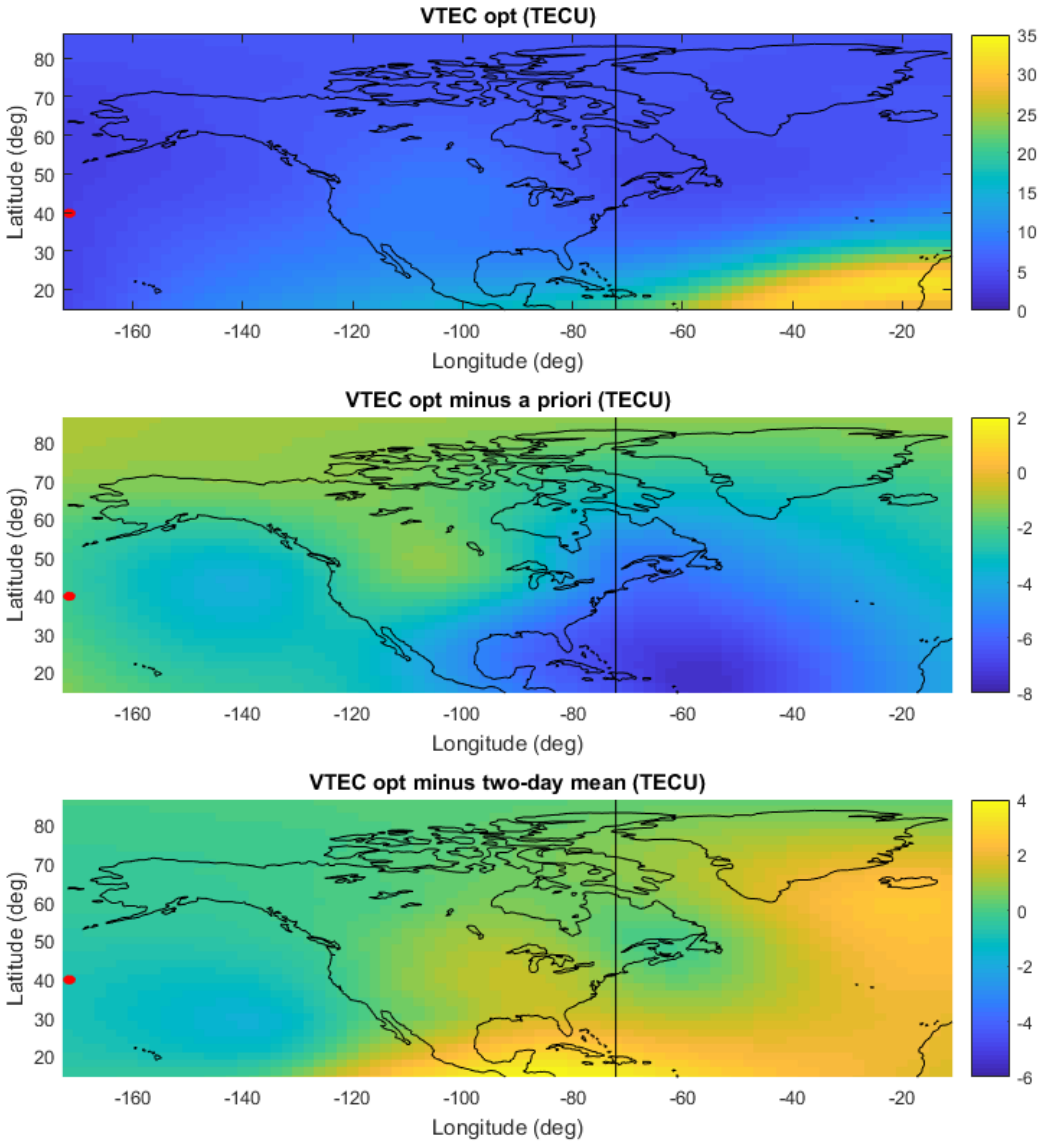

Figure 24: Optimal, deviation from *a priori,* and deviation from two-day mean maps of VTEC at 16:48 UTC. Local noon at 72° W.

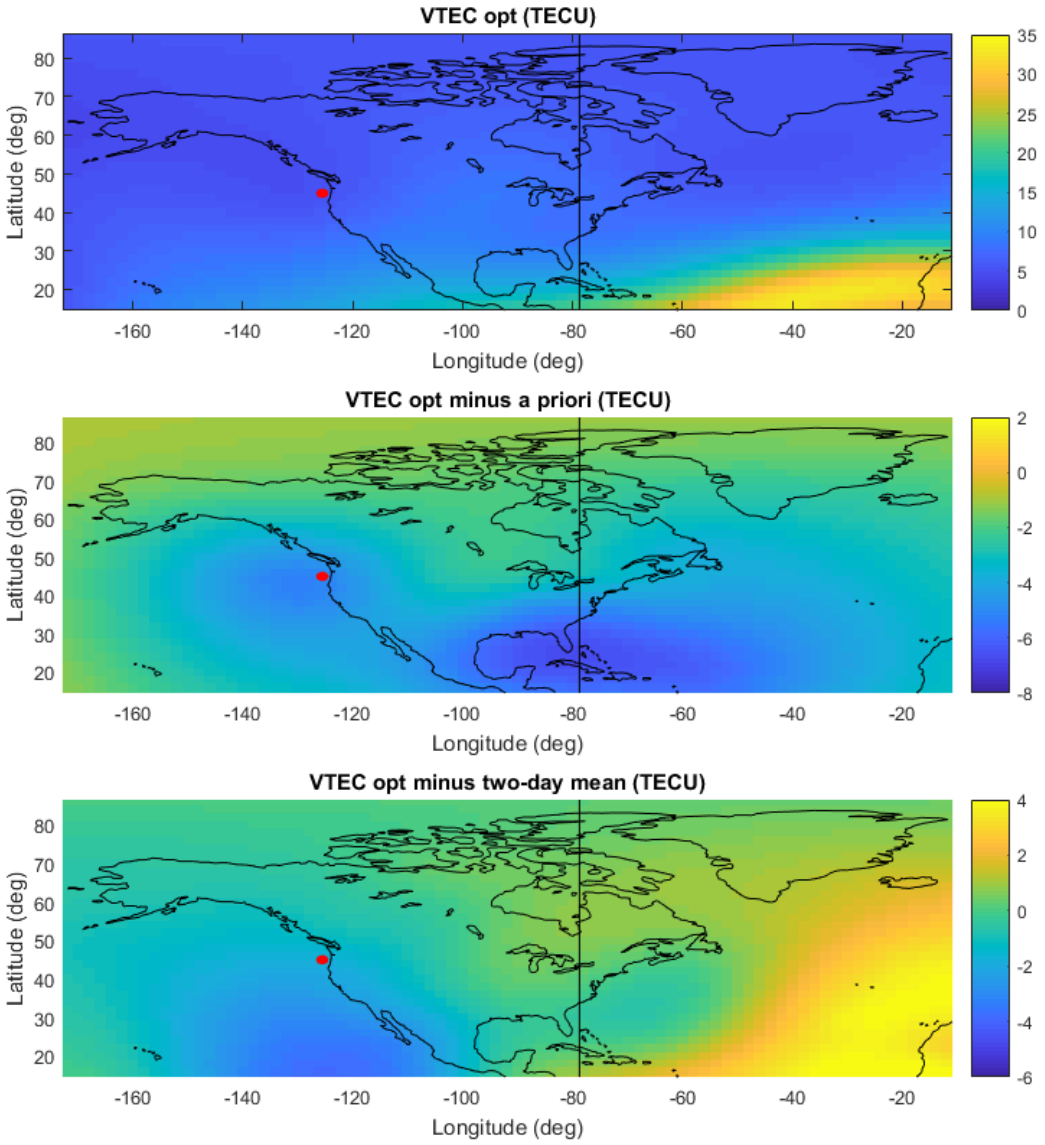

Figure 25: Optimal, deviation from *a priori,* and deviation from two-day mean maps of VTEC at 17:15 UTC. Local noon at 79° W.

4.4 Analysis of the Intermediate Segment of the Eclipse

This subsection analyzes the intermediate portion of the eclipse. Figures 27 - 30 plot maps of the estimated Chapman profile peak electron density altitude h_{nemax} at 4 successive times in the middle of the eclipse. Figures 31 - 34 plot maps of the Chapman profile altitude scale height h_{sc} at the same set of times. Figures 35 - 38 plot maps of the Chapman profile Vertical TEC at the same set of times. The first of each of these sets of 4 plots corresponds to 17:45 UTC when the region of totality is over Wyoming. The slant TEC fit errors of the estimate at 17:45 UTC have mean/standard-deviation/peak values of -0.02/3.64/28.57 TECU. The second plot in each set of 4 corresponds to 18:15 UTC when the region of totality is over southeastern Missouri. The slant TEC fit errors of the estimate at 18:15 UTC have mean/standard-deviation/peak values of 0.02/3.43/27.78 TECU. The third plot in each set of 4 corresponds to the maximum eclipse when the maximum width of the band is 115 km and the region of totality is over southwestern Kentucky at 18:26 UTC. The slant TEC fit errors of the estimate at 18:26 UTC have mean/standard-deviation/peak values of -0.02/3.55/24.96 TECU. The fourth plot in each set of 4 corresponds to when the eclipse is over South Carolina. The slant TEC fit errors of the estimate at 18:45 UTC have mean/standard-deviation/peak values of 0.02/3.79/31.63 TECU. This section shows how the ionosphere changes as the eclipse passes over the United States. The results in this section will perhaps be the most revealing because most of the TEC measurements were made in this region. Additionally, the region of totality passes through local noon in this section.

The dataset used to produce the plots at 17:45 UTC contained 11720 slant TEC measurements from 1282 CORS receivers and 17 radio occultation passes. The dataset used to produce the plots at 18:15 UTC contained 12764 slant TEC measurements from 1436 CORS receivers and 8 radio occultation passes. The dataset used to produce the plots at 18:26 UTC contained 12395 slant TEC measurements from 1406 CORS receivers and 5 radio occultation passes. The dataset used to produce the plots at 18:45 UTC contained 12241 slant TEC measurements from 1353 CORS

receivers and 4 radio occultation passes. Figure 26 shows the ionosphere pierce points of the lines-of-sight between CORS receivers and GPS satellites as dark grey points. It also shows the lowest points of approach of the lines-of-sight between orbiting radio-occultation receivers and GPS satellites as white diamonds. The points in this figure all apply for the dataset corresponding to 18:26 UTC.

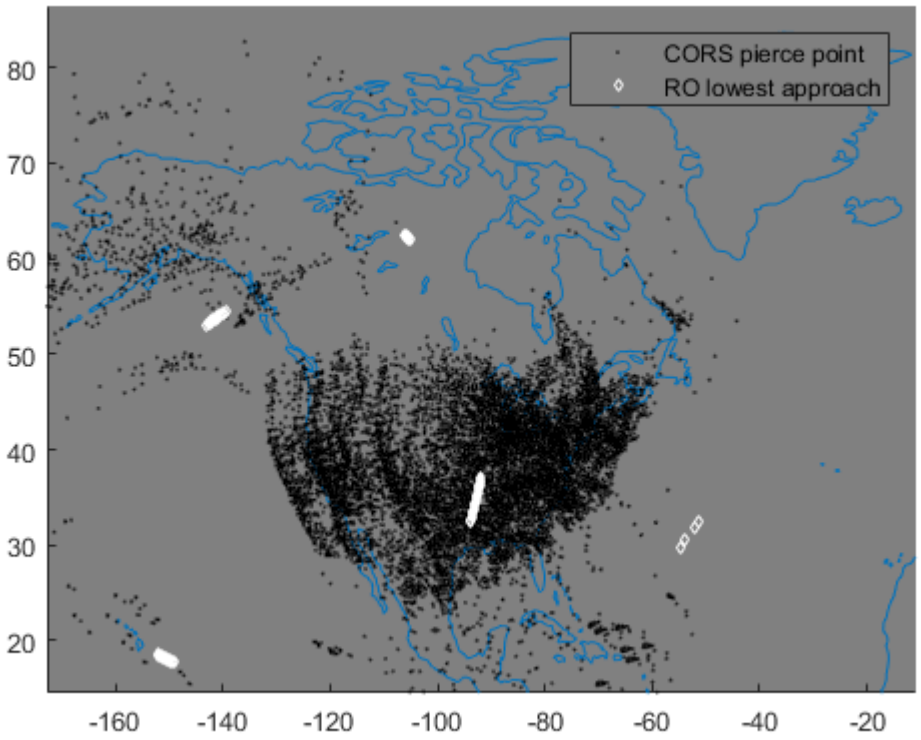

Figure 26: CORS to GPS satellite line-of-sight 350 km altitude ionosphere pierce points and points of lowest approach to the Earth of orbiting radio-occultation receiver to GPS satellite lines-of-sight. Data correspond to 18:26 UTC.

Figure 28 illustrates a clear peak in the h_{nemax} difference from the two-day mean. The peak is about 45 km above the two-day mean map. After the eclipse passes local noon, a noticeable wake is created in the eclipse path. The wake of the totality region is very large in radius and magnitude by the time associated with Fig. 30. In fact, the increase of h_{nemax} reaches 60 km above

the two-day average at the highest point of this wake region, as seen in Fig. 30 in regions where the eclipse has already passed through.

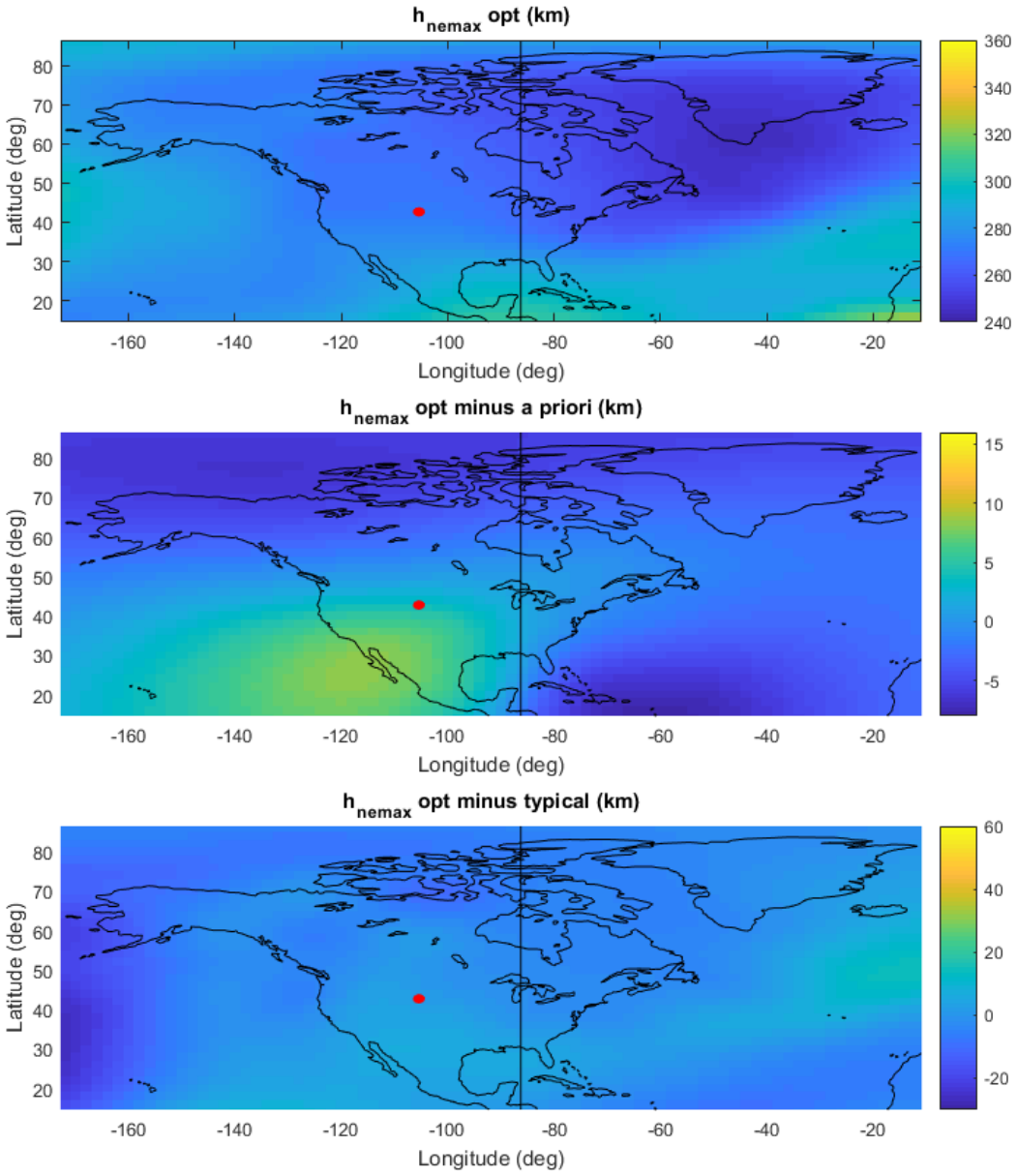

Figure 27: Optimal, deviation from *a priori,* and deviation from two-day mean maps of h_{nemax} at 17:45 UTC. Local noon at 86° W.

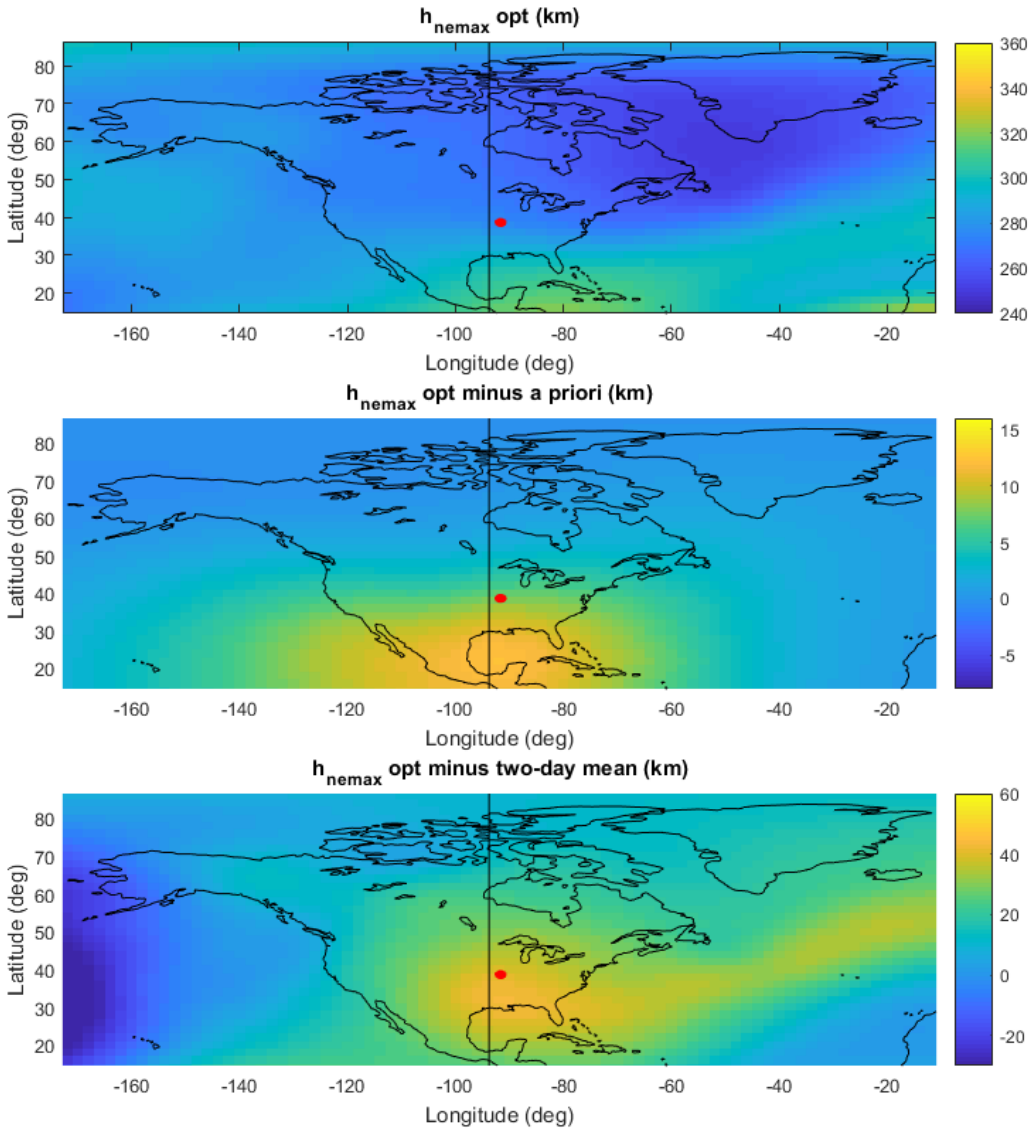

Figure 28: Optimal, deviation from *a priori,* and deviation from two-day mean maps of h_{nemax} at 18:15 UTC. Local noon at 94° W.

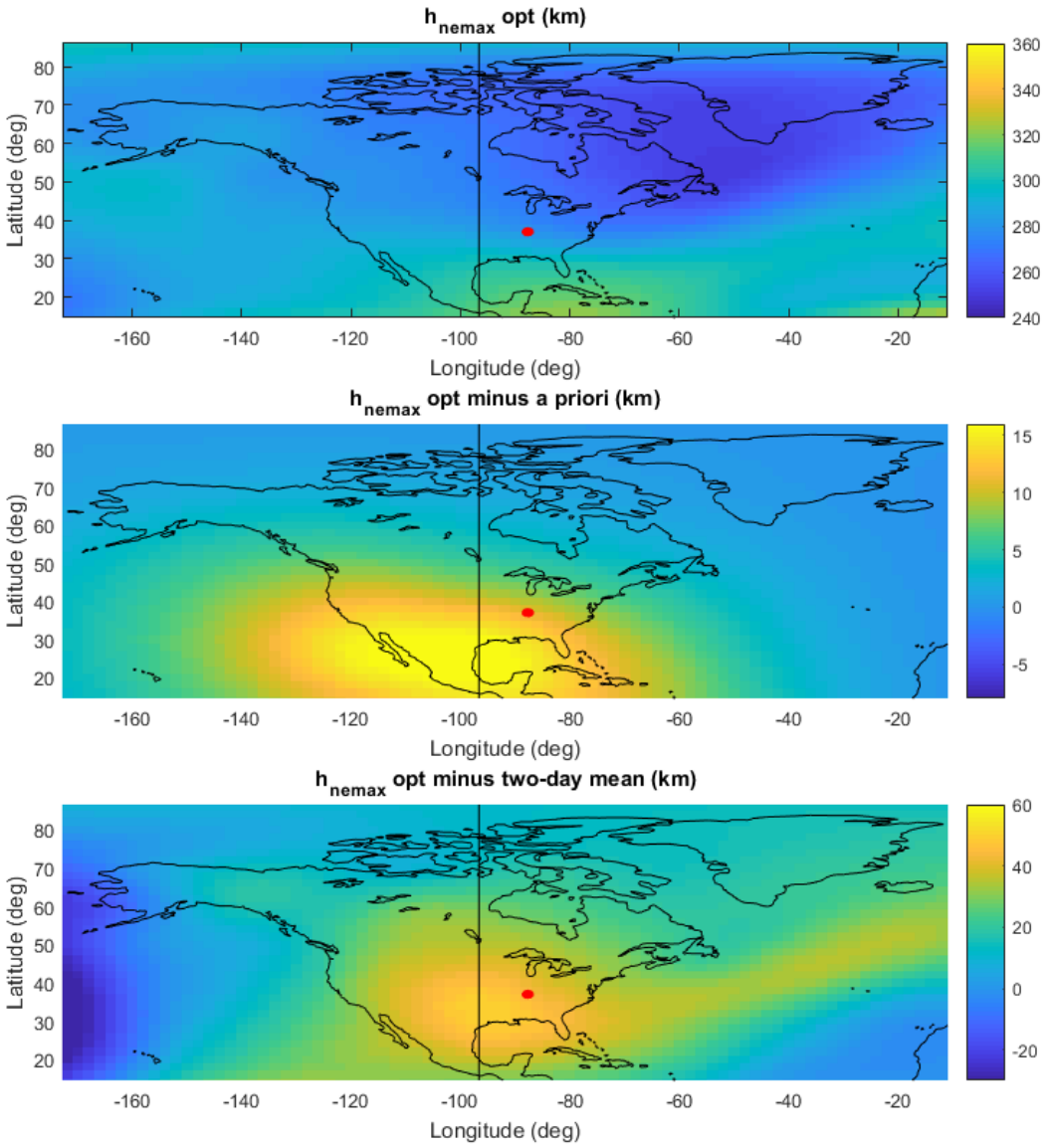

Figure 29: Optimal, deviation from *a priori,* and deviation from two-day mean maps of h_{nemax} at 18:26UTC. Local noon at 97° W.

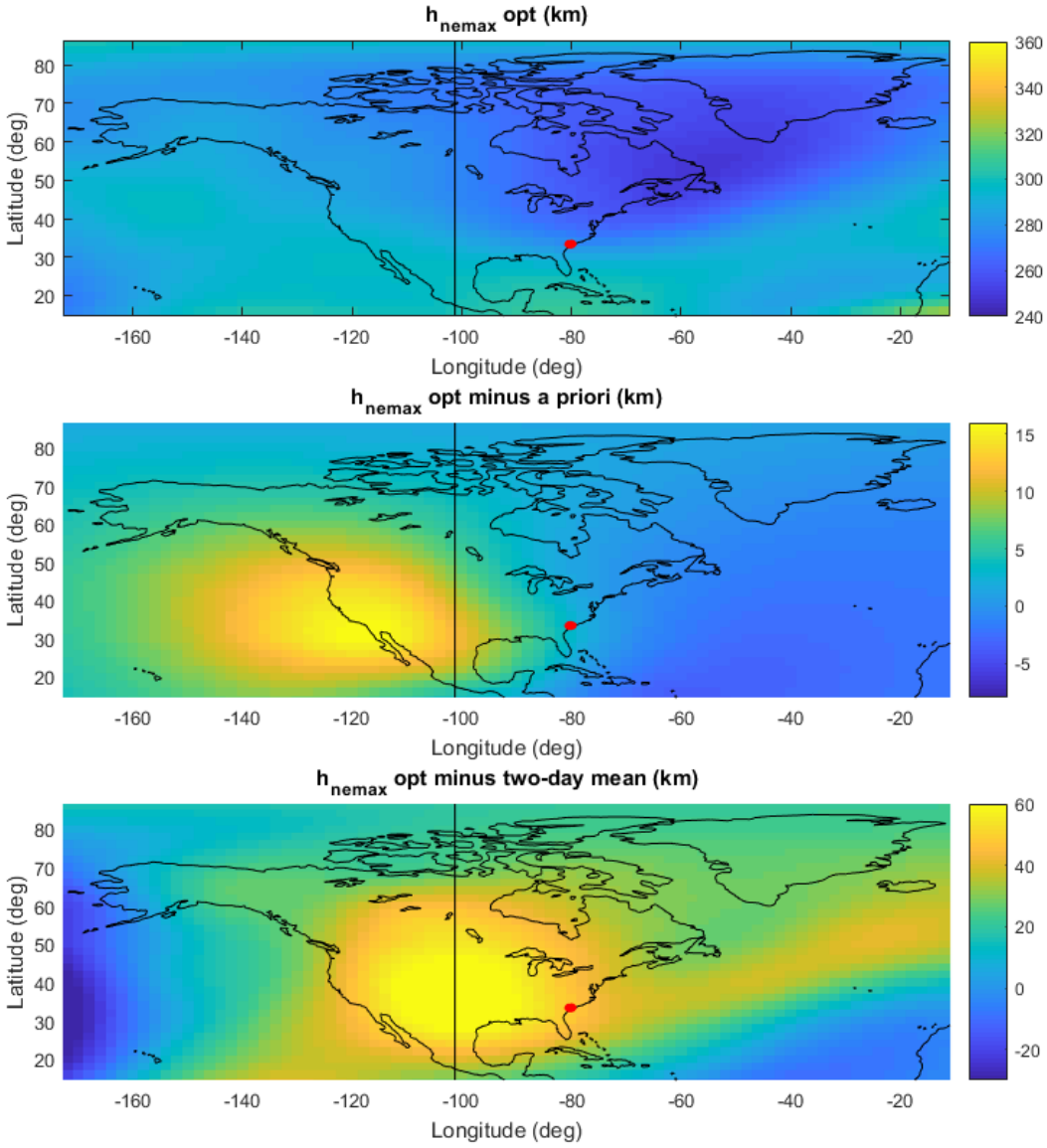

Figure 30: Optimal, deviation from *a priori,* and deviation from two-day mean maps of h_{nemax} at 18:45 UTC. Local noon at 101° W.

As noted in section 4.2, h_{sc} is not affected very much by the eclipse -- review Figs. 31 - 34. However, a slight increase in h_{sc} is observed near eclipsed regions.

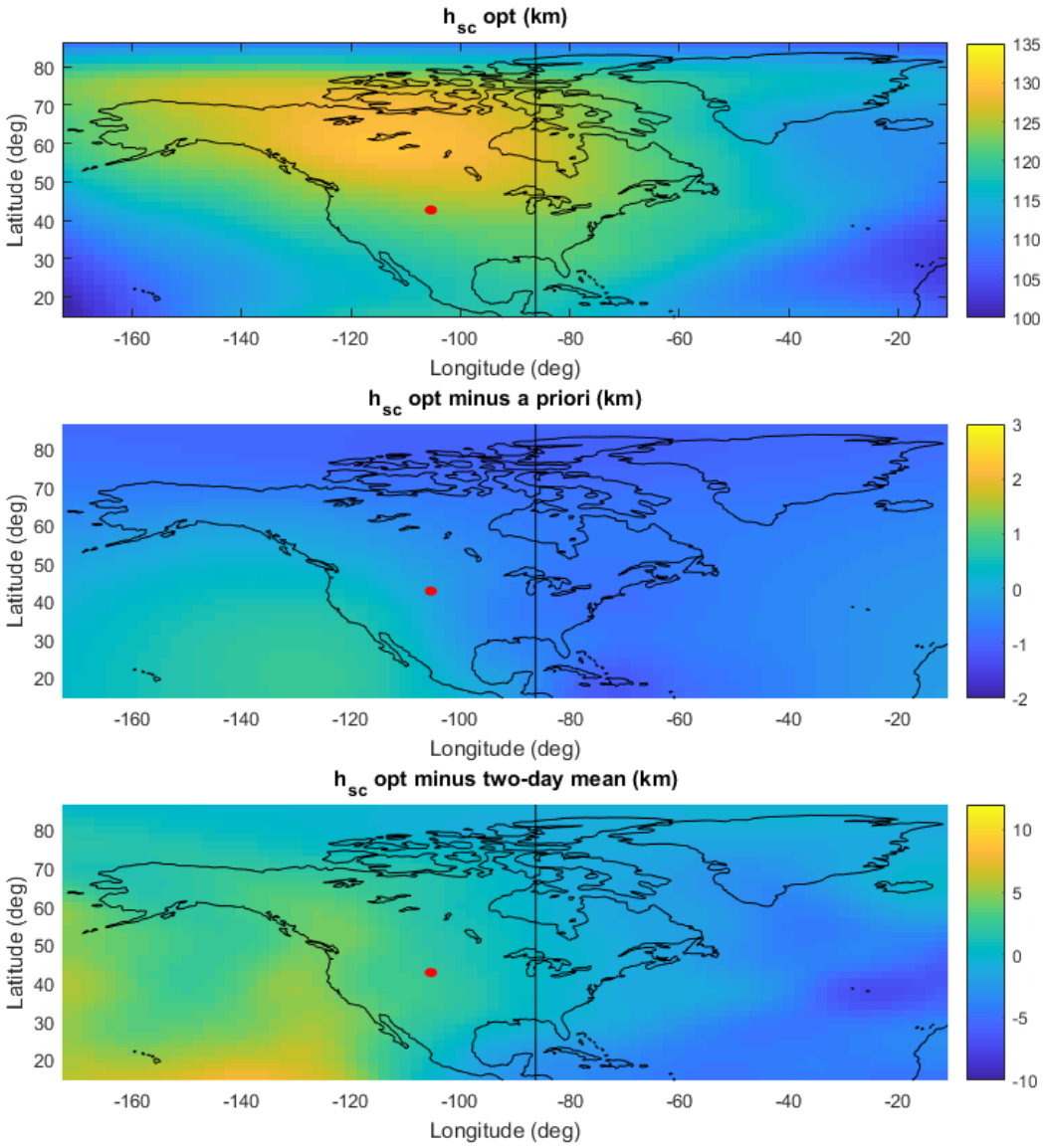

Figure 31: Optimal, deviation from *a priori,* and deviation from two-day mean maps of h_{sc} at 17:45 UTC. Local noon at 86° W.

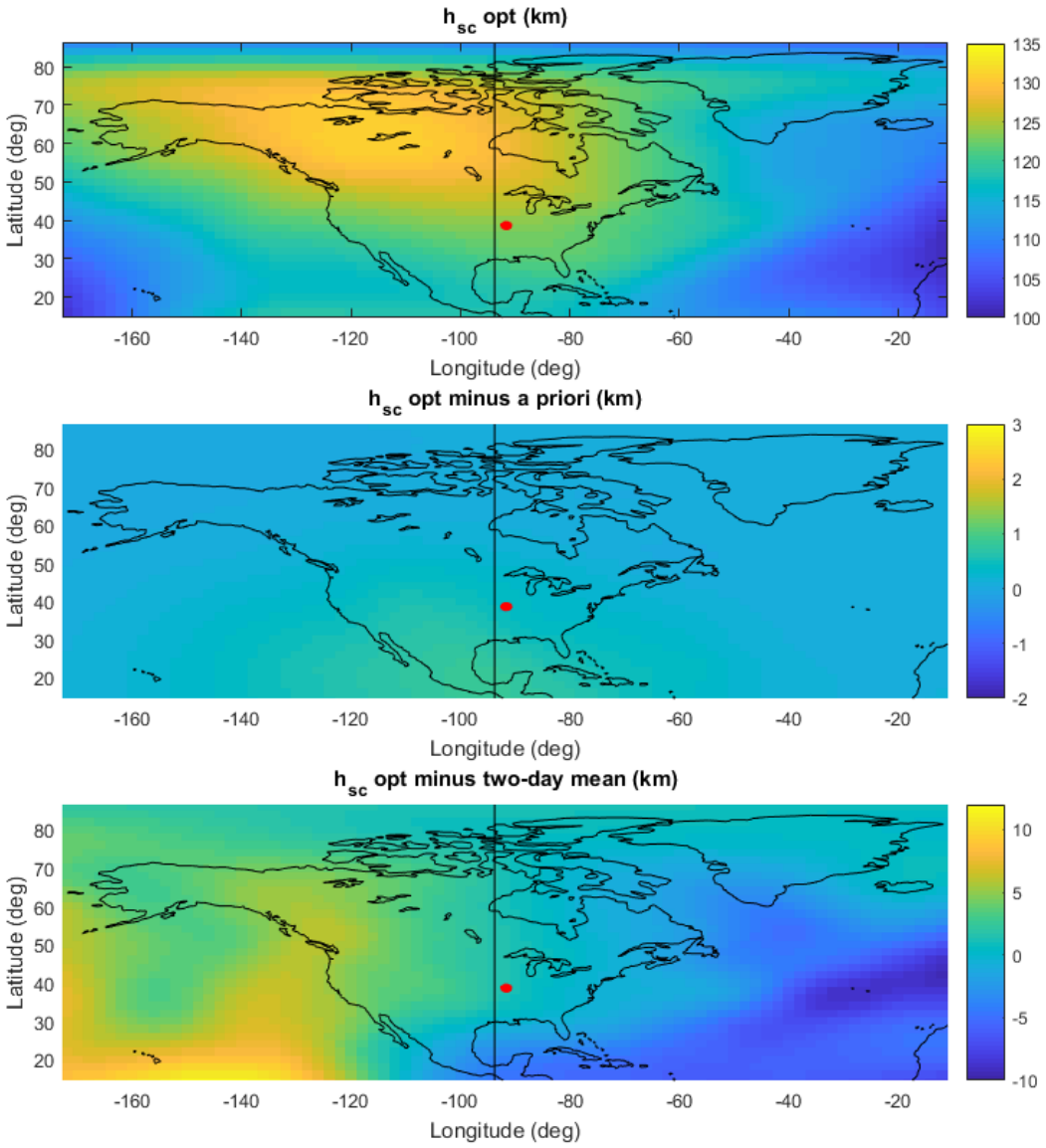

Figure 32: Optimal, deviation from *a priori,* and deviation from two-day mean maps of h_{sc} at 18:15 UTC. Local noon at 94° W.

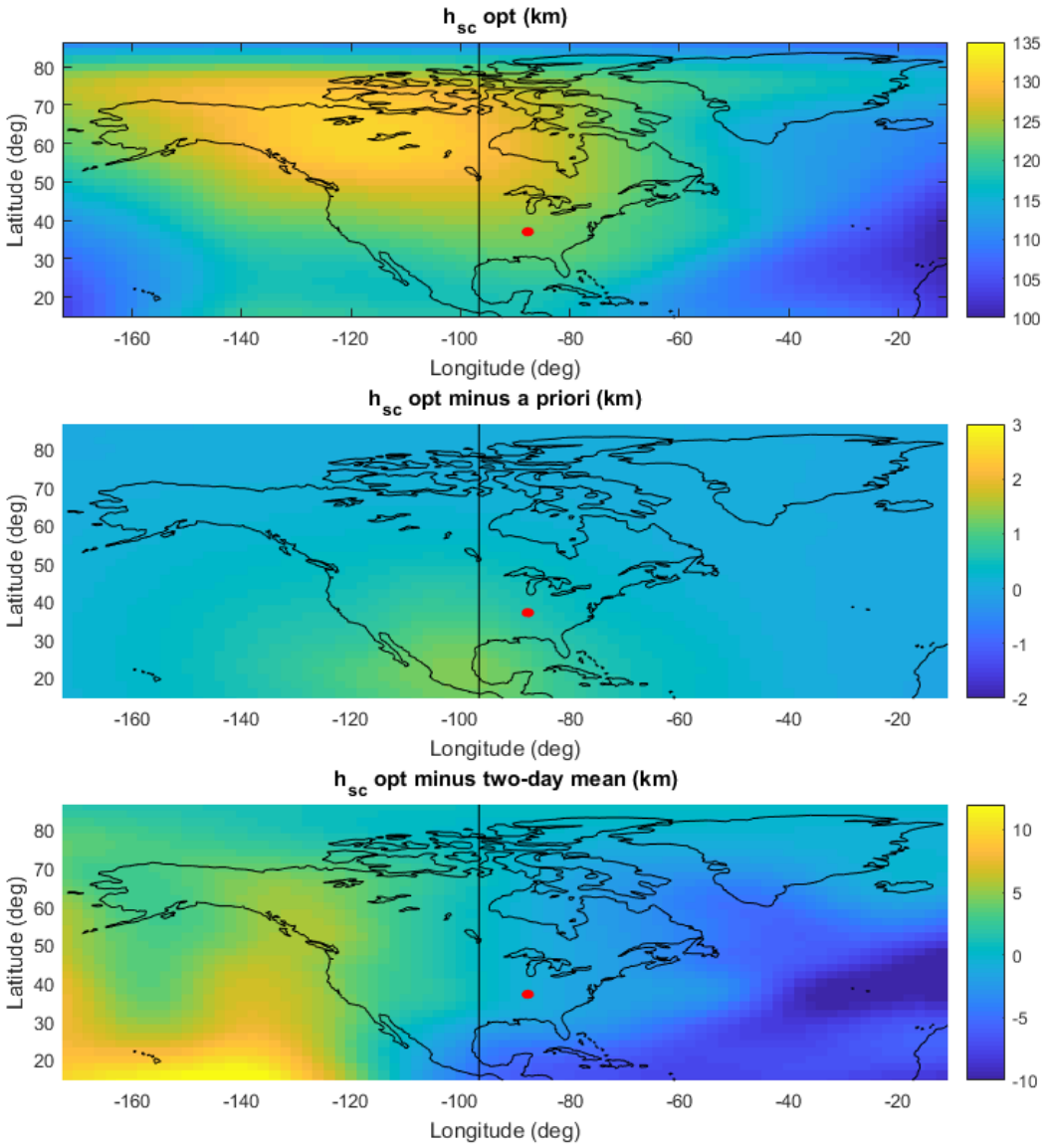

Figure 33: Optimal, deviation from *a priori,* and deviation from two-day mean maps of h_{sc} at 18:26 UTC. Local noon at 97° W.

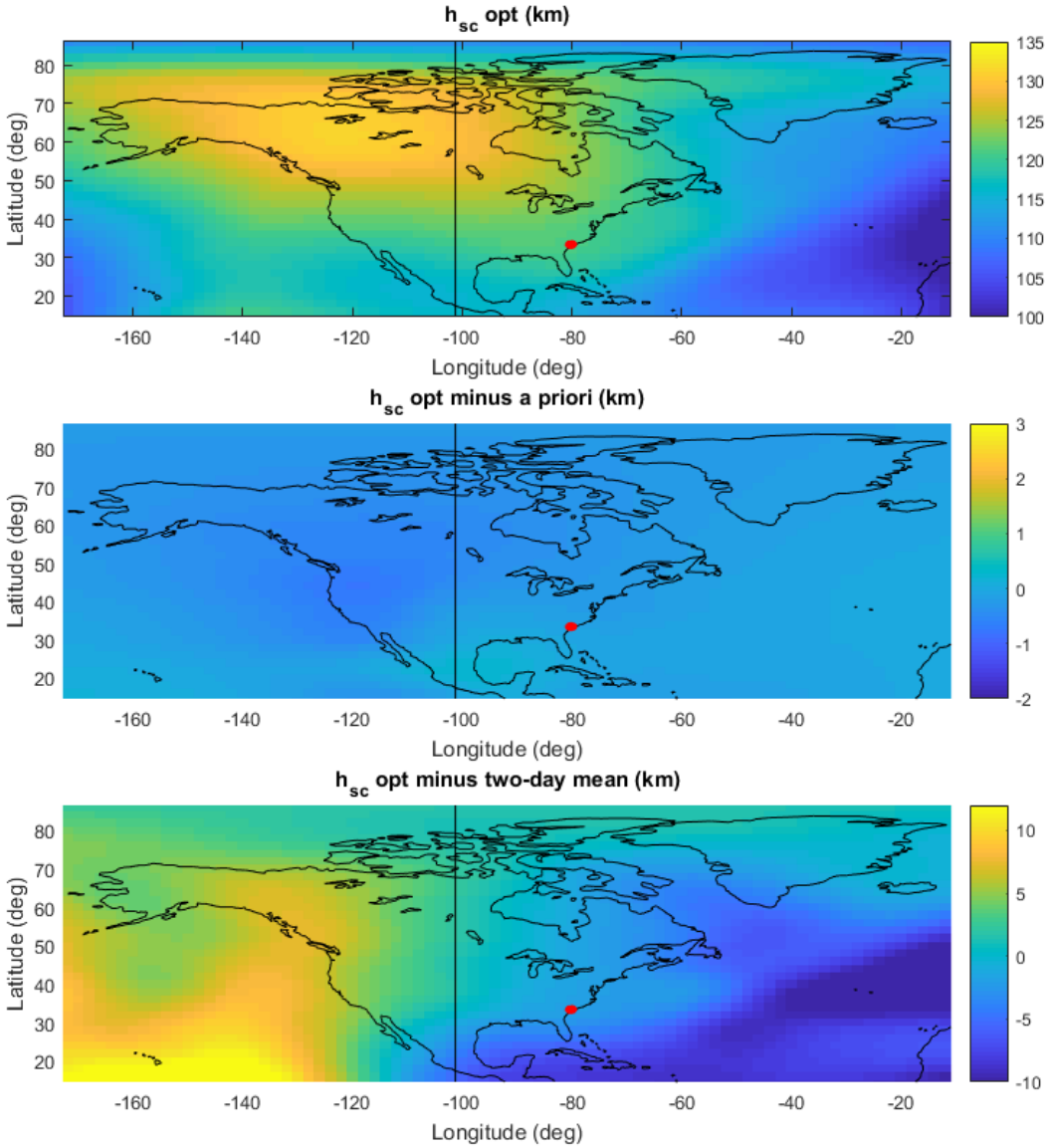

Figure 34: Optimal, deviation from *a priori,* and deviation from two-day mean maps of h_{sc} at 18:45 UTC. Local noon at 101° W.

Like h_{sc}, the eclipse leaves a large and distinct wake of disturbances in VTEC as it passes over the United States. The disturbances can be observed in comparing the optimal estimate to the *a priori* and two-day mean values – decreases in VTEC follow the eclipsed region in Figs. 35 - 38. Figure 35 shows that even when the eclipse was over Wyoming, parts of the Pacific Ocean and nearly the entire northwestern United States experienced a dip in VTEC of 6-8 TECU. This is a significant amount because the total VTEC in that region is no more than 10-12 TECU. The eclipse caused a lasting dip in VTEC of over one third of its initial value. As the eclipse approached local noon (see Fig. 36), the dip in VTEC associated with the subsolar peak being smaller than the *a priori* prediction began to merge with the dip in VTEC caused by the eclipse. For the most part, this seemed to mask any effects that the eclipse may have had on VTEC in these regions. Figure 38 shows a hint of the VTEC wake. As the sun approached, it appears that the west coast began to "recover" from the VTEC decrease.

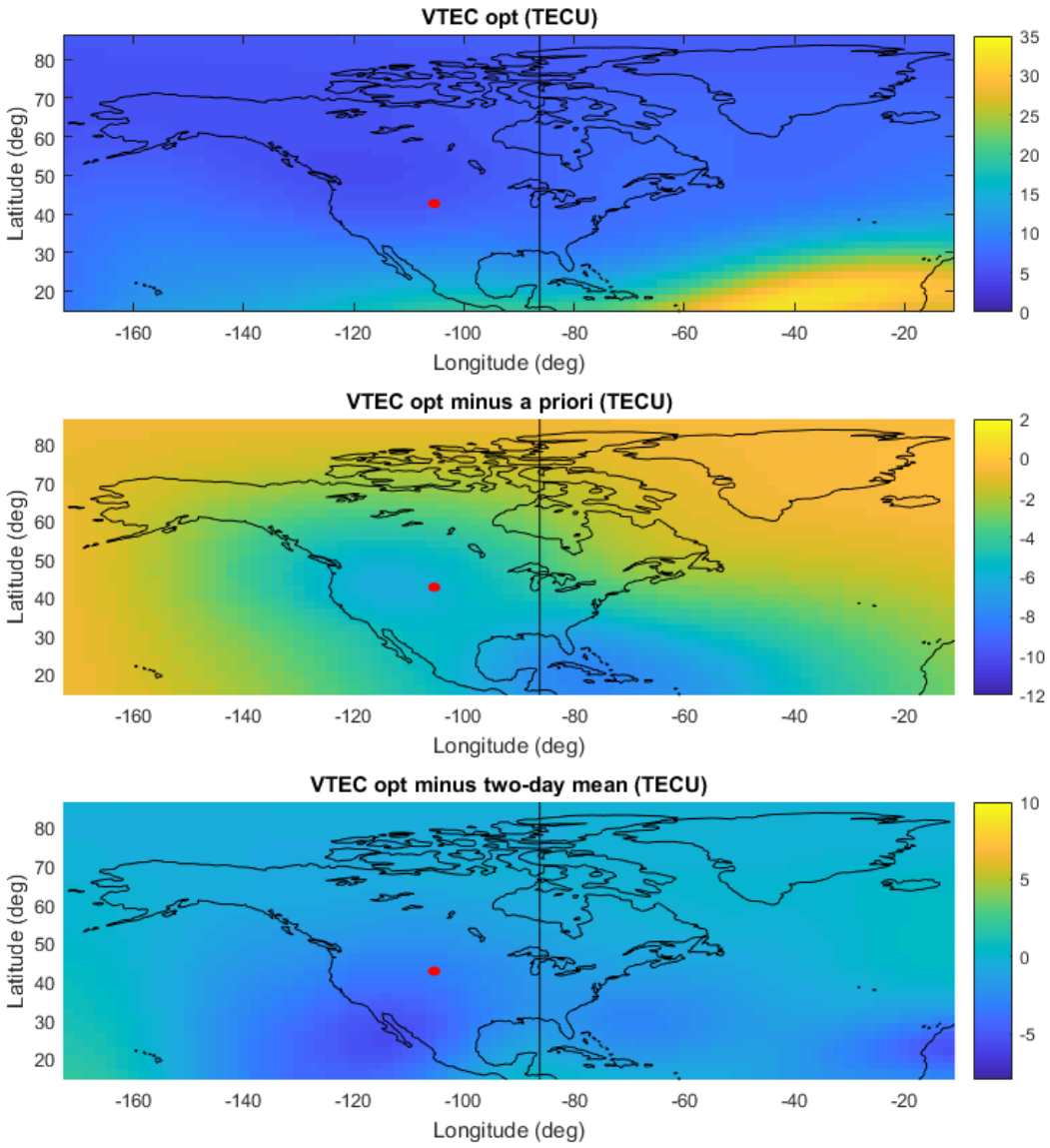

Figure 35: Optimal, deviation from *a priori,* and deviation from two-day mean maps of VTEC at 17:45 UTC. Local noon at 86° W.

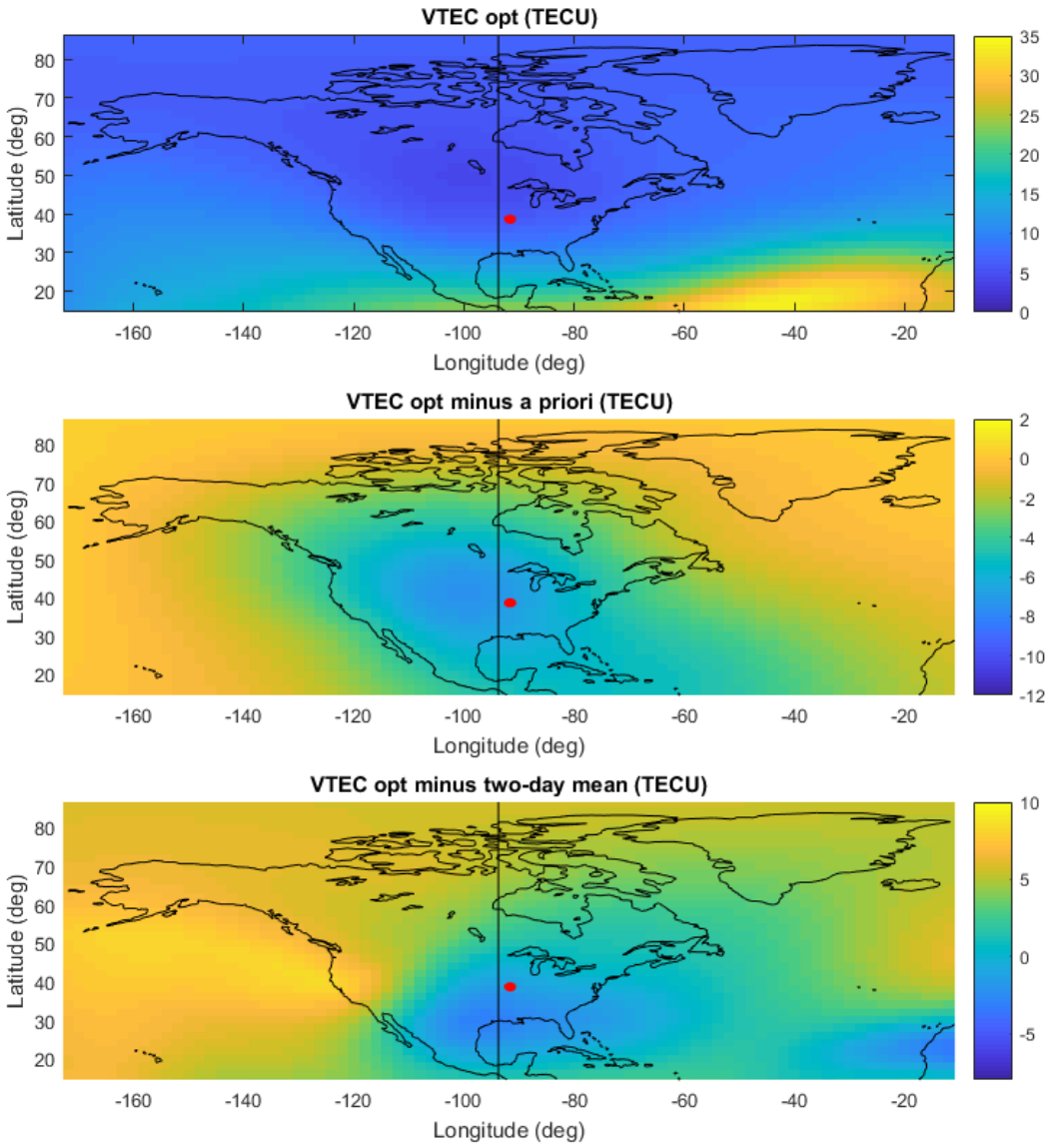

Figure 36: Optimal, deviation from *a priori,* and deviation from two-day mean maps of VTEC at 18:15 UTC. Local noon at 94° W.

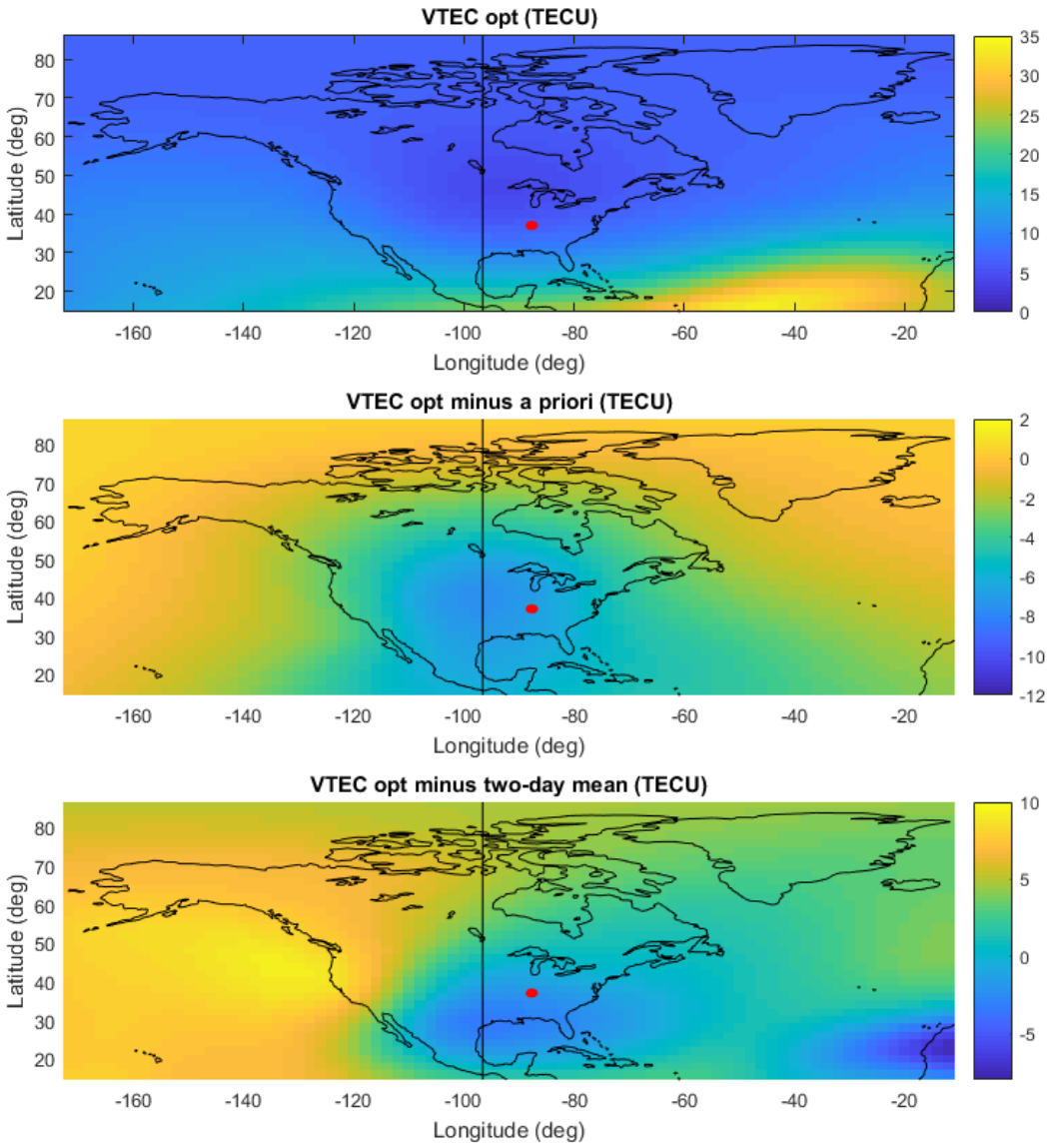

Figure 37: Optimal, deviation from *a priori,* and deviation from two-day mean maps of VTEC at 18:26 UTC. Local noon at 101° W.

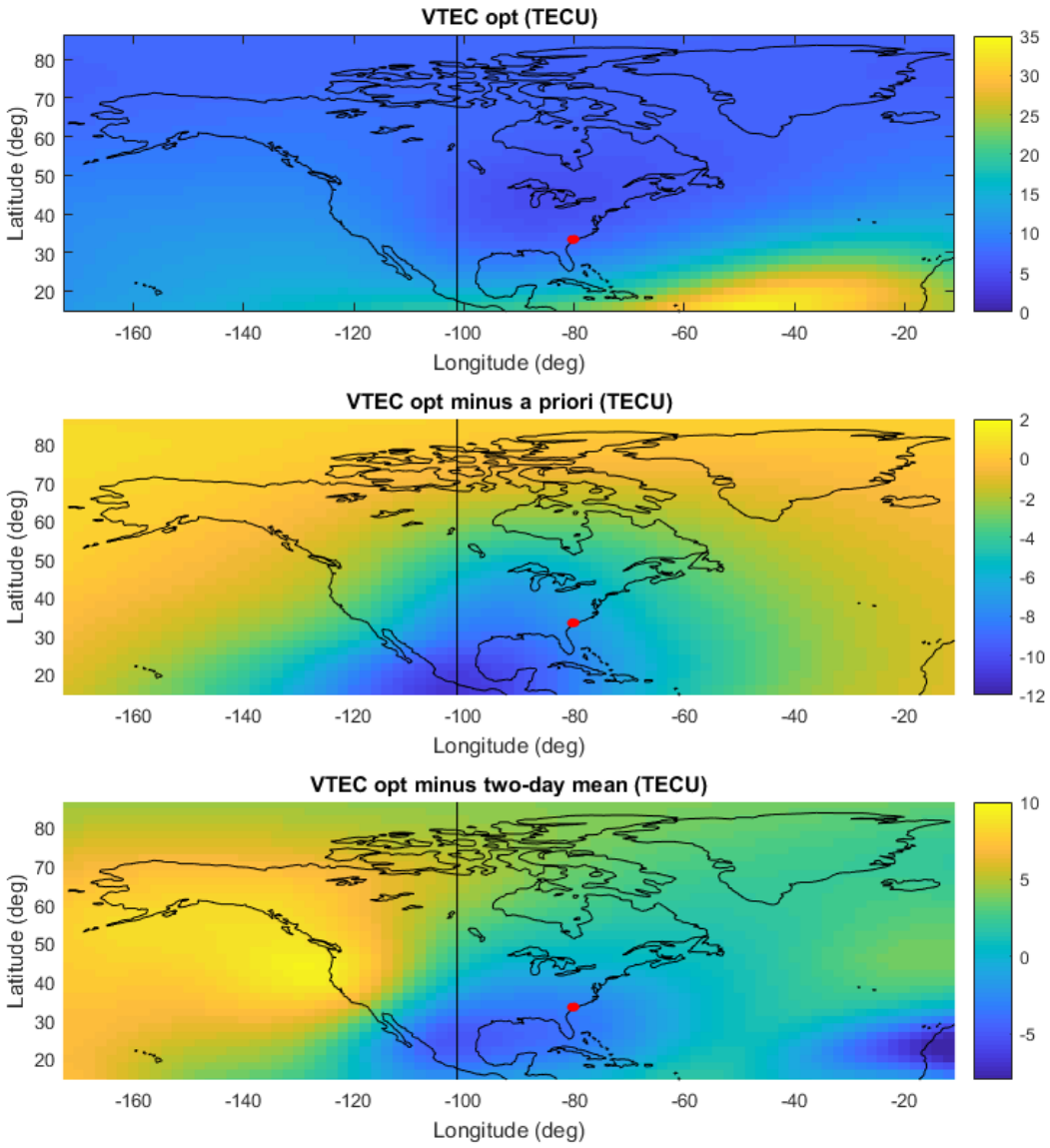

Figure 38: Optimal, deviation from *a priori,* and deviation from two-day mean maps of VTEC at 18:45 UTC. Local noon at 97° W.

4.5 Analysis of the Final Segment of the Eclipse

This section will analyze the final segment of the eclipse from 19:00 UTC until 21:04 UTC when the Earth is no longer partially eclipsed. Figures 40 - 44 plot maps of the estimated Chapman profile peak electron density altitude h_{nemax} at 4 successive times late in the eclipse. Figures 45 - 49 plot maps of the Chapman profile altitude scale height h_{sc} at the same set of times. Figures 50 - 54 plot maps of the Chapman profile Vertical TEC at the same set of times. The first of each of these sets of 5 plots corresponds to at 19:15 UTC when the eclipse traversed over the western part of the Atlantic Ocean. The slant TEC fit errors of the estimate at 19:15 UTC have mean/standard-deviation/peak values of -0.01/3.71/52.05 TECU. The second plot in each set of 5 corresponds to 19:45 UTC. The slant TEC fit errors of the estimate at 19:45 UTC have mean/standard-deviation/peak values of -0.01/3.67/49.60 TECU. The third plot in each set of 5 corresponds to 20:01 UTC when the Earth no longer is totally eclipsed. The slant TEC fit errors of the estimate at 20:01 UTC have mean/standard-deviation/peak values of -0.02/3.83/39.76 TECU. The fourth plot in each set of 5 corresponds to 20:30 UTC. The slant TEC fit errors of the estimate at 20:30 UTC have mean/standard-deviation/peak values of -0.01/3.67/49.60 TECU. Finally, the fifth plot in each set of 5 corresponds to 21:04 UTC when the Earth is no longer partially eclipsed. The slant TEC fit errors of the estimate at 21:04 UTC have mean/standard-deviation/peak values of 0.01/3.80/30.51 TECU.

The dataset used to produce the plots at 19:15 UTC contained 12042 slant TEC measurements from 1289 CORS receivers and 9 radio occultation passes. The dataset used to produce the plots at 19:45 UTC contained 11922 slant TEC measurements from 1313 CORS receivers and 8 radio occultation passes. The dataset used to produce the plots at 20:01 UTC contained 12297 slant TEC measurements from 1373 CORS receivers and 5 radio occultation passes. The dataset used to produce the plots at 20:30 UTC contained 12041 slant TEC measurements from 1321 CORS

receivers and 9 radio occultation passes. The dataset used to produce the plots at 21:04 UTC contained 12672 slant TEC measurements from 1289 CORS receivers and 5 radio occultation passes. Figure 39 shows the ionosphere pierce points of the lines-of-sight between CORS receivers and GPS satellites as dark grey dots. It also shows the lowest points of approach of the lines-of-sight between orbiting radio-occultation receivers and GPS satellites as white diamonds. This plot applies for the dataset corresponding to 19:15 UTC.

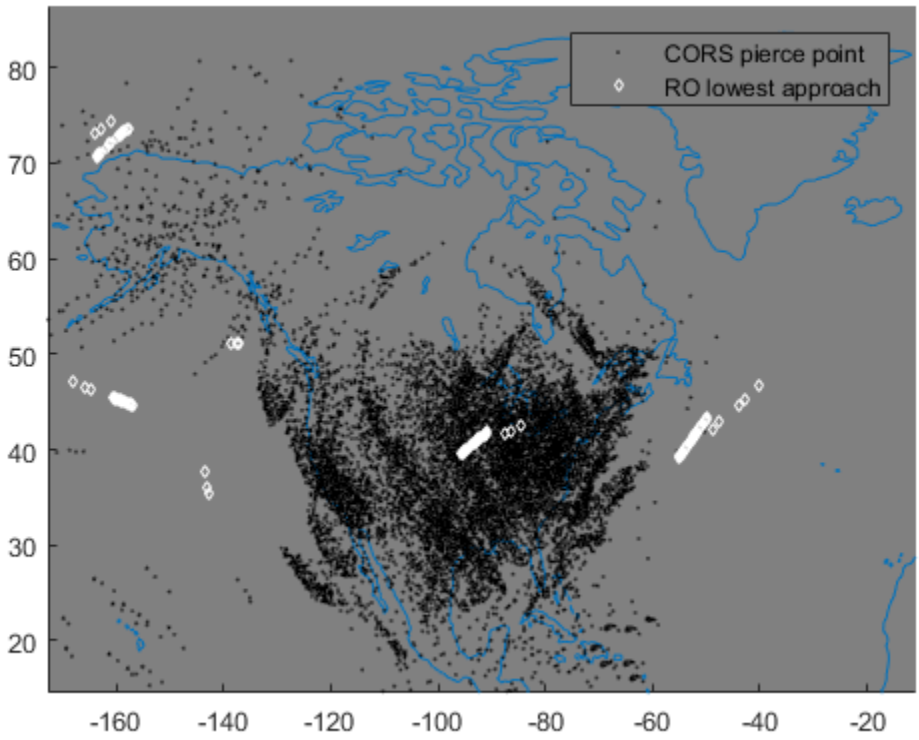

Figure 39: CORS to GPS satellite line-of-sight 350 km altitude ionosphere pierce points and points of lowest approach to the Earth of orbiting radio-occultation receiver to GPS satellite lines-of-sight. Data correspond to 19:15 UTC.

Figures 40 - 44 show some residual increases in h_{nemax} relative to the two-day average during the tail end of the eclipse. It is difficult, however, to discern a clear connection of the variable increases in these plots to the migration of the eclipse point or of the sub-solar point.

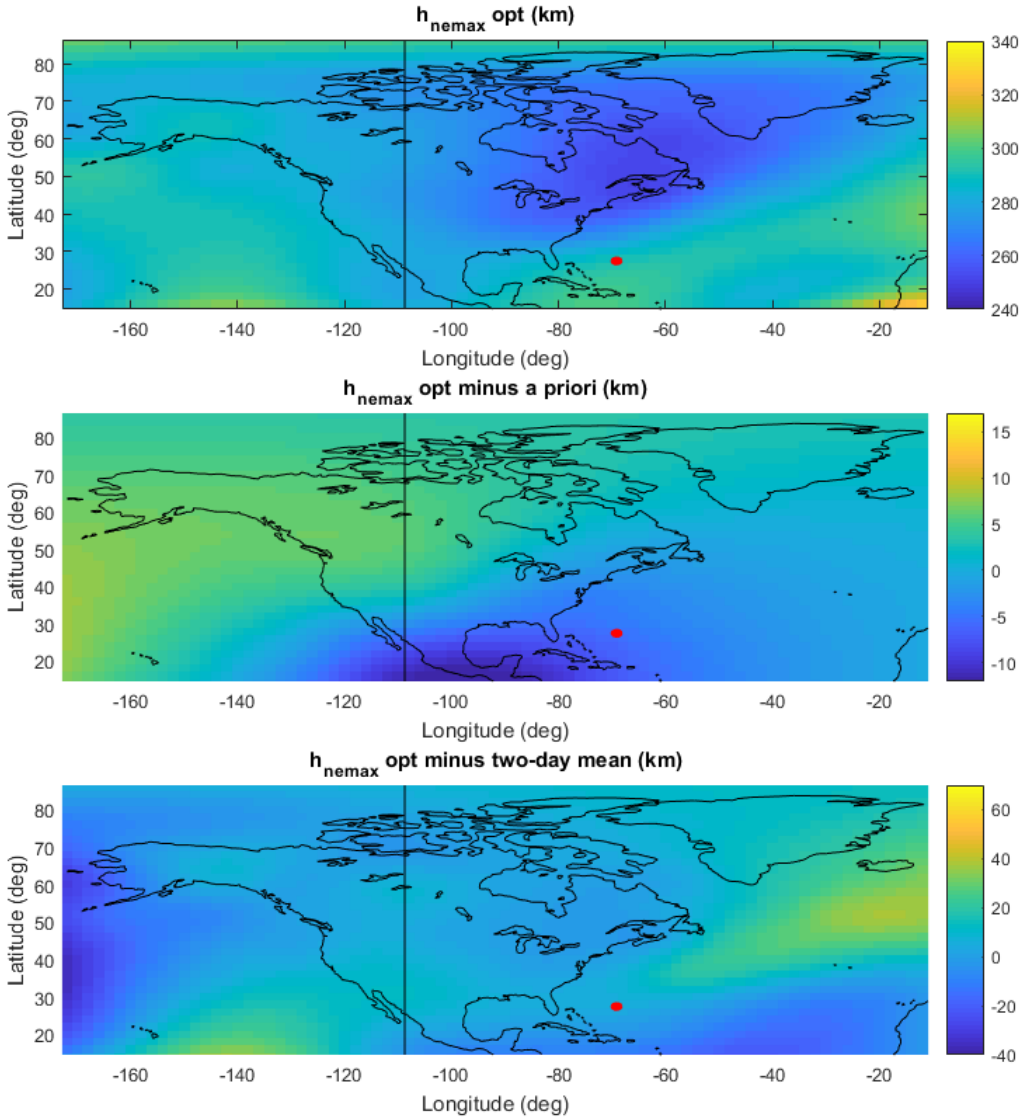

Figure 40: Optimal, deviation from *a priori,* and deviation from two-day mean maps of h_{nemax} at 19:15 UTC. Local noon at 109° W.

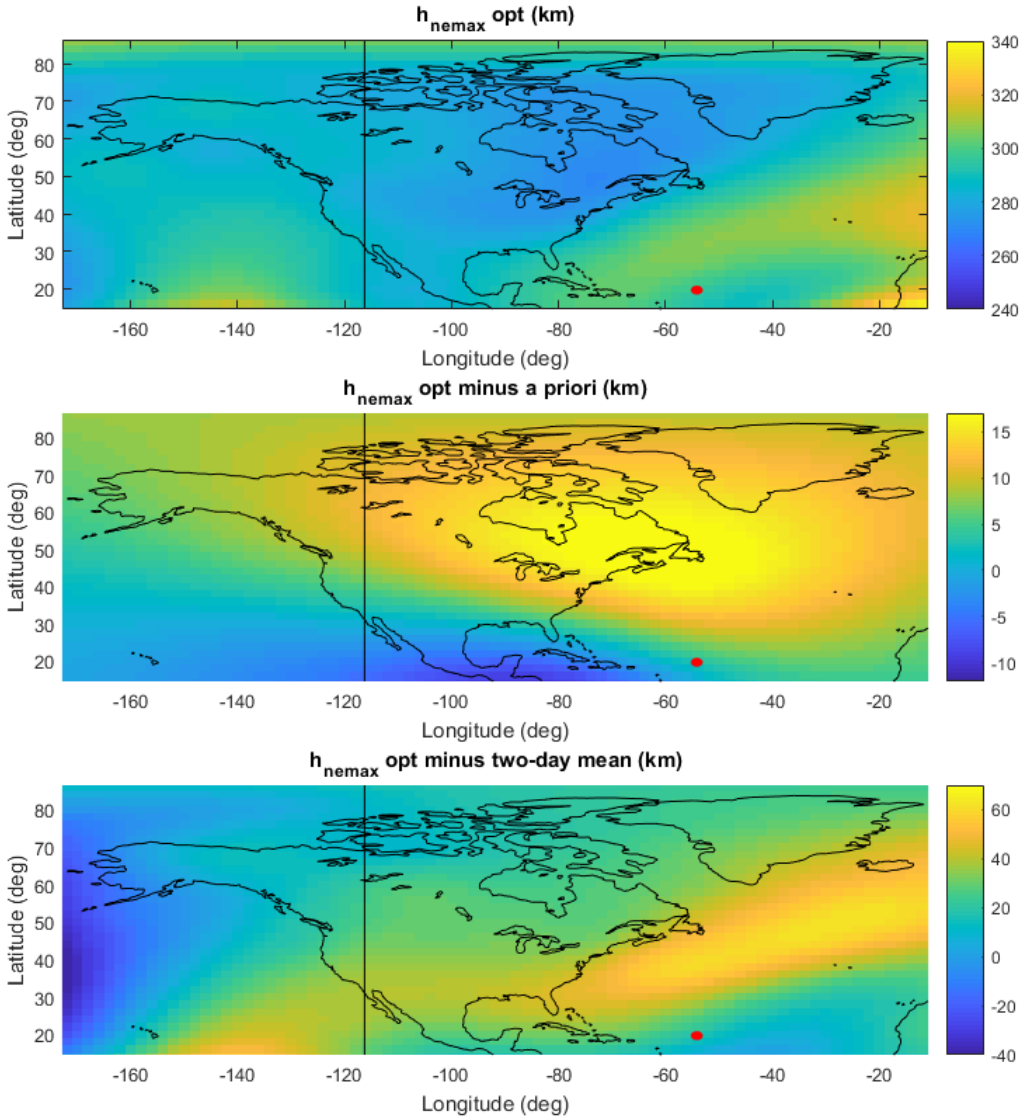

Figure 41: Optimal, deviation from *a priori,* and deviation from two-day mean maps of h_{nemax} at 19:45 UTC. Local noon at 116° W.

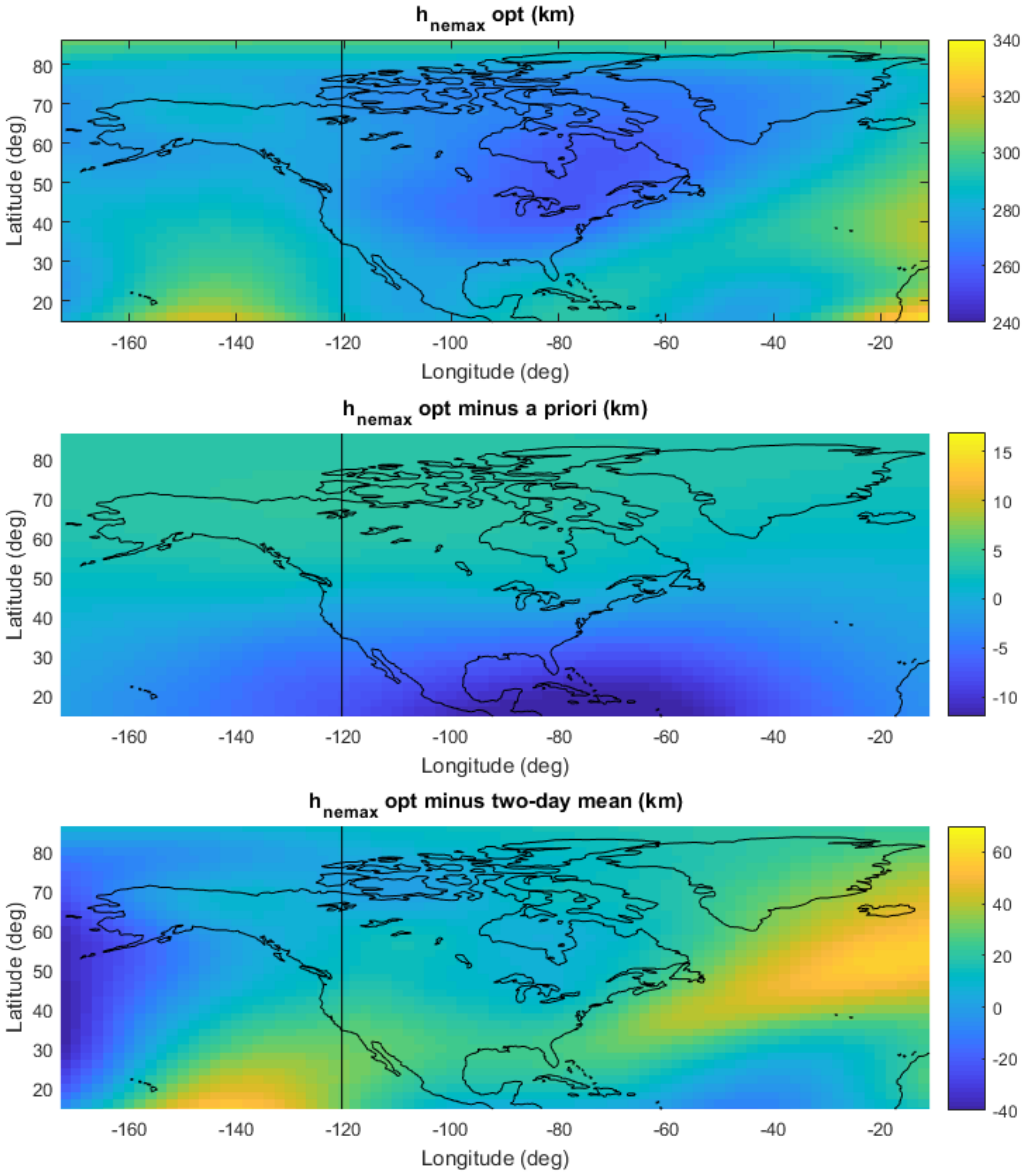

Figure 42: Optimal, deviation from *a priori,* and deviation from two-day mean maps of h_{nemax} at 20:01 UTC. Local noon at 120° W.

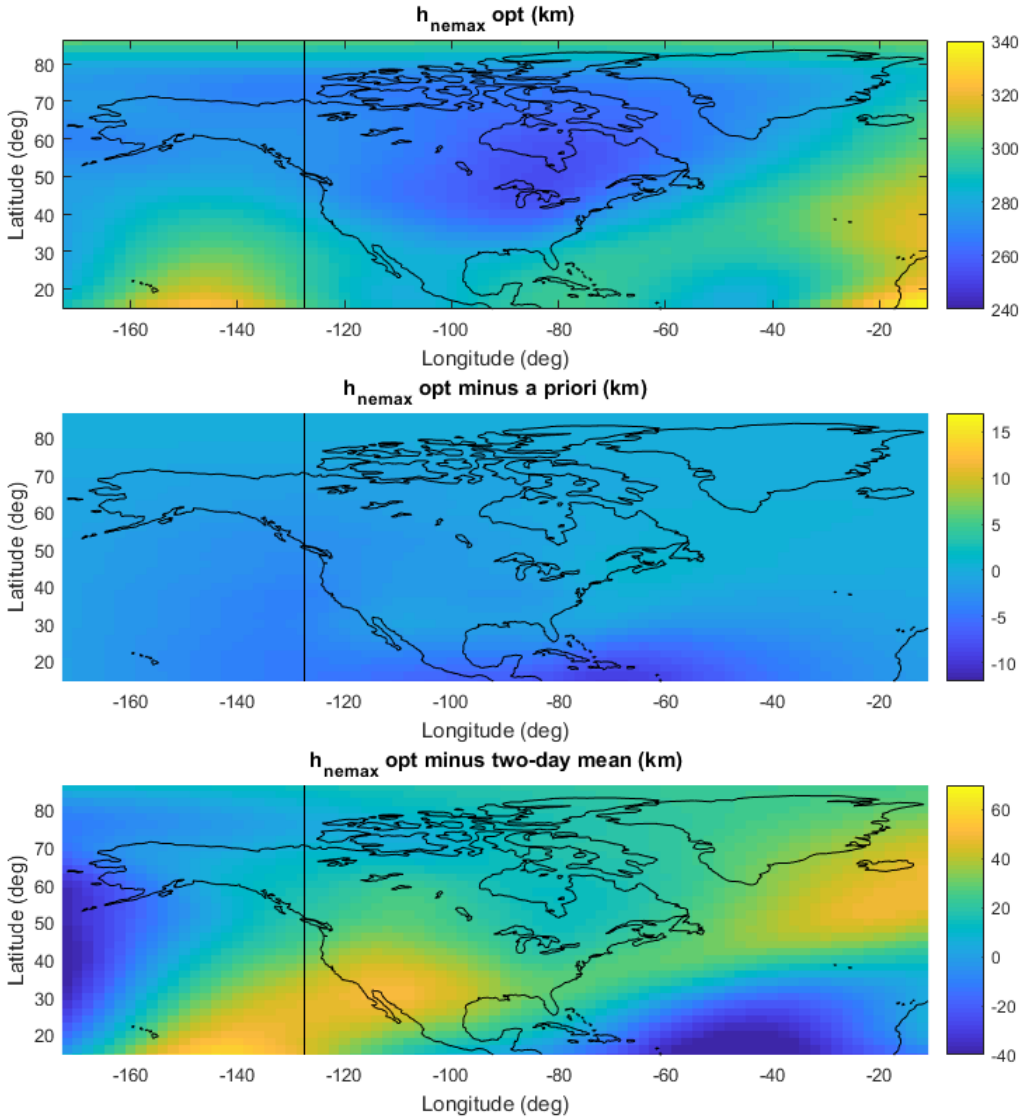

Figure 43: Optimal, deviation from *a priori,* and deviation from two-day mean maps of h_{nemax} at 20:30 UTC. Local noon at 128° W.

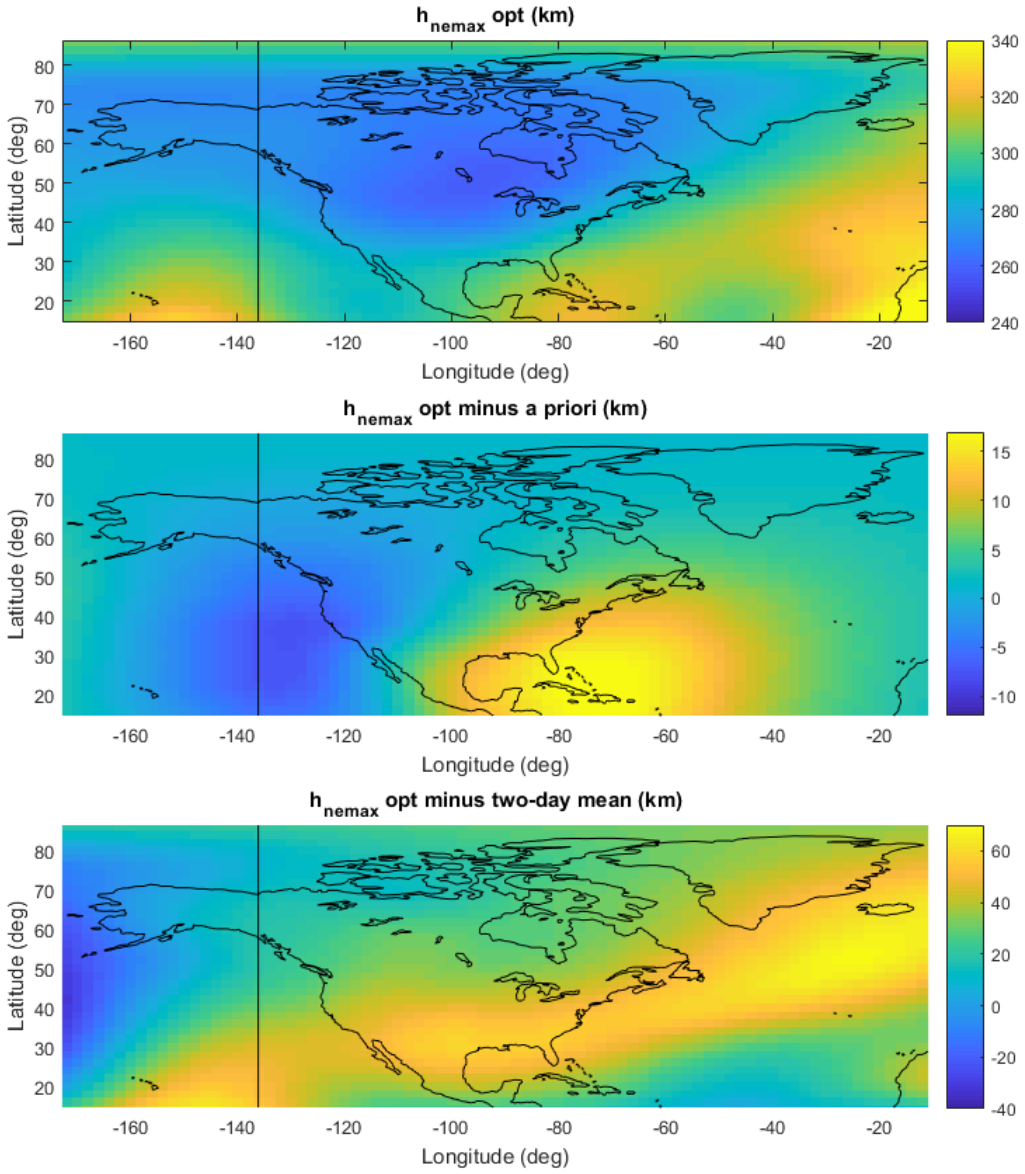

Figure 44: Optimal, deviation from *a priori,* and deviation from two-day mean maps of h_{nemax} at 21:04 UTC. Local noon at 136° W.

As the sun drifted west in the sky and the eclipse east, h_{sc} did not change from *a priori* values much but increased from two-day mean values on the west coast, as indicated by Figs. 45 - 49. Most of the United States seemed to have recovered and drifted towards expected *a priori* values. However, Fig. 46 showed a significant increase in h_{sc} over the north Atlantic. This increase is counter-intuitive because it is slightly out of range of the majority of the TEC measurements made and is the only case where h_{nemax} increased by that much.

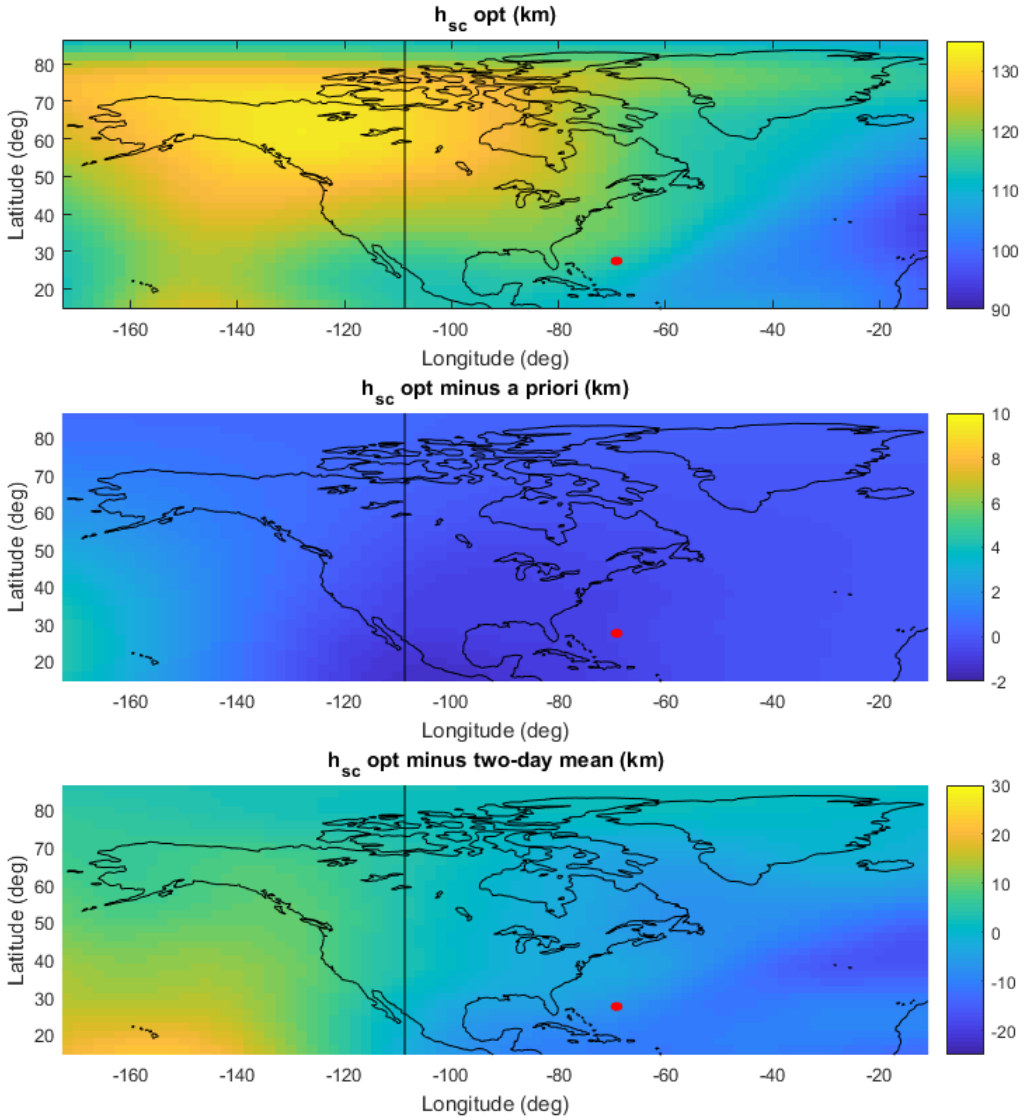

Figure 45: Optimal, deviation from *a priori,* and deviation from two-day mean maps of h_{sc} at 19:15 UTC. Local noon at 109° W.

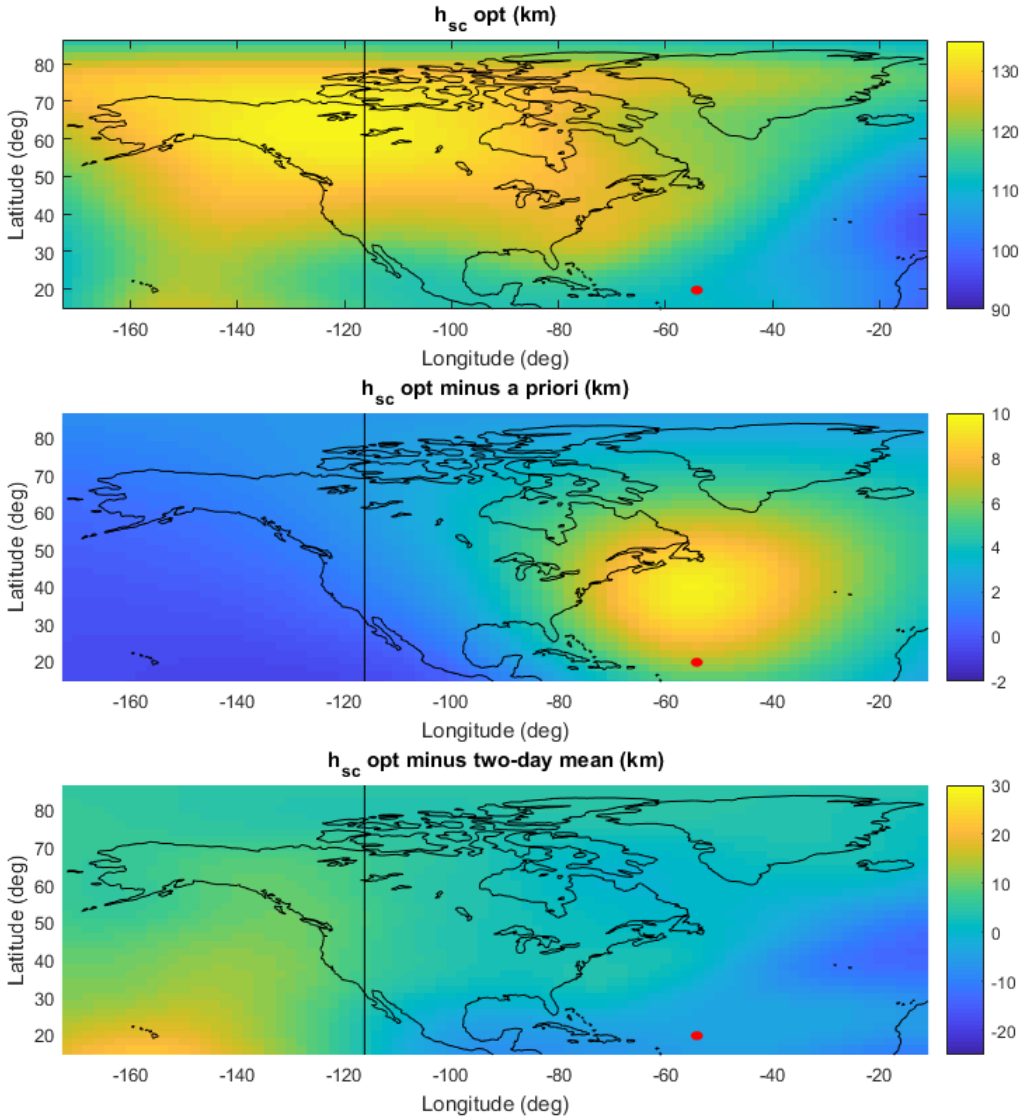

Figure 46: Optimal, deviation from *a priori,* and deviation from two-day mean maps of h_{sc} at 19:45 UTC. Local noon at 116° W.

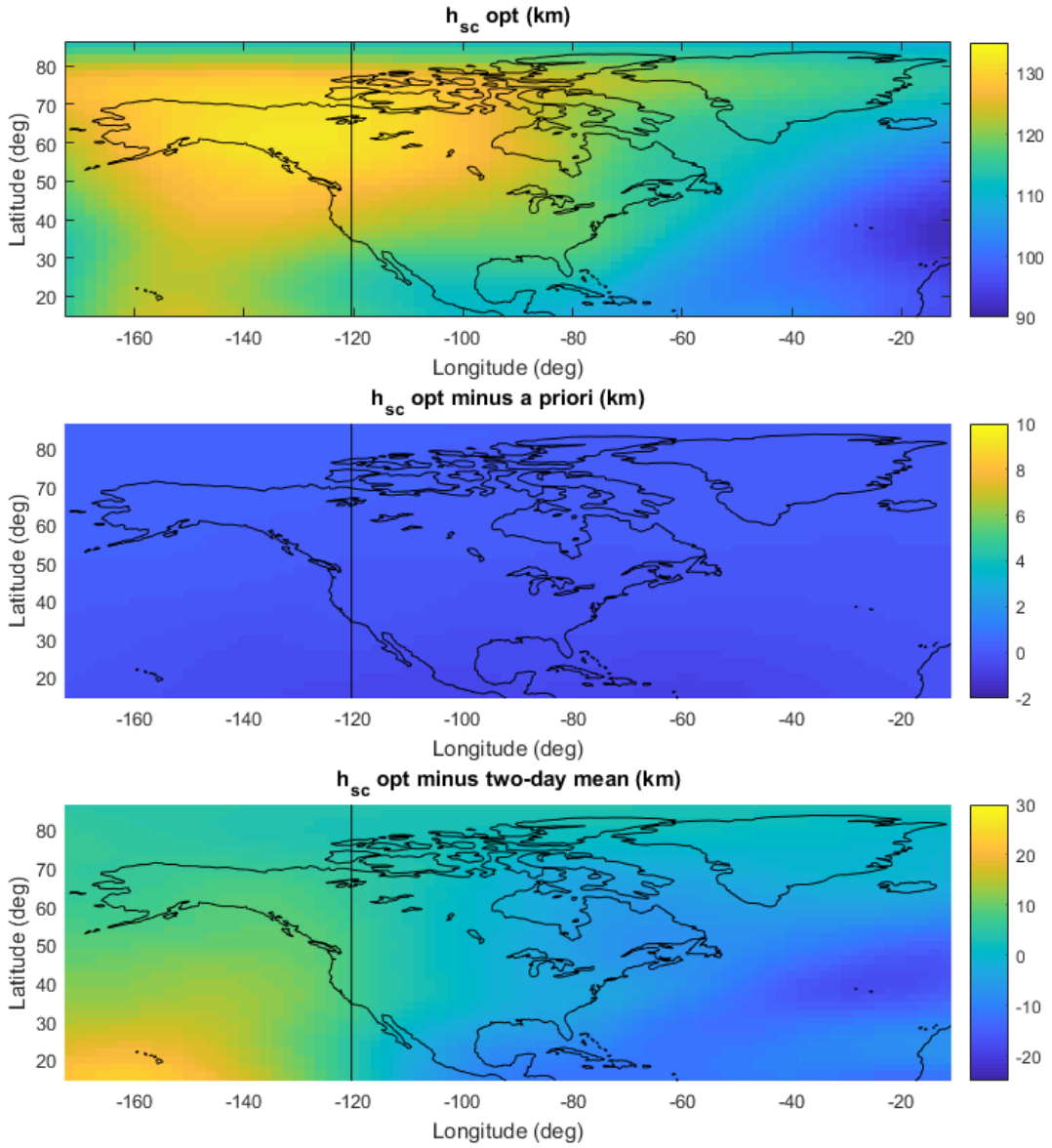

Figure 47: Optimal, deviation from *a priori,* and deviation from two-day mean maps of h_{sc} at 20:01 UTC. Local noon at 120° W.

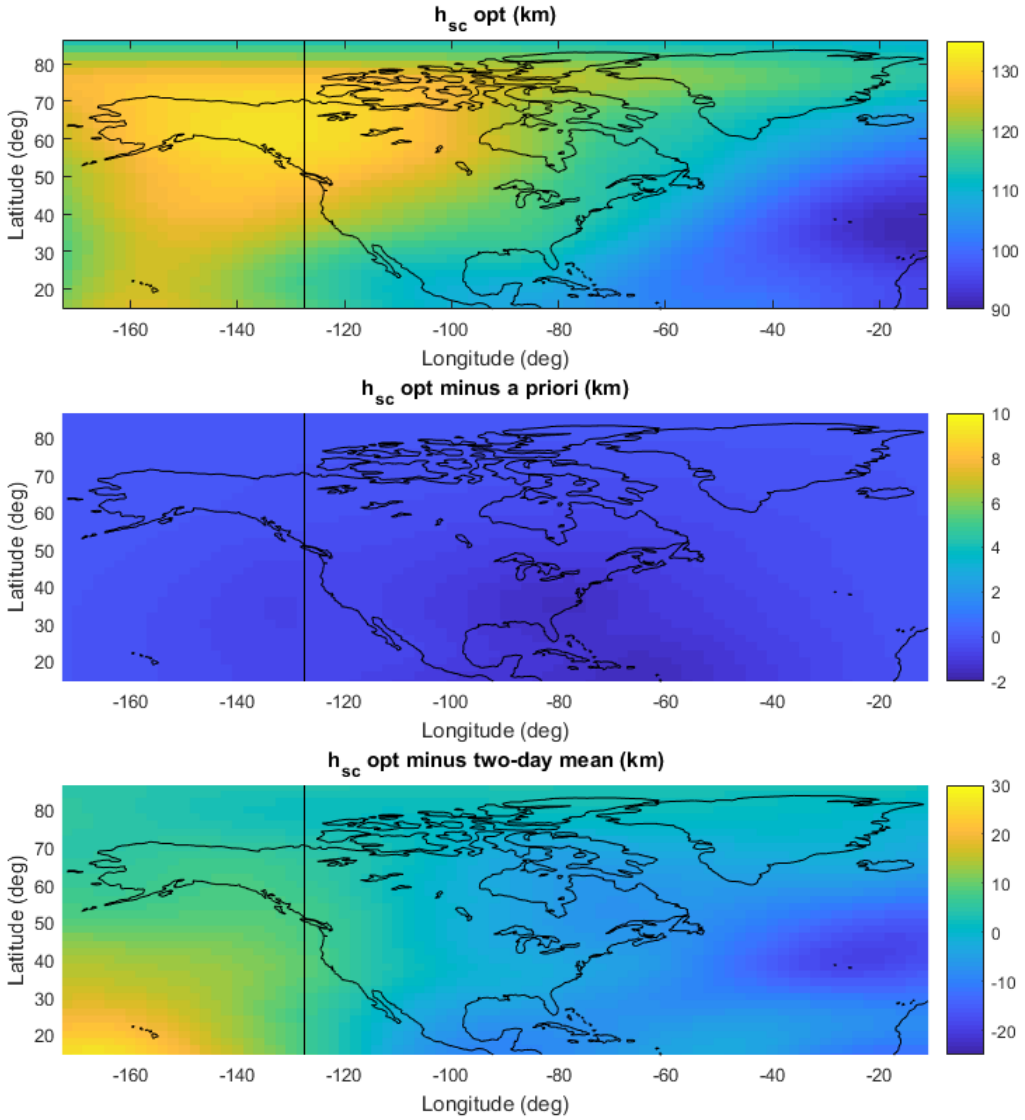

Figure 48: Optimal, deviation from *a priori,* and deviation from two-day mean maps of h_{sc} at 20:30 UTC. Local noon at 128° W.

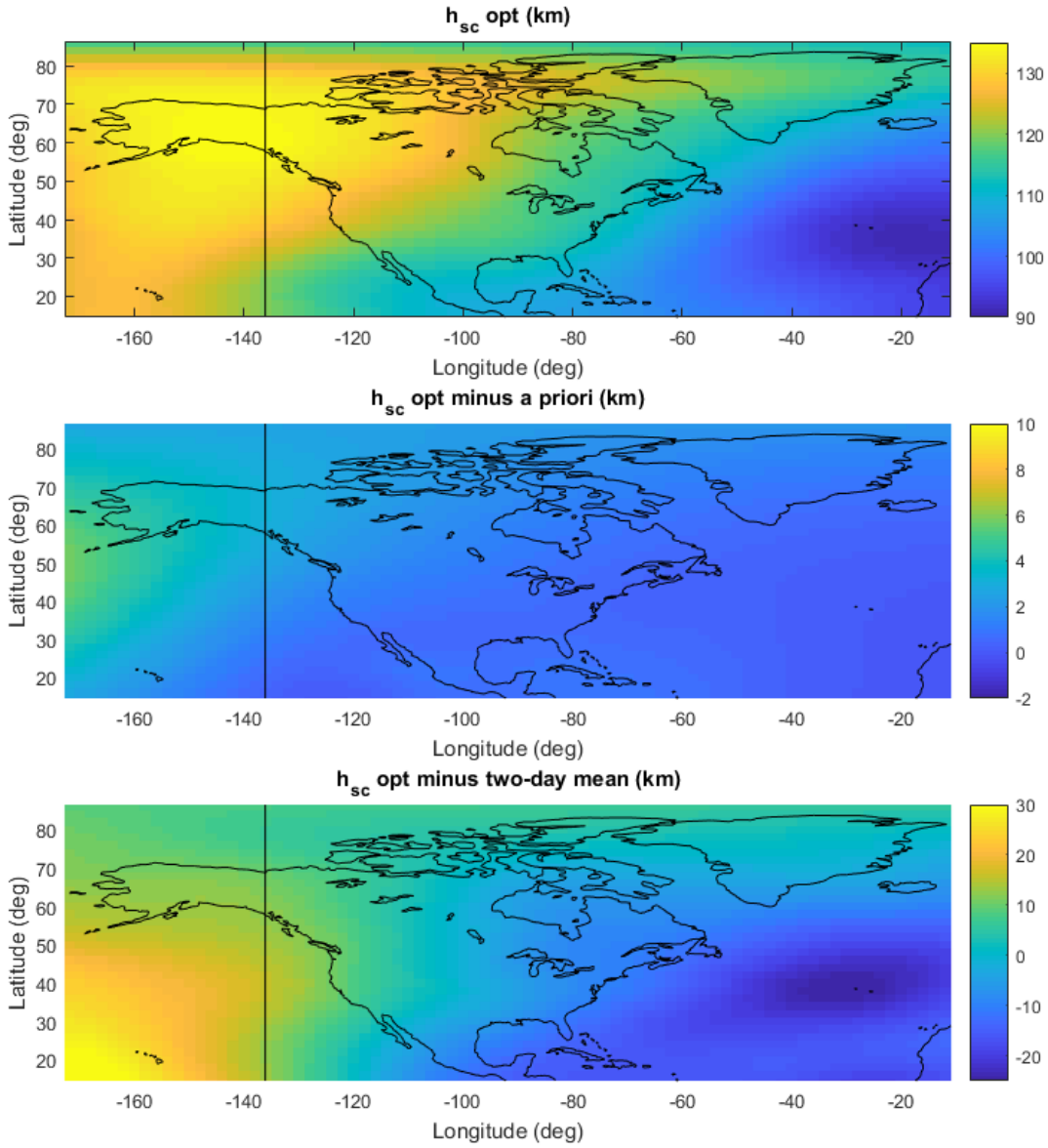

Figure 49: Optimal, deviation from *a priori,* and deviation from two-day mean maps of h_{sc} at 21:04 UTC. Local noon at 136° W.

The discrepancy in VTEC values caused from sun and eclipse passage from *a priori* information remained even after the eclipse passed overhead. Similar, but smaller, decrements in VTEC are seen in the wake of the eclipse region in the differences between the estimates and the two-day mean values. Figures 50 - 54 also show that even though the regions of the ionosphere that the eclipse passed over experienced VTEC differences from two-day mean values, VTEC values trended towards two-day mean values on the east coast of the United States as the sun set.

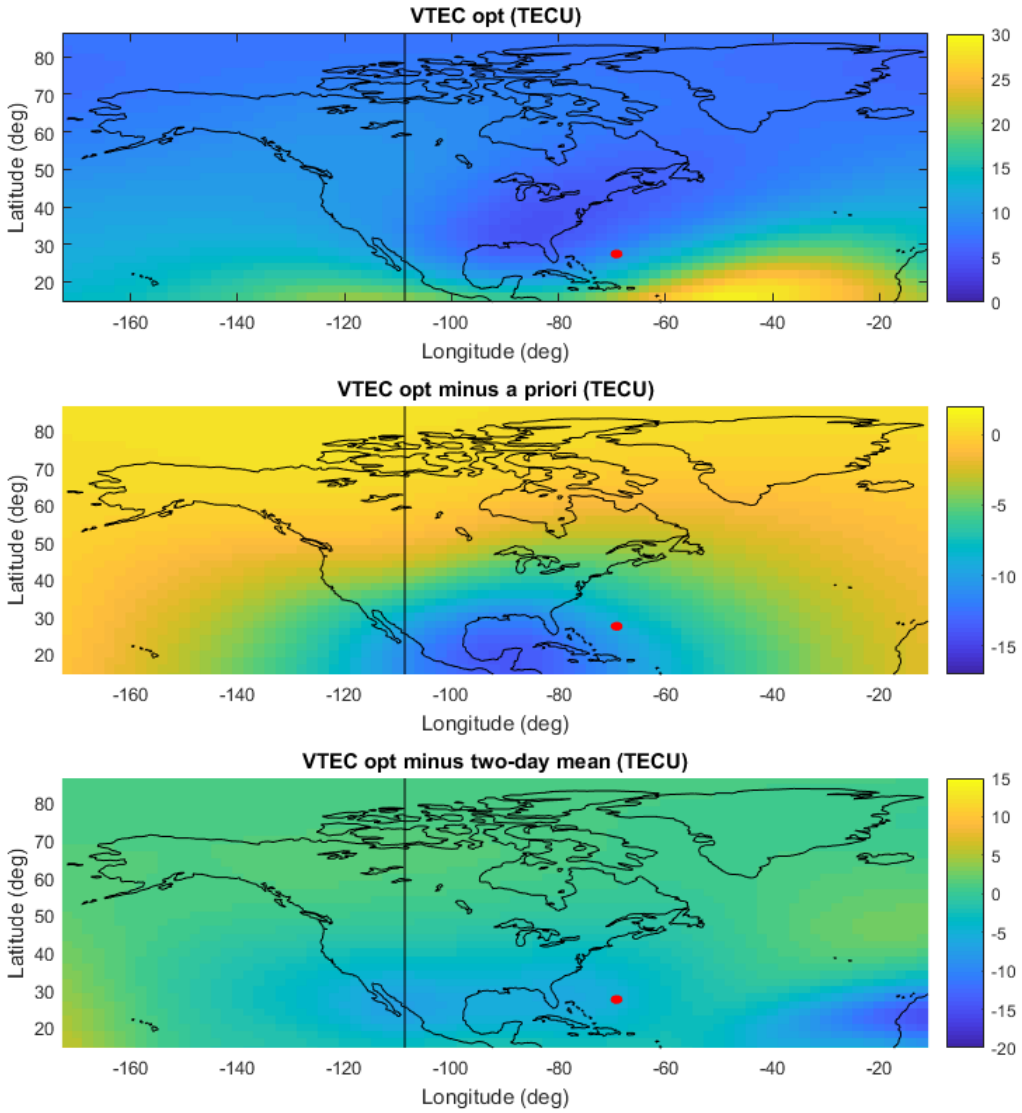

Figure 50: Optimal, deviation from *a priori,* and deviation from two-day mean maps of VTEC at 19:15 UTC. Local noon at 109° W.

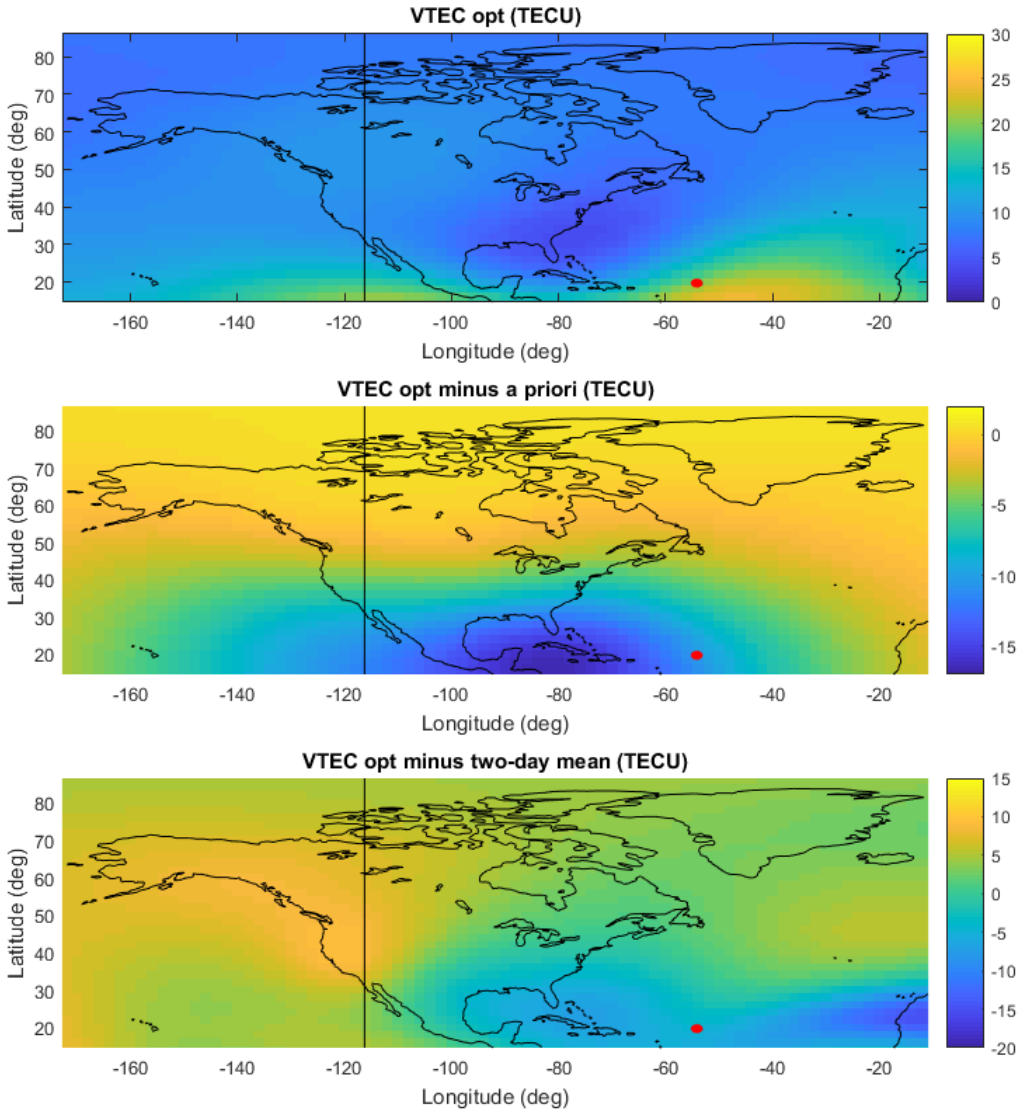

Figure 51: Optimal, deviation from *a priori,* and deviation from two-day mean maps of VTEC at 19:45 UTC. Local noon at 116° W.

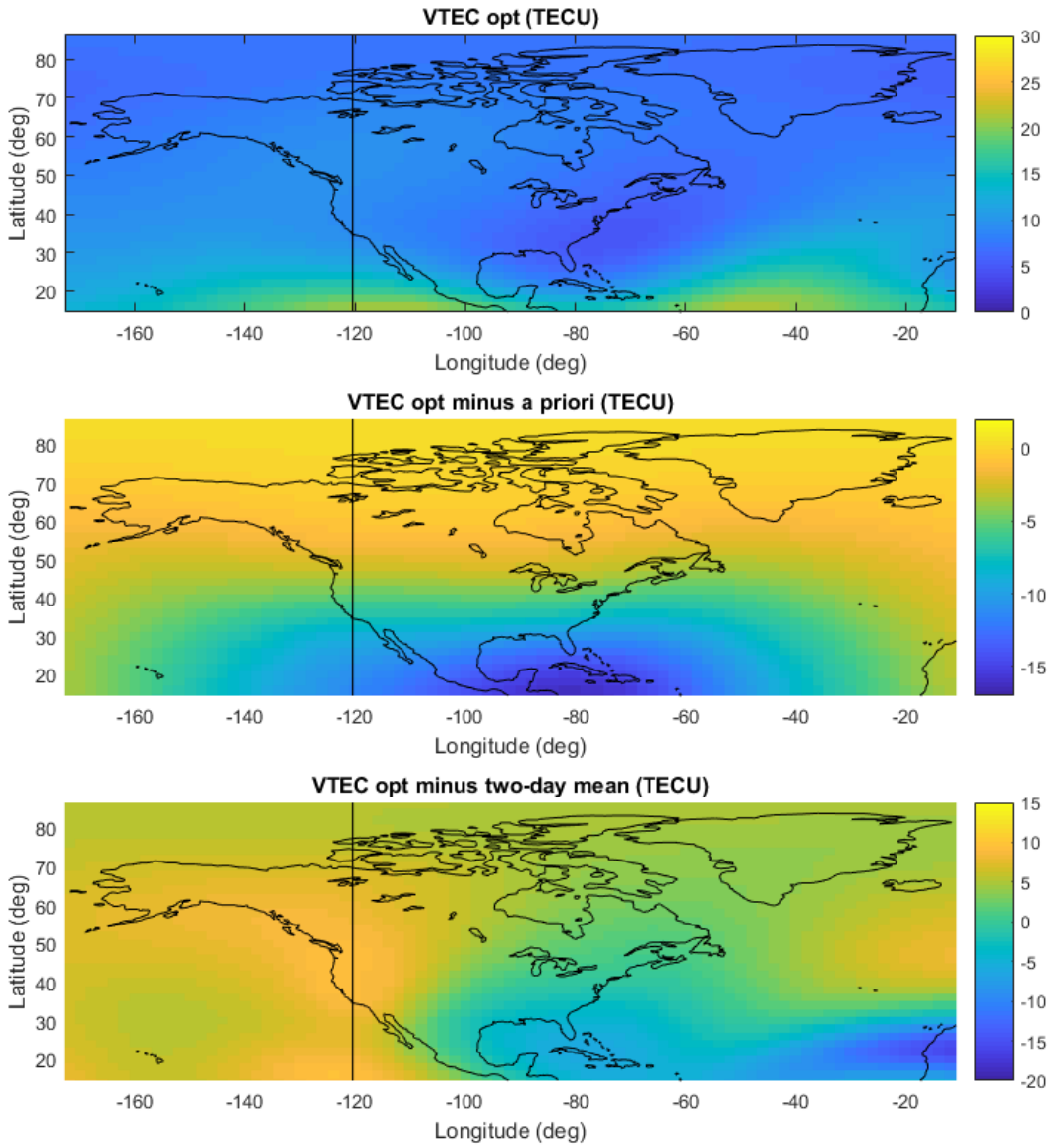

Figure 52: Optimal, deviation from *a priori,* and deviation from two-day mean maps of VTEC at 20:01 UTC. Local noon at 120° W.

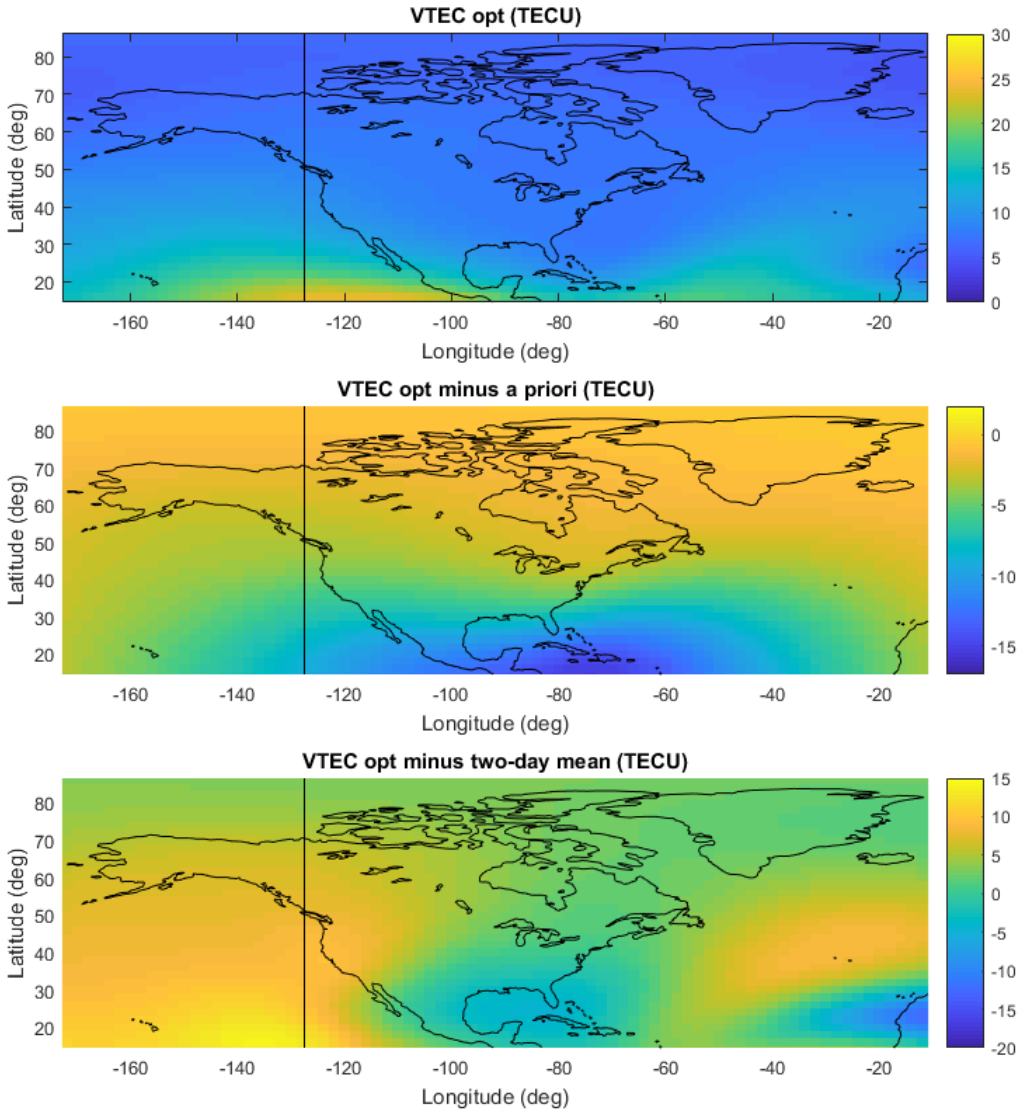

Figure 53: Optimal, deviation from *a priori,* and deviation from two-day mean maps of VTEC at 20:30 UTC. Local noon at 128° W.

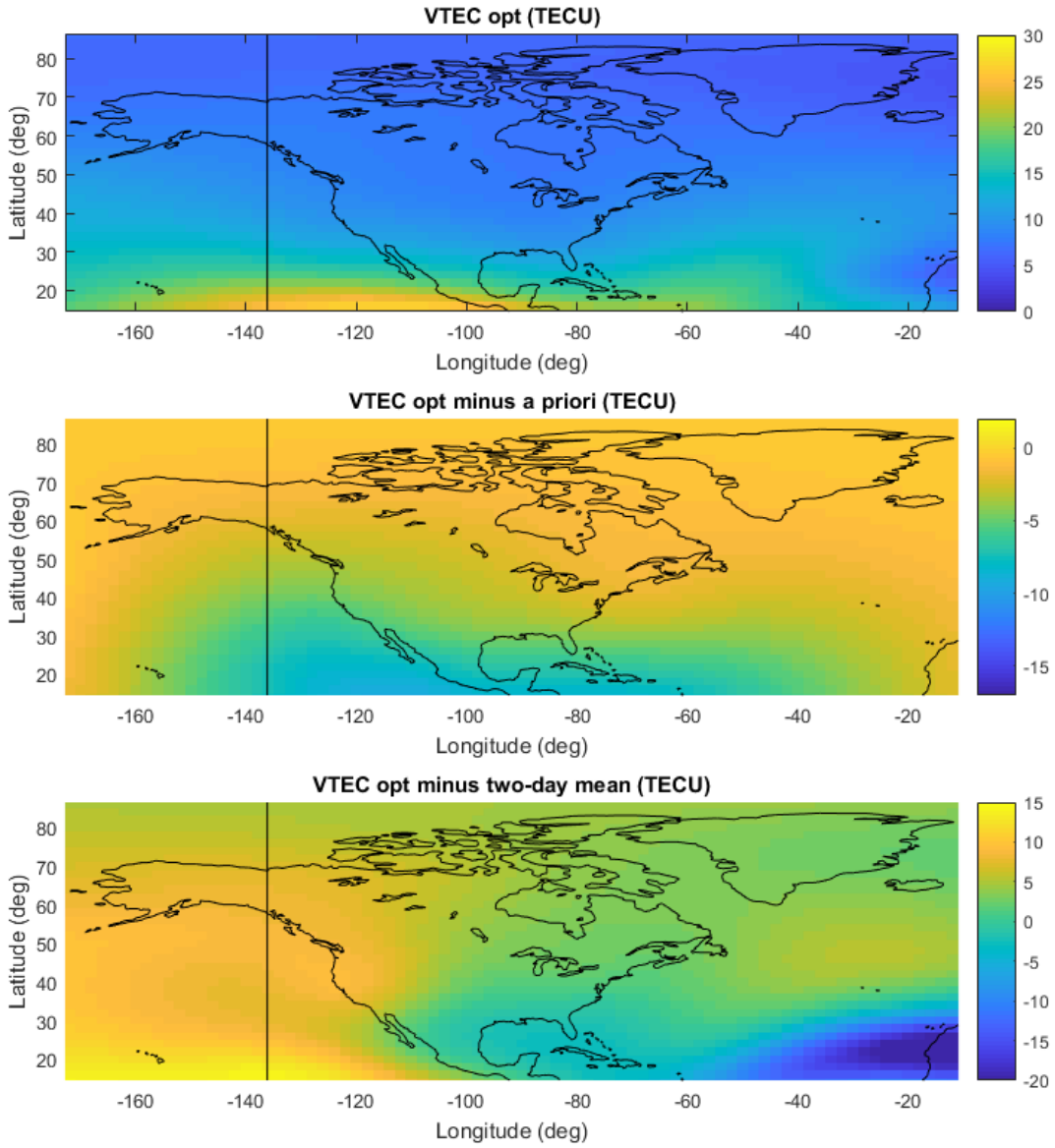

Figure 54: Optimal, deviation from *a priori,* and deviation from two-day mean maps of VTEC at 21:04 UTC. Local noon at 136° W.

CHAPTER 5: CONCLUSIONS

The algorithm designed in the thesis was the next installment of algorithms that fuse various data sources to estimate ionospheric electron density profiles [4]. Chapter 3 showcased the ability of the filter to produce a convincing estimate of the electron density profile. When inputting normal non-eclipse data, the filter performed well and had a relatively tight distribution. The thin-shell VTEC estimate comparison showed that the filter produced reasonable values. The reliability of the filter was examined when the biases between day and night cases was compared. Ideally, the biases of the receivers would change very little based on time of day, but the filter produced bias estimates that were too different between day and night cases to completely trust. Several possible solutions were tried and tested, but none were able to completely solve the problem. The bias differences were not quite reasonable. Future work should address this problem.

The eclipse dataset yielded several interesting results. The fits had large peak slant TEC fit error values that should not be of much concern. The peak fit error values are associated with measurements that pass-through regions of the ionosphere over the oceans where there were not many measurements. Those regions with few measurements tended towards *a priori* information, and in reality, the true ionosphere differed from the *a priori* ionosphere in those areas. The measurement/model mismatch is then due to the disruptions over the oceans that are not modeled well.

The altitude of peak electron density significantly increased as the eclipse passed through the United States. It left a wake of increased altitudes of peak electron density that was as high as 60 km immediately after eclipse passage and between 20 – 30 km hours afterwards. However, the lack of a pattern near the eclipse's path over CONUS in the final segments of the eclipse does not show a strong correlation between any lasting effects the eclipse had on the altitude of peak electron density.

The scale height map did not change very much. There was a small amount of movement that seemed to follow the eclipse. But, the scale of the movement was nearly negligible. It was certainly too small to correlate with the eclipse path.

The VTEC map during the beginning portion of the eclipse indicated that CONUS was already a few TECU above the two-day mean case. As the eclipse passed over the United States, a very distinct pocket of the ionosphere dropped in VTEC. This pocket moved with the eclipse path and showed a "wake" to the west of the eclipse that elongated slightly with time. However, once the eclipse passed, the dip in VTEC perturbation from the two-day mean value associated with the sun directly overhead, the pocket became less pronounced. Finally, near the latter parts of the eclipse, the gap between predicted VTEC and optimal VTEC over regions that had been passed over began to close and the ionosphere seemingly recovered to VTEC values that are a few TECU above the two-day mean case. However, a noticeable portion of the southeastern United States remained below this roughly 3 TECU difference from the two-day mean map.

Future work on estimating the ionosphere with this method should first incorporate any new radio occultation data. Plans for COSMIC-2 were recently scrapped. The new fleet would have had 12 satellites in orbit measuring TEC and would have drastically increased the amount of radio occultation data processed by this filter. Future work should also aim to incorporate new data sources like ionosonde measurements into the filter. Similarly, a few satellites have instruments other than GPS receivers that measure various features of the ionosphere, such as height of peak electron density, that can be assimilated. Finally, future iterations of the filter should enforce a requirement that the raw, bias-corrected TEC values in Section 3.3.1 are strictly positive.

REFERENCES

1. K. Rawer., *Wave Propagation in the Ionosphere*. Kluwer Acad.Publ., Dordrecht 1993.
2. P. Misra, P. Enge, *Global Positioning System: Signals, Measurements, and Performance*. 2nd Ed., Ganga-Jamuna Press, Massachusetts, 2011.
3. C. Cooper, A. Chartier, C. Mitchell, and D. Jackson, "Improving Ionospheric Imaging via the Incorporation of Direct Ionosonde Observations into GPS Tomography," in *Proceedings of the General Assembly and Scientific Symposium (URSI GASS), 2014 XXXIth URSI.* Beijing: IEEE, Aug. 2014.
4. M.L. Psiaki, G. Bust, C. Mitchell, "Nonlinear Estimation to Assimilate GPS TEC Data into a Regional Ionosphere Model," in *Proceedings of ION GNSS*, 2015.
5. N. Jakowski, et al., "Ionospheric behavior over Europe during the solar eclipse of 3 October 2005," in *Journal of Atmospheric and Solar-Terrestrial Physics* Vol. 70.6, 2008, pp. 836-853.
6. Cheng, Kang, Yinn-Nien Huang, Sen-Wen Chen, "Ionospheric effects of the solar eclipse of September 23, 1987, around the equatorial anomaly crest region," *Journal of Geophysical Research: Space Physics* Vol. 97.A1, 1992, pp. 103-111.
7. E. L. Afraimovich, "Ionospheric effects of the solar eclipse of March 9, 1997, as deduced from GPS data," *Geophysical research letters,* Vol. 25.4, 1998, pp. 465-468.
8. H. Le, "The ionospheric responses to the 11 August 1999 solar eclipse: observations and modeling," *Annales geophysicae: atmospheres, hydrospheres and space sciences,* Vol. 26, 2008.
9. E.L. Afraimovich, E. A. Kosogorov, and O. S. Lesyuta, "Effects of the August 11, 1999 total solar eclipse as deduced from total electron content measurements at the GPS

network," *Journal of atmospheric and solar-terrestrial physics,* Vol. 64.18, 2002, pp. 1933-1941.

10. L.G. Smith, et al., "Measurements in the ionosphere during the solar eclipse of 20 July 1963," *Journal of Atmospheric and Terrestrial Physics,* Vol. 27.7, 1965, pp. 803-829.
11. N. A. Frissell, et al., "Modeling Amateur Radio Soundings of the Ionospheric Response to the 2017 Great American Eclipse," *Geophysical Research Letters*, Vol. 45.10, 2018, pp. 4665-4674.
12. Earle, Gregory Duane, et al., "HF Band Observations and Modeling of the 2017 Eclipse," *AGU Fall Meeting Abstracts*, 2017.
13. The Free Dictionary, *Ionosphere,* in *https://encyclopedia2.thefreedictionary.com/ionosphere*. The Free Dictionary: thefreedictionary.com
14. Bilitza, Dieter, and Bodo W. Reinisch, "International reference ionosphere 2007: improvements and new parameters," in *Advances in space research,* Vol. 42.4, 2008, pp. 599-609.
15. J. Feltens, "Chapman profile approach for 3-D global TEC representation," in *IGS Presentation*, 1998.
16. CDAAC, *https://cdaac-www.cosmic.ucar.edu/* . CDAAC: Cosmic Data Analysis and Archive Center.
17. P. Gill, W. Murray, and M. Wright, *Practical Optimization*, New York: Academic Press, 1981.
18. M.L. Psiaki, K.C. Ward, and K.J. DeMars, “A Bi-Quintic Latitude/Longitude Spline and Lunar Surface Modeling for Spacecraft Navigation,” Proc. Junkins Dynamical Systems Symposium, May 20-21, 2018, College Station, TX.